



Delft University of Technology

Optomechanical devices in the quantum regime

Marinkovic, Igor

DOI

[10.4233/uuid:aa1e9f1e-456b-4ac9-b541-991d7f6baaa6](https://doi.org/10.4233/uuid:aa1e9f1e-456b-4ac9-b541-991d7f6baaa6)

Publication date

2019

Citation (APA)

Marinkovic, I. (2019). *Optomechanical devices in the quantum regime*. [Dissertation (TU Delft), Delft University of Technology]. <https://doi.org/10.4233/uuid:aa1e9f1e-456b-4ac9-b541-991d7f6baaa6>

Important note

To cite this publication, please use the final published version (if applicable). Please check the document version above.

Copyright

Other than for strictly personal use, it is not permitted to download, forward or distribute the text or part of it, without the consent of the author(s) and/or copyright holder(s), unless the work is under an open content license such as Creative Commons.

Takedown policy

Please contact us and provide details if you believe this document breaches copyrights. We will remove access to the work immediately and investigate your claim.

This work is downloaded from Delft University of Technology.

For technical reasons the number of authors shown on this cover page is limited to a maximum of 10.

OPTOMECHANICAL DEVICES IN THE QUANTUM REGIME

OPTOMECHANICAL DEVICES IN THE QUANTUM REGIME

Proefschrift

ter verkrijging van de graad van doctor
aan de Technische Universiteit Delft,
op gezag van de Rector Magnificus Prof. dr. ir. T.H.J.J. van der Hagen,
voorzitter van het College voor Promoties,
in het openbaar te verdedigen op vrijdag 14 juni 2019 om 10:00 uur

door

Igor MARINKOVIĆ

Master of Science in Physics,
University of Bonn, Bonn, Germany,
geboren te Kragujevac, Serbia.

Dit proefschrift is goedgekeurd door de

promotor: Dr. S. Gröblacher

promotor: Prof.dr.ir H.S.J. van der Zant

Samenstelling promotiecommissie:

Rector Magnificus,	voorzitter
Dr. S. Gröblacher,	Technische Universiteit Delft
Prof.dr.ir H.S.J. van der Zant,	Technische Universiteit Delft
Prof.dr. Y. Blanter	Technische Universiteit Delft
Prof.dr. P.G. Steeneken	Technische Universiteit Delft
Prof.dr. E. Verhagen	AMOLF
Prof.dr. A. Fiore	Technische Universiteit Eindhoven
Prof.dr. N. Sangouard	Universität Basel



This work is part of the research programme of the Foundation for Fundamental Research on Matter (FOM), which is financially supported by the Netherlands Organisation for Scientific Research (NWO).

Keywords: cavity optomechanics, optomechanical crystals, intensity interferometry, Bell inequality

Printed by: IPSKAMP PRINTING

Front & Back: Optical microscope image of nanobeam devices.

Copyright © 2019 by I. Marinković
Casimir PhD Series, Delft-Leiden 2019-15

ISBN 978-90-8593-401-1

An electronic version of this dissertation is available at
<http://repository.tudelft.nl/>.

CONTENTS

1	A place for mechanical resonators in the quantum world	1
1.1	Why mechanical resonators?	2
1.2	Why optomechanics?	2
1.3	Why this thesis?	3
	References	4
2	Basics of optomechanics	7
2.1	Intro to optomechanics	8
2.1.1	Optomechanical Hamiltonian	8
2.1.2	Linearized Hamiltonian	9
2.1.3	Action of optomechanical Hamiltonian	9
2.2	Open dynamics	11
2.3	Quantum experiments of harmonic oscillator.	13
2.3.1	Sideband asymmetry	13
2.3.2	Hanbury Brown and Twiss interferometry	14
2.3.3	Cauchy Schwarz inequality	15
2.3.4	Bell inequality	16
	References	18
3	Optomechanical crystal nanobeam	21
3.1	Photonic crystal cavity	22
3.2	Fiber to nanobeam coupling	22
3.2.1	Fiber to waveguide coupling	22
3.2.2	Waveguide to nanobeam coupling	25
3.3	More than optomechanics	26
3.4	Why silicon nanobeams.	27
	References	28
4	Fabrication of optomechanical nanobeam devices	31
4.1	Fabrication of silicon nanobeam devices	32
4.1.1	Electron beam lithography.	32
4.1.2	Dry etching	33
4.1.3	Wet processing.	36
4.2	Fabricating identical devices	37
4.3	Fabricating tapered fibers.	37
	References	38

5	Hanbury Brown and Twiss interferometry of single phonons from an optomechanical resonator	41
5.1	Main Text	42
5.2	Materials and Methods	47
	References	56
6	Optomechanical Bell test	61
6.1	Main Text	62
6.2	Supplementary Information	69
	References	73
7	Conclusion	79
	References	80
8	Appendix	81
8.1	Fabrication failures and hints	81
8.2	Measuring input coupling of photonic resonator	81
8.3	Efficient fiber coupling inside a dilution fridge	84
	References	86
	Summary	87
	Samenvatting	89
	Acknowledgements	91
	Curriculum Vitæ	93
	List of Publications	95
	References	95

1

A PLACE FOR MECHANICAL RESONATORS IN THE QUANTUM WORLD

Igor Marinković

I will discuss why some of the properties of mechanical resonators can be attractive for quantum information applications. Also I will show how experimental efforts described in this thesis fit into the story.

1.1. WHY MECHANICAL RESONATORS?

Investigating optical fields at level of single photons and understanding the differences between the predictions of a quantum and a classical field theory[1–3] played pivotal role in development of quantum optics and quantum information. In recent years experiments that follow this trail, but involving phonons instead of photons, were performed. I hope to motivate why it makes sense to pursue this task of quantum control of micromechanical resonators like it has been done for optical fields.

Demonstrating quantum effects with mechanical resonators is not a straightforward task, primarily because of their linearity and somewhat low frequency. These properties are the main reason that quantum experiments with mechanical resonators are a young research field. Because of the linearity, most quantum experiments involving micromechanical resonators use another quantum system to make them behave non-classically. All this suggests we can expect that mechanical resonators will be useful for quantum technology only when integrated along with another quantum system. Despite of this somewhat sidekick role, this chapter aims to show that there is potential for mechanical resonators to make an impact on the development of quantum technologies.

The same way current computation and communication uses several technologies, it is reasonable to expect that the same is what might happen with their quantum counterparts. Mechanical resonators might be well suited for the task of connecting quantum technologies because of their ability to couple to electromagnetic modes in wide frequency spectrum, but also to various other quantum systems (superconducting qubits[4], ultracold atoms[5], NV centers[6]...). Quantum procesors that operate with microwave frequencies (like superconducting qubits) are usually contained in dilution fridge without the ability to communicate with other distant quantum processors. Faithful conversion of quantum information between optical and microwave modes means that one could exchange information among these processors over long distances. This type of device that can transmit quantum information between various quantum hardware is called a quantum transducer. Most mechanical devices so far have been designed to interact only with one quantum system. This is slowly changing and designing mechanical resonator with good coupling to both optical and microwave resonators has become a hot research topic in recent years [7–9]. Besides the ability to exchange quantum information with various systems, mechanical resonators could be used to store quantum information as well[10, 11], as their lifetimes extend into time scale of seconds[12]

Besides this application driven side of research, fundamental interest in non-classical states of massive objects exists, as the question of boundary between quantum and classical physics is still open. Because of their large particle number and large mass, micromechanical resonators with experimentally accessible non-classical states are well suited hardware to test modifications to quantum mechanics[13–15].

1.2. WHY OPTOMECHANICS?

This thesis will concentrated on interfacing mechanical with optical¹ resonators, which is the main focus of the field of cavity optomechanics[16]. The interaction is intrinsi-

¹More precisely we work with infrared (about 1550nm) resonators, but in this thesis I will often refer to it as optical

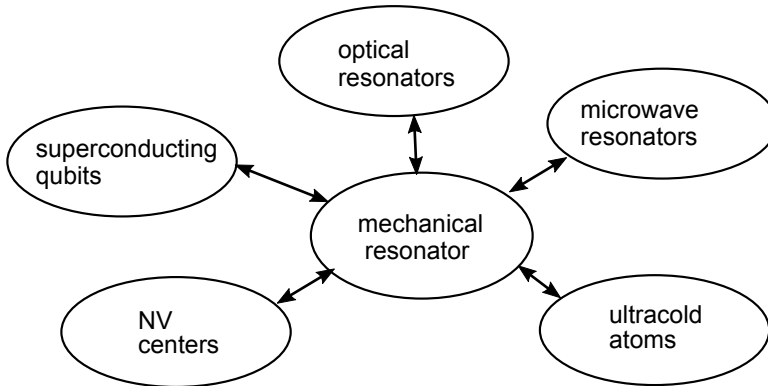


Figure 1.1: Mechanical resonators can coherently interact with many quantum systems that are seen as hardware candidates for quantum computing and communication.

cally nonlinear and one can expect rich quantum dynamics[17]. Still, the nonlinearity in the systems created so far was small enough that interaction takes a linear character. Despite this, optomechanics at optical and infra-red frequencies has already produced several milestone experiments like cooling mechanical resonator to the ground state and squeezed light generation[18, 19].

As mentioned in the previous section mechanical resonators couple to various physical systems (Fig. 1.1), giving them high potential for wide application as detectors as well. On the other hand light interferometers are known as a good way of detecting small variations in position. Detecting the motion of mirrors using light has been a driving force for optomechanics[16, 20]. In our research, we wish to exploit another quality of optomechanical system, and that is a good combination of a system that can transmit and a system that can store information. This type of interface is exactly what is needed for achieving long-distance quantum networks via quantum repeaters[21]. Additionally, optomechanics is an interesting approach for quantum communication because of the ability to design optomechanical devices of a wide range of wavelength, including wavelengths used in standard telecommunication that have low propagation losses. Usually, one can place many optomechanical devices on a single chip and design them such that they have different frequency and that way achieve multiplexing.

1.3. WHY THIS THESIS?

Previous optomechanics experiments with micromechanical resonator mostly operated in a regime where the state of the mechanical resonator was dominated by thermal noise. A higher level of control is needed in order to be able to use mechanical resonator for quantum applications. Previous research with similar optomechanical devices[22] showed that this might not be possible due to the heating of structure from laser light.

This thesis experimentally demonstrates the control of a quantum state of micromechanical resonators with laser pulses, with a goal of laying the groundwork for applications of mechanical resonators in quantum technologies.

1 Quantum experiment demonstrating entanglement between bulk phonons in diamond has been already conducted[23]. By performing similar experiments on an engineered system we want to bring mechanical resonators closer to a useful technology. With devices presented in this thesis there is much more freedom in choosing mechanical and optical frequencies and lifetimes, as well as the coupling between two resonators. In this thesis I will focus on two experiments published in [24, 25]. Additionally our team has performed an experiment demonstrating the entanglement of two mechanical modes in [26].

REFERENCES

- [1] H. J. Kimble, M. Dagenais, and L. Mandel, *Photon antibunching in resonance fluorescence*, Phys. Rev. Lett. **39**, 691 (1977).
- [2] J. F. Clauser, *Experimental distinction between the quantum and classical field-theoretic predictions for the photoelectric effect*, Phys. Rev. D **9**, 853 (1974).
- [3] S. J. Freedman and J. F. Clauser, *Experimental test of local hidden-variable theories*, Phys. Rev. Lett. **28**, 938 (1972).
- [4] A. D. O'Connell, M. Hofheinz, M. Ansmann, R. C. Bialczak, M. Lenander, E. Lucero, M. Neeley, D. Sank, H. Wang, M. Weides, J. Wenner, J. M. Martinis, and A. N. Cleland, *Quantum ground state and single-phonon control of a mechanical resonator*, Nature **464**, 697 (2010).
- [5] S. Camerer, M. Korppi, A. Jckel, D. Hunger, T. W. Hnsch, and P. Treutlein, *Realization of an optomechanical interface between ultracold atoms and a membrane*, Phys. Rev. Lett. **107**, 223001 (2011).
- [6] O. Arcizet, V. Jacques, A. Siria, P. Poncharal, P. Vincent, and S. Seidelin, *A single nitrogen-vacancy defect coupled to a nanomechanical oscillator*, Nat Phys **7**, 879 (2011).
- [7] R. W. Andrews, R. W. Peterson, T. P. Purdy, K. Cicak, R. W. Simmonds, C. A. Regal, and K. W. Lehnert, *Bidirectional and efficient conversion between microwave and optical light*, Nature Phys. **10**, 321 (2014).
- [8] K. C. Balram, M. Davanço, J. Y. Lim, J. D. Song, and K. Srinivasan, *Moving boundary and photoelastic coupling in GaAs optomechanical resonators*, Optica **1**, 414 (2014).
- [9] J. Bochmann, A. Vainsencher, D. D. Awschalom, and A. N. Cleland, *Nanomechanical coupling between microwave and optical photons*, Nature Phys. **9**, 712 (2013).
- [10] V. Fiore, Y. Yang, M. C. Kuzuk, R. Barbour, L. Tian, and H. Wang, *Storing Optical Information as a Mechanical Excitation in a Silica Optomechanical Resonator*, Phys. Rev. Lett. **107**, 133601 (2011).
- [11] A. N. Cleland and M. R. Geller, *Superconducting qubit storage and entanglement with nanomechanical resonators*, Phys. Rev. Lett. **93**, 070501 (2004).

- [12] G. S. MacCabe, H. Ren, J. Luo, J. D. Cohen, H. Zhou, A. Sipahigil, M. Mirhosseini, and O. Painter, *Phononic bandgap nano-acoustic cavity with ultralong phonon lifetime*, arXiv e-prints, arXiv:1901.04129 (2019), arXiv:1901.04129 [cond-mat.mes-hall].
- [13] W. Marshall, C. Simon, R. Penrose, and D. Bouwmeester, *Towards Quantum Superpositions of a Mirror*, Phys. Rev. Lett. **91**, 130401 (2003).
- [14] M. Bahrani, M. Paternostro, A. Bassi, and H. Ulbricht, *Proposal for a noninterferometric test of collapse models in optomechanical systems*, Phys. Rev. Lett. **112**, 210404 (2014).
- [15] S. Nimmrichter, K. Hornberger, and K. Hammerer, *Optomechanical sensing of spontaneous wave-function collapse*, Phys. Rev. Lett. **113**, 020405 (2014).
- [16] M. Aspelmeyer, T. J. Kippenberg, and F. Marquardt, *Cavity optomechanics*, Rev. Mod. Phys. **86**, 1391 (2014).
- [17] P. Rabl, *Photon blockade effect in optomechanical systems*, Phys. Rev. Lett. **107**, 63601 (2011).
- [18] J. Chan, T. P. M. Alegre, A. H. Safavi-Naeini, J. T. Hill, A. Krause, S. Gröblacher, M. Aspelmeyer, and O. Painter, *Laser cooling of a nanomechanical oscillator into its quantum ground state*, Nature **478**, 89 (2011).
- [19] A. H. Safavi-Naeini, S. Gröblacher, J. T. Hill, J. Chan, M. Aspelmeyer, and O. Painter, *Squeezed light from a silicon micromechanical resonator*, Nature **500**, 185 (2013).
- [20] C. M. Caves, *Quantum-mechanical radiation-pressure fluctuations in an interferometer*, Phys. Rev. Lett. **45**, 75 (1980).
- [21] L. M. Duan, M. D. Lukin, J. I. Cirac, and P. Zoller, *Long-distance quantum communication with atomic ensembles and linear optics*. Nature **414**, 413 (2001).
- [22] J. D. Cohen, S. M. Meenehan, G. S. MacCabe, S. Gröblacher, A. H. Safavi-Naeini, F. Marsili, M. D. Shaw, and O. Painter, *Phonon counting and intensity interferometry of a nanomechanical resonator*, Nature **520**, 522 (2015).
- [23] K. C. Lee, M. R. Sprague, B. J. Sussman, J. Nunn, N. K. Langford, X.-M. Jin, T. Champion, P. Michelberger, K. F. Reim, D. England, D. Jaksch, and I. Walmsley, *Entangling macroscopic diamonds at room temperature*. Science **334**, 1253 (2011).
- [24] S. Hong, R. Riedinger, I. Marinković, A. Wallucks, S. G. Hofer, R. A. Norte, M. Aspelmeyer, and S. Gröblacher, *Hanbury Brown and Twiss interferometry of single phonons from an optomechanical resonator*, Science **358**, 203 (2017).
- [25] I. Marinković, A. Wallucks, R. Riedinger, S. Hong, M. Aspelmeyer, and S. Gröblacher, *Optomechanical bell test*, Phys. Rev. Lett. **121**, 220404 (2018).
- [26] R. Riedinger, A. Wallucks, I. Marinković, C. Löschnauer, M. Aspelmeyer, S. Hong, and S. Gröblacher, *Remote quantum entanglement between two micromechanical oscillators*, Nature **556**, 473 (2018).

2

BASICS OF OPTOMECHANICS

Igor Marinković

This chapter introduces a basic theory of sideband resolved optomechanics and correlation functions of optical and mechanical modes.

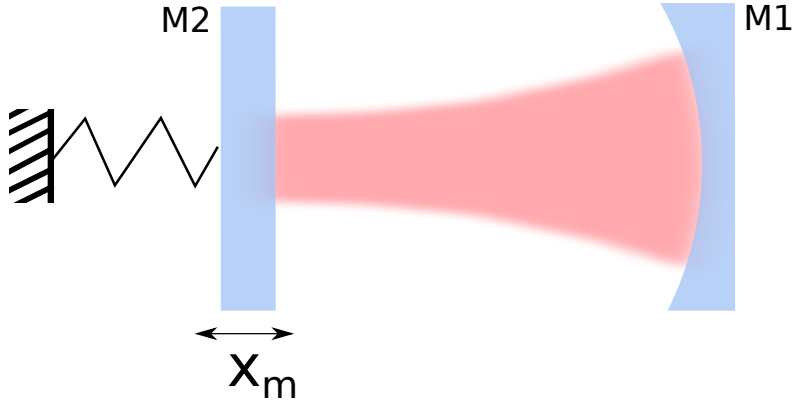


Figure 2.1: Generic optomechanical system, where motion of one of the mirrors modulates the length of the optical cavity.

2.1. INTRO TO OPTOMECHANICS

This thesis deals with one of the simplest yet very important concept in physics - the Harmonic oscillator. We will investigate two coupled harmonic oscillators. One them will be mechanical in nature and simple to imagine-a mass on a spring. The other one is somewhat more complex and electromagnetic in nature. It will be an optical cavity. To make things a bit more advanced we will look into experiments where the quantum description of nature has to be evoked in order to explain results produced by coupling of these two oscillators.

In this section I will outline the basics of the theory of optomechanics that can be found in more detail in references [1–3]. We mostly follow [1]. Then I will briefly present measures that are commonly used in quantum optics to demonstrate non-classical behaviour of harmonic oscillator (for further reading please look at any textbook on quantum optics e.g. [4]).

2.1.1. OPTOMECHANICAL HAMILTONIAN

Let's consider the following experimental situation given in Fig. 2.1. An optical cavity (frequency $\omega_c/2\pi$) is formed by two mirrors, where one of them (M2) is connected with a spring to a fixed wall (Fig. 2.1) and acts as a harmonic oscillator of mass m and resonant frequency $\omega_m/2\pi$. Hamiltonian of uncoupled systems is:

$$\hat{H} = \hbar\omega_m\hat{b}^\dagger\hat{b} + \hbar\omega_c\hat{c}^\dagger\hat{c} \quad (2.1)$$

where \hat{b} and \hat{c} are annihilation operators for the mechanical and optical mode respectively. Frequency of the optical resonance is determined by the length of the cavity and therefore a change in position of M2 (x_m) will modulate the resonant frequency of the optical cavity. We can expand $\omega_c(x_m)$ in a Taylor series around zero:

$$\omega_c(x_m) = \omega_c(0) + \left. \frac{\partial\omega_c(x_m)}{\partial x_m} \right|_0 x_m + \dots$$

If we consider only elements up to first order of the Taylor expansion, the Hamiltonian describing this interaction is given by:

$$\hat{H} = \hbar\omega_m \hat{b}^\dagger \hat{b} + \hbar\omega_c(0) \hat{c}^\dagger \hat{c} + \hbar g_0 (\hat{b}^\dagger + \hat{b}) \hat{c}^\dagger \hat{c}, \quad (2.2)$$

where $g_0 = \left. \frac{\partial \omega_c(x_m)}{\partial x_m} \right|_0 x_{zpf}$ is called the single photon coupling and can be interpreted as the shift in optical frequency due to motion of the mirror by the zero point fluctuation:

$$x_{zpf} = \sqrt{\frac{\hbar}{2m\omega_m}}.$$

Where we have used the following link between position operator and creation and annihilation operators:

$$\hat{x}_m = x_{zpf} (\hat{b} + \hat{b}^\dagger). \quad (2.3)$$

2.1.2. LINEARIZED HAMILTONIAN

In experiments we will always drive (pump) the optical resonator with one input laser field (frequency $\omega_l/2\pi$) at a time. Using the unitary transformation $\hat{U}(t) = e^{i\omega_l t \hat{c}^\dagger \hat{c}}$. We can move into a frame rotating with drive frequency:

$$\hat{H}_{rf} = \hbar\omega_m \hat{b}^\dagger \hat{b} - \hbar\Delta \hat{c}^\dagger \hat{c} + \hbar g_0 (\hat{b}^\dagger + \hat{b}) \hat{c}^\dagger \hat{c}, \quad (2.4)$$

where $\Delta = \omega_l - \omega_c(0)$ is the detuning of the drive laser with respect to the cavity. At this point we have to take into account that optical cavity will always be coupled to external modes. In all physical realizations interaction of optical cavity with external modes is stronger than optomechanical coupling. In this case we can linearize the optical field around mean value such that $\hat{c} = \alpha + \hat{a}$, where α is chosen to be real. For devices with small non-linearity (g_0 smaller than the optical cavity decay rate κ and mechanical frequency ω_m) we will neglect terms that are not enhanced by α . Also we will neglect the effect of constant shift to optical resonance. We obtain the final form of linearised Hamiltonian:

$$\hat{H}_l = \hbar\omega_m \hat{b}^\dagger \hat{b} - \hbar\Delta \hat{a}^\dagger \hat{a} + \hbar g_0 (\alpha \hat{a}^\dagger + \alpha \hat{a}) (\hat{b}^\dagger + \hat{b}). \quad (2.5)$$

Though we now have a linear Hamiltonian, the interaction is now enhanced by the amplitude of the mean intracavity field, meaning we can tune the coupling by the power of our pump laser.

2.1.3. ACTION OF OPTOMECHANICAL HAMILTONIAN

Looking at equation 2.5, we see that the initial nonlinear Hamiltonian is now replaced with linear interaction between two resonators with frequencies ω_m and Δ . In order to make interaction resonant, absolute detuning of drive laser should be equal to the mechanical frequency. At this point pump light only determines the coupling strength and effective frequency of the optical resonator, but what happens to pump photons is not much of our concerns. Here photons of laser pump beam are removed from quantum picture and we assume that optomechanical interaction has a negligible effect on the state of the strong pump beam. If we operate in the sideband resolved regime ($\omega_m \gg \kappa$)

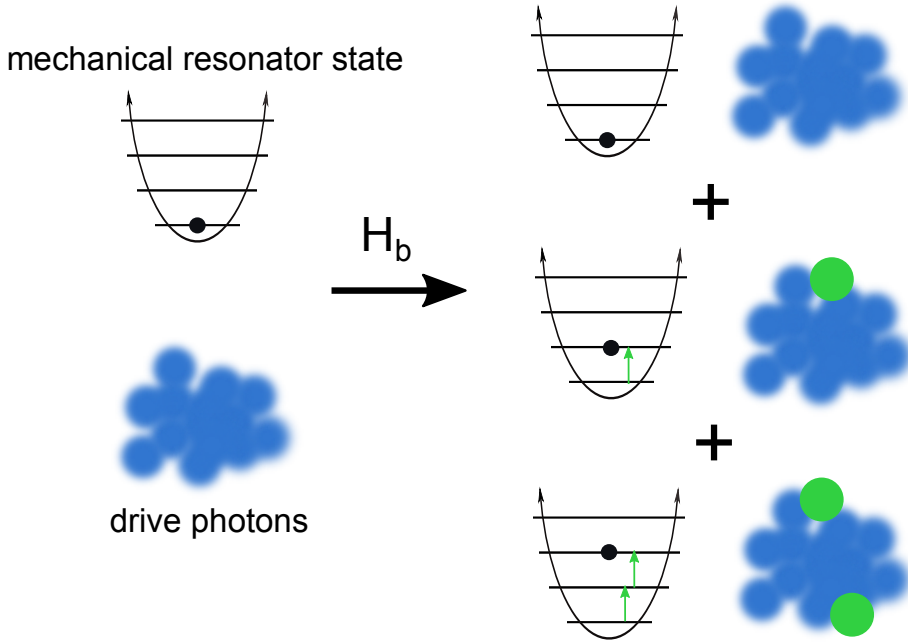


Figure 2.2: Blue are photons coming from laser. Green are on resonance inside cavity. We start with both mechanical and optical resonator in ground state (no phonons, no green photons). Whenever a green photon is created, mechanical resonator will go up by 1 excitation on level diagram. When laser pulse containing photons interacts with mechanical resonator superposition of different number of particle pairs is created. Probabilities associated with excitations can be controlled by number of blue photons.

we can selectively drive the transitions that increase or decrease number of excitations in mechanical resonator (Fig. 2.4). If the pump laser is blue detuned ($\Delta = \omega_m$) optical resonator has effective negative frequency and we keep only energy preserving terms, so Hamiltonian can be approximated using rotating wave approximation[5]

$$\hat{H}_b = \hbar g_0 \alpha (\hat{a}^\dagger \hat{b}^\dagger + \hat{a} \hat{b}). \quad (2.6)$$

This is known in quantum optics as two mode squeezing Hamiltonian (Fig. 2.2). We consider special case when both mechanical and optical resonators are in ground state. In the ideal case of no losses, mechanical (m) and resonant optical mode (o) after weak blue detuned laser pulse:

$$|\psi\rangle_b \rightarrow (|0\rangle_o |0\rangle_m + \epsilon_b |1\rangle_o |1\rangle_m + \mathcal{O}(\epsilon_b^2)), \quad (2.7)$$

where $\epsilon_b^2 \ll 1$ is excitation probability that can be tuned by number of blue detuned photons (see next section for explicit expression). We can see that as a result of blue pulse we have created entanglement between optical and mechanical mode. In simple words we create phonons and photons as pairs and the final state is a superposition of having 0

or 1 or 2... pairs of particles. As this interaction entangles optical and mechanical modes, it will be starting point for all our protocols.

On the other hand, if the pump laser is red detuned from the optical cavity resonance we obtain so called beam splitter Hamiltonian:

$$\hat{H}_r = \hbar g_0 \alpha (\hat{a}^\dagger \hat{b} + \hat{a} \hat{b}^\dagger). \quad (2.8)$$

We can describe this interaction as transfer of quantum state from one mode to another. As the name suggests this is equivalent to optical beam splitter, with the exception that one of the input and one of the output modes are mechanical rather than optical (Fig. 2.3). As already mentioned the coupling between the optical and mechanical mode is determined by pump light, we can use amount of pump light to tune the reflectivity of the splitter. This part of Hamiltonian is crucial for wavelength conversion protocols.

In experiments in this thesis the beam splitter Hamiltonian will be used to transfer the state of mechanical resonator onto the optical mode (Fig. 2.3). This means that we can use sophisticated optical detection apparatus in order to measure the mechanical degree of freedom. If we start with state $|0\rangle_o |\psi\rangle_m$ of optical (o) and mechanical mode (m), under beam splitter interaction this state will evolve towards $|\psi\rangle_o |0\rangle_m$ in the limit of complete state transfer. If only partial state transfer is achieved we have the case that beam splitter is partially reflective. The expression for reflectivity (ϵ_r^2) is given in next section. In case of $\epsilon_r < 1$ and if the state of the mechanical resonator is not detected by some other means we have to trace out the mechanics, leading us to a mixed state of the optics.

The interaction of blue and red detuned light with the mechanical resonator can be seen also the way presented in Fig. 2.4.

2.2. OPEN DYNAMICS

In actual optical cavities the field will always leak out of the cavity. We can still consider the cavity to be a single mode, but coupled linearly to the continuum of optical modes in the ground state¹ [4]. Additionally mechanical frequency is orders of magnitude smaller than frequency difference from other nearest optical mode, so we don't expect coupling between optical modes due to mechanics. Optomechanical state after two mode squeezing laser pulse acting on optomechanical system in ground state is derived in [7, 8] using Langevin equations, with assumption of over-coupled cavity i.e. cavity losses are dominated by coupling to external modes over which we have control (input coupling rate equal to total loss rate: $\kappa_e \approx \kappa$). Still we can use this result in our case with small modifications. When going from completely overcoupled to partially coupled cavity we have to correct the intracavity pump power. We can still write the state of mechanics and scattered field from cavity after pumped by blue detuned laser pulse as two mode squeezed state having excitation probability as derived in [8] with correction for intracavity photon

¹Approach valid for high Q resonators[6]

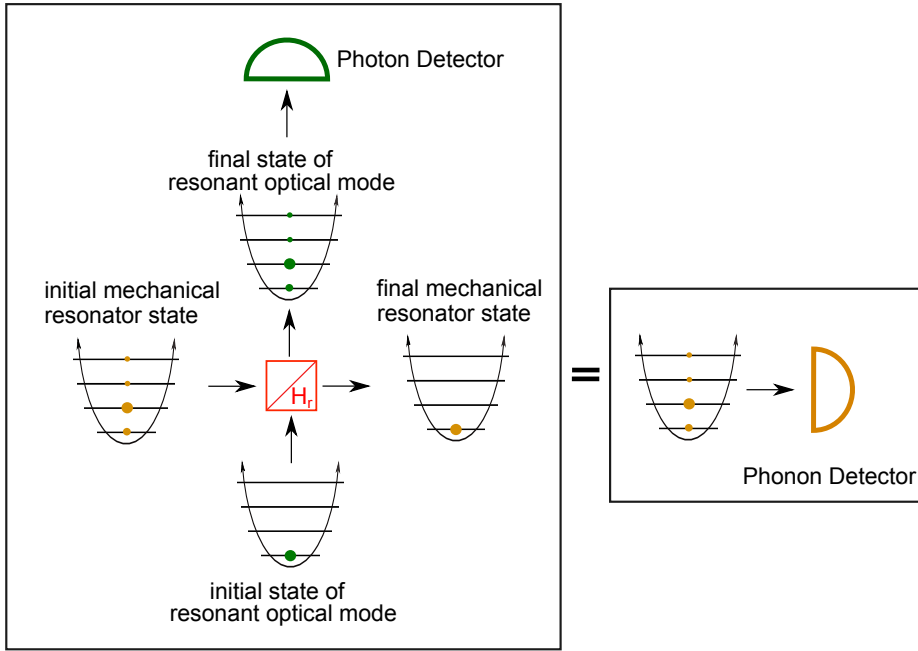


Figure 2.3: Red detuned pumping of optical resonator can be visualized as beam splitter where one of the inputs (outputs) is optical and other is mechanical. In the limit of perfect reflectivity (optomechanical scattering probability $\epsilon_r^2 \rightarrow 1$), after the red pump we will have mechanical resonator in ground state while optical mode will contain state that was previously in mechanical resonator. If we then detect output optical mode, it is effectively as if we measured initial mechanical mode with phonon detector. Since we do not possess such a device, we always transfer state of mechanical mode onto optical mode and perform detection with single photon detectors.

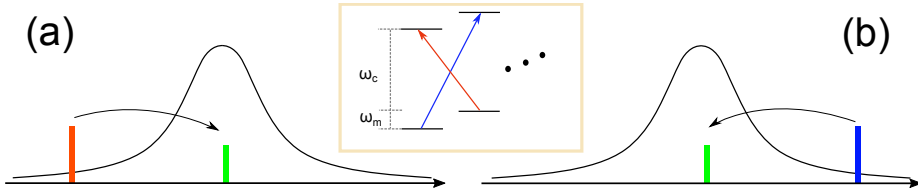


Figure 2.4: Optomechanical scattering of light red (a) and blue (b) detuned from optical resonance (black line). In order to become resonant with the cavity, red (blue) pump photons take (give away) energy from (to) mechanical resonator. Inset: Energy levels of optomechanical system. If we operate in sideband resolved regime we can selectively drive transitions that increase or decrease number of mechanical excitations. Process in (a) is also called anti-Stokes scattering, while process in (b) is also referred to as Stokes scattering.

number:

$$\begin{aligned} \epsilon_b^2 &= \exp\left(\frac{\kappa_e}{\kappa} \frac{4g_0^2 E_p}{\hbar\omega_l(\omega_m^2 + (\kappa/2)^2)}\right) - 1 \\ &\approx \frac{\kappa_e}{\kappa} \frac{4g_0^2 E_p}{\hbar\omega_l(\omega_m^2 + (\kappa/2)^2)} \quad \text{for } \epsilon_b^2 \ll 1 \end{aligned} \quad (2.9)$$

where E_p is energy of the pulse. Another correction is needed as the two mode squeezed state contains optical radiation modes that we do not have access to. These modes have to be traced out such that a mixed state is created. We can model this by acting onto the state with beam splitter with transmission given by cavity collection efficiency and tracing out modes that are inaccessible. So basically our detection efficiency is lower by κ_e/κ . Full derivation of Equation 2.9 can be found in [3]. Leak of phonons from the mechanical resonator can be treated in similar fashion to optical mode scattering losses. Still, experiments in this thesis are performed on timescale much shorter than the lifetime of mechanical resonator, so mechanical losses can be neglected. Similarly to scattering probability of two mode squeezing process, we can correct result obtained in [8] scattering probability of red detuned pulse (beam splitter reflectivity):

$$\epsilon_r^2 = 1 - \exp\left(-\frac{\kappa_e}{\kappa} \frac{4g_0^2 E_p}{\hbar\omega_l(\omega_m^2 + (\kappa/2)^2)}\right).$$

Important additional assumption used for deriving these equations is that $g_0\alpha \ll \kappa$ [8], which set time limit for how fast we can transfer state between mechanics and optics (Fig. 2.3). Also pulses should be much slower than $1/\kappa$ such that there are no pulse distortions due to finite cavity linewidth.

2.3. QUANTUM EXPERIMENTS OF HARMONIC OSCILLATOR

Infra-red and optical photons are prime candidates for implementing quantum communication protocol. There are several benchmark experiments that one can perform on the road towards creating quantum technology that uses photons. Prominent measures that we will also use in this thesis to demonstrate quantum phenomena of mechanical resonators are Hanbury-Brown twiss interferometry, Cauchy Schwarz inequality² and Bell inequality. As we saw in the previous chapter we can use optomechanical beamsplitter Hamiltonian to transfer quantum state from the mechanical to optical resonator. That way we can utilize techniques used to demonstrate the nonclassicality of optical oscillator to establish nonclassical behaviour of the mechanical oscillator.

2.3.1. SIDEBAND ASYMMETRY

One of the common requirements for showing quantum behaviour of mechanical resonators is removing thermal excitations. For high frequency (GHz) resonators in dilution refrigerator (≈ 20 mK) the average number of thermal excitations should be negligible. In order to confirm this we can perform sideband asymmetry[9] (Fig. 2.5(a)). We send repeatedly weak ($\epsilon_b \ll 1$) blue detuned pulse to the mechanical resonator and count how many on resonant photons are created in the interaction of the pulse with the mechanics. We then perform the same measurement also for red detuned pulses with the same input pulse length and same average number of photons as blue pulses. We wait inbetween each pulse such that mechanical resonator can rethermalize with the

²Measurement of Cauchy Schwarz inequality with optomechanical devices has already been demonstrated[9], still I will describe it here as we will make use of it in Bell experiment.

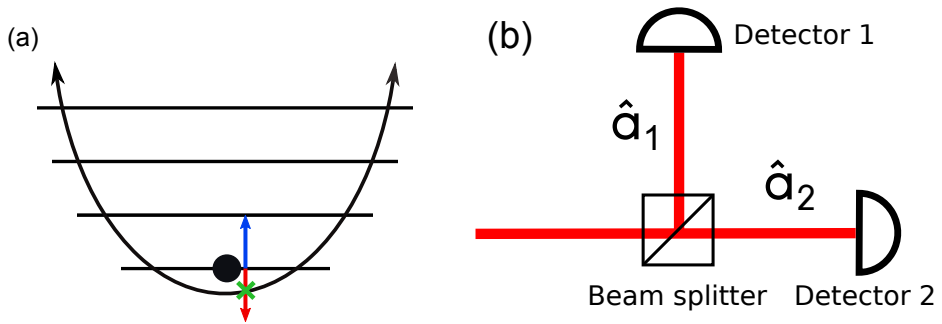


Figure 2.5: (a) Mechanical resonator is in lowest possible energy state so photons can not gain any energy to become resonant with cavity. This is not the case for blue detuned photons that instead need to give away energy to become resonant. (b) Hanbury Brown Twiss interferometry is performed using beam splitter and two single photon detectors.

environment. The number of thermal excitations can be determined as[9]

$$n_{th} = \frac{\Gamma_r}{\Gamma_b - \Gamma_r} \quad (2.10)$$

where Γ_b and Γ_r are rates at which resonant photons are created when device is pumped with blue and red detuned light respectively. Intuitively this asymmetry in scattering of blue and red detuned light can be seen as following. If the mechanical resonator is in the ground state it has no excitations to give to the light, so photons can not upconvert to become resonant with the cavity. On the other hand the mechanical resonator can always receive excitations from blue-detuned light and in that case photons can downconvert to become resonant with the cavity Fig. 2.5(a).

The number of thermal excitations is an important number that characterizes our experiment and that is easy to measure. As it will be shown in later chapters sideband asymmetry can be used to estimate the results of quantum experiments. It is important to make sure that the intra-cavity pulse powers for blue and red pulses are the same and that the detection probability is the same for both. In the case of counting scattered photons, one also needs to filter out photon of the pump pulses. Additionally we assume that pump light at the cavity frequency is in a vacuum state, therefore any technical noise at these frequencies can result in wrong measurement of temperature.

2.3.2. HANBURY BROWN AND TWISS INTERFEROMETRY

One can distinguish between certain types of quantum states of light by evaluating its second order autocorrelation function at time delay τ , defined as:

$$g_{oo}^{(2)}(\tau) = \frac{\langle \hat{a}^\dagger(0) \hat{a}^\dagger(\tau) \hat{a}(\tau) \hat{a}(0) \rangle}{\langle \hat{a}^\dagger(\tau) \hat{a}(\tau) \rangle \langle \hat{a}^\dagger(0) \hat{a}(0) \rangle} \quad (2.11)$$

It can be shown[4] that commonly occurring coherent states and their incoherent mixtures satisfy following inequality $g_{oo}^{(2)}(\tau) \geq 1$. As this inequality is also predicted by semi-

classical theories³ of photodetection, the states that do not follow this inequality we call non-classical. An example of this state is the single excitation Fock state that has $g_{oo}^2(0) = 0$. Generating single excitations in optical modes is of high importance for quantum communication[11] and Hanbury Brown and Twiss interferometry became standard way of determining the quality of single photon source.

This second order autocorrelation function can be measured by performing Hanbury Brown and Twiss interferometry (Fig. 2.5b). The idea is to split the beam of light in two and send it to two single photon detectors. By sending the sending the light through the beam splitter and detecting two output modes (a_1 and a_2) on two detectors we can measure:

$$g_{12}^{(2)}(0) = \frac{\langle \hat{a}_1^\dagger \hat{a}_2^\dagger \hat{a}_1 \hat{a}_2 \rangle}{\langle \hat{a}_1^\dagger \hat{a}_1 \rangle \langle \hat{a}_2^\dagger \hat{a}_2 \rangle}, \quad (2.12)$$

where the numerator is the expectation value of coincidences between two detectors (chapter 12 in [12]), while the denominator is the product of the expectation values of number of individual clicks of detectors. Since the other input port of the beam splitter is in vacuum state we get $g_{12}^{(2)}(0) = g_{oo}^{(2)}(0)$.

If the optical mode is truly populated by a single photon, one should observe no coincidence clicks between two detectors. On the other hand a semiclassical theory predicts that there will be equal light intensity at both detectors, therefore coincidences are possible[10]. The same reasoning can be applied to mechanical waves and therefore we also use Hanbury Brown and Twiss for checking the non-classical nature of mechanical excitations. We can then define second order correlation function of mechanical mode in terms of its annihilation operator as:

$$g_{mm}^{(2)}(\tau) = \frac{\langle \hat{b}^\dagger(0) \hat{b}^\dagger(\tau) \hat{b}(\tau) \hat{b}(0) \rangle}{\langle \hat{b}^\dagger(\tau) \hat{b}(\tau) \rangle \langle \hat{b}^\dagger(0) \hat{b}(0) \rangle},$$

satisfying the same non-classicality condition as its optical counterpart.

2.3.3. CAUCHY SCHWARZ INEQUALITY

Now let's consider an experiment involving two optical mode (\hat{a}_A and \hat{a}_B) and each one is divided and sent to a pair of detectors. We can define the cross correlation function for these two modes as:

$$g_{AB}^{(2)}(0) = \frac{\langle \hat{a}_A^\dagger \hat{a}_B^\dagger \hat{a}_B \hat{a}_A \rangle}{\langle \hat{a}_A^\dagger \hat{a}_A \rangle \langle \hat{a}_B^\dagger \hat{a}_B \rangle} \quad (2.13)$$

Initially this measurement was also used to disprove semiclassical theories of photodetection, as using the Cauchy-Schwarz inequality it can be proven that classical fields follow the inequality[10]:

$$g_{AB}^{(2)} < \sqrt{g_{AA}^{(2)} g_{BB}^{(2)}}$$

where $g_{AA}^{(2)}$, $g_{BB}^{(2)}$ are the second order correlations for each of two modes (as described in the previous section).

³Semiclassical theories treat the detector as a quantum object, while the light is treated like a classical field[10]

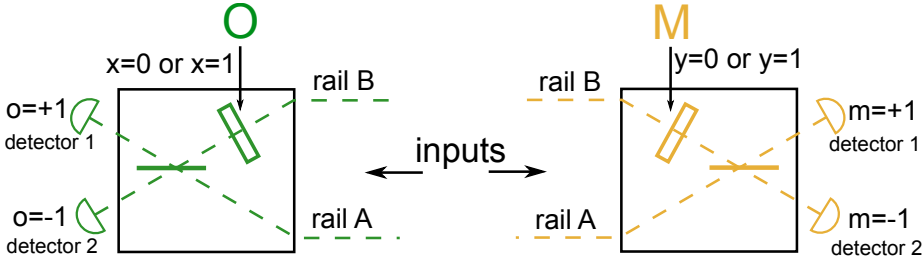


Figure 2.6: Idealistic depiction of an optomechanical Bell test. Two entangled particles photon (green) and phonon (orange) are each sent to distant measurement apparatus. States are encoded such that e.g. $|A\rangle_o$ represents photon coming in through rail A and $|B\rangle_m$ represents phonon coming in through rail B. Phase in A arms of both photon and phonon can be changed using phase shifters. These are the settings (x and y) used for Bell measurement. The result of optical interference is measured on single photon detector and the result of mechanical interference on single phonon detector (let's assume we have such a device). At each setup measurement results are assigned the following way: if detector 1 clicks we record result +1, likewise click of detector 2 corresponds to result -1. Equivalent experiment in purely optical regime (4 optical modes) has been demonstrated[16].

In the following chapters we will use it to evaluate the correlations between the optical and mechanical mode after the action of the two mode squeezing Hamiltonian. Definition of optical cross correlation can easily be changed to optomechanical:

$$g_{om}^{(2)}(0) = \frac{\langle \hat{a}^\dagger \hat{b}^\dagger \hat{b} \hat{a} \rangle}{\langle \hat{a}^\dagger \hat{a} \rangle \langle \hat{b}^\dagger \hat{b} \rangle}. \quad (2.14)$$

For the ideal state given in Equation 2.7 we expect[13]:

$$g_{om}^{(2)} = 1 + 1/\epsilon_b^2$$

But thermal excitations will degrade this value. We can use the value of n_{th} to estimate $g_{om}^{(2)} \approx \frac{1+n_{th}}{n_{th}}$ [9].

Cross correlation was not only used as a measure to disprove semiclassical theories of photodetection, but it is also important benchmark[14] as certain minimum values are required in order to allow for the same setup to detect several more advanced quantum measures like the Bell inequality $g_{om}^{(2)} > 5.8$ [15].

2.3.4. BELL INEQUALITY

I will give a very short introduction to hidden variable theories and Bell theorem. Detailed discussion can be found [17], and we partially follow it here, for historic perspective refer to [18]. In this thesis we will deal with only one type of Bell inequality called CHSH (Clauser-Horne-Shimony-Holt) inequality, but I will often in this thesis refer to it simply as the Bell inequality as well.

Let's consider two particles (we will name them O and M) that are spatially separated and we have two potential settings at which we can measure the particles $x \in \{0, 1\}$; $y \in \{0, 1\}$. Two potential outcomes for each particle measurement $o = \pm 1$; $m = \pm 1$. Quantum mechanics predicts that the measurement on entangled states of two particles can lead to (anti-) correlation of the measurement results. Local hidden variable theories

try to explain the existence of the correlations by introducing hypothetical parameters λ , called hidden variables. If such variables exist, joint probability of obtaining certain results o and m for settings x and y ($p(o, m|x, y)$) can be factorized:

$$p(o, m|x, y, \lambda) = \int \rho(\lambda) p(o|x, \lambda) p(m|y, \lambda) d\lambda \quad (2.15)$$

where $\rho(\lambda)$ is a statistical distribution of the hidden variables. We now wish to evaluate the following expression

$$S = \langle o_0 m_0 \rangle + \langle o_0 m_1 \rangle + \langle o_1 m_0 \rangle - \langle o_1 m_1 \rangle, \quad (2.16)$$

where $\langle o_0 m_0 \rangle$ is the expectation value of the measurement of the quantity $o \cdot m$ when the measurement settings are kept at $x = 0, y = 0$. Using Equation 2.15 we have: $\langle o_x m_y \rangle = \int d\lambda \rho(\lambda) \langle o_x \rangle_\lambda \langle m_y \rangle_\lambda$. Finally we get:

$$S = \int d\lambda \rho(\lambda) \left[\langle o_0 \rangle_\lambda (\langle m_0 \rangle_\lambda + \langle m_1 \rangle_\lambda) + \langle o_1 \rangle_\lambda (\langle m_0 \rangle_\lambda - \langle m_1 \rangle_\lambda) \right]. \quad (2.17)$$

As the expression in the brackets can only yield ± 2 we get a final CHSH expression:

$$-2 \leq S \leq 2.$$

The locality condition is captured in the form of $\rho(\lambda), \langle o_x \rangle_\lambda$ and $\langle m_y \rangle_\lambda$. If the result of measurement of particle O depended on measurement settings of particle M we would write $\langle o_x \rangle_{\lambda, y}$, in which case we could not factorize S to get the form given in Equation 2.17.

Now let's show that quantum mechanics can provide result different to this one using the experiment shown in Fig. 2.6. Particle O is now chosen to be a photon and it is measured at apparatus O . The photon can arrive to apparatus through two optical modes (rails). States are encoded such that $|A\rangle_o$ represents photon in rail A, and state $|B\rangle_o$ labels photon being in other rail. Same labelling is used for apparatus M that receives particle M - a phonon. Let's consider case when entangled state $|AA\rangle_{om} + |BB\rangle_{om}$ is measured. Using phase shifters this state can be transformed into:

$$|AA\rangle_{om} + e^{i\phi_o + i\phi_m} |BB\rangle_{om}$$

where ϕ_o and ϕ_m are phases added in rails B for optical and mechanical mode respectively.

After the beam splitter, the photon can end up in front of detector 1 ($|1\rangle$) or detector 2 ($|2\rangle$). The states passing the beam splitter are transformed $|A\rangle \rightarrow |1\rangle + i|2\rangle$ and $|B\rangle \rightarrow i|1\rangle + |2\rangle$, meaning the resulting state is

$$\begin{aligned} |\Phi\rangle &= \frac{1}{2\sqrt{2}} \left[\left(1 - e^{i(\phi_o + \phi_m)}\right) \left(|1\rangle|1\rangle - |2\rangle|2\rangle\right) + i \left(1 + e^{i(\phi_o + \phi_m)}\right) \left(|1\rangle|2\rangle + |2\rangle|1\rangle\right) \right] \\ &= \frac{1}{\sqrt{2}} \left[\sin\left(\frac{\phi_o + \phi_m}{2}\right) \left(|1\rangle|1\rangle - |2\rangle|2\rangle\right) + \cos\left(\frac{\phi_o + \phi_m}{2}\right) \left(|1\rangle|2\rangle + |2\rangle|1\rangle\right) \right], \quad (2.18) \end{aligned}$$

with the global phase factor dropped. We make labels on each setup such that if detector $|1\rangle$ clicks we assign the measurement result $+1$, likewise click on $|2\rangle$ produces result -1 . We can evaluate expectation value $\langle o_x m_y \rangle = \sin^2\left(\frac{\phi_o + \phi_m}{2}\right) - \cos^2\left(\frac{\phi_o + \phi_m}{2}\right)$. We select that measurements settings $x \in \{0, 1\}$ to correspond to $\phi_o = 0$ and $\phi_o = \pi/2$, while $y \in \{0, 1\}$ correspond to $\phi_m = -\pi/4$ and $\phi_m = \pi/4$. With these we obtain $|S| = 2\sqrt{2}$. The experiment is repeated many times and we need to record on what detector photon/phonon ended for each experiment run. Then we need to count how many times same and opposite detectors clicked. Using these number we can evaluate the expectation value by counting coincidences:

$$\begin{aligned} \langle o_x m_y \rangle &= p(o = 1, m = 1) + p(o = -1, m = -1) - p(o = 1, m = -1) - p(o = -1, m = 1) \\ &= \frac{n_{11} + n_{22} - n_{12} - n_{21}}{n_{11} + n_{22} + n_{12} + n_{21}}, \end{aligned}$$

where $p(o = 1, m = 1)$ (x and y omitted) is the probability for outcomes $o = 1, m = 1$ and so on, while n_{ij} labels the number of times a photon was recorded at detector $i \in \{1, 2\}$ and a phonon was recorded at detector $j \in \{1, 2\}$.

We will show in Chapter 6 the actual experiment is performed such that we convert mechanical excitations in both mechanical rails into optical ones right before the phonon beam splitter. After that we can use optical components for measurement of phonon state. In order to simplify the experiment instead of spatially separating the detection of photon and phonon, detections are time separated. This is done so we can now use the same equipment for detecting the state of photons and phonons.

Bell inequality is not only interesting because of foundations of quantum mechanics, but it can be used as basis for quantum cryptography protocols[19, 20]. The ability of quantum hardware to violate Bell inequalities can be seen as an important benchmark test.

REFERENCES

- [1] M. Aspelmeyer, T. J. Kippenberg, and F. Marquardt, *Cavity optomechanics*, Rev. Mod. Phys. **86**, 1391 (2014).
- [2] C. K. Law, *Effective hamiltonian for the radiation in a cavity with a moving mirror and a time-varying dielectric medium*, Phys. Rev. A **49**, 433 (1994).
- [3] R. Riedinger, *Single Phonon Quantum Optics*, Ph.D. thesis, University of Vienna (2018).
- [4] D. F. Walls and G. J. Milburn, *Quantum Optics* (Springer, 1994).
- [5] M. D. et al., ed., *Quantum Machines: Measurement and Control of Engineered Quantum Systems* (Oxford University Press, 2011).
- [6] R. Lang, M. O. Scully, and W. E. Lamb, *Why is the laser line so narrow? a theory of single-quasimode laser operation*, Phys. Rev. A **7**, 1788 (1973).

- [7] C. Galland, N. Sangouard, N. Piro, N. Gisin, and T. J. Kippenberg, *Heralded Single-Phonon Preparation, Storage, and Readout in Cavity Optomechanics*, Phys. Rev. Lett. **112**, 143602 (2014).
- [8] S. G. Hofer, W. Wiczorek, M. Aspelmeyer, and K. Hammerer, *Quantum entanglement and teleportation in pulsed cavity optomechanics*, Phys. Rev. A **84**, 52327 (2011).
- [9] R. Riedinger, S. Hong, R. A. Norte, J. A. Slater, J. Shang, A. G. Krause, V. Anant, M. Aspelmeyer, and S. Gröblacher, *Non-classical correlations between single photons and phonons from a mechanical oscillator*, Nature **530**, 313 (2016).
- [10] J. F. Clauser, *Experimental distinction between the quantum and classical field-theoretic predictions for the photoelectric effect*, Phys. Rev. D **9**, 853 (1974).
- [11] C. H. Bennett and G. Brassard, *An update on quantum cryptography*, in *Advances in Cryptology* (Springer Berlin Heidelberg) pp. 475–480.
- [12] L. Mandel and E. Wolf, *Optical Coherence and Quantum Optics* (Cambridge University Press, 1995).
- [13] C. W. Chou, S. V. Polyakov, A. Kuzmich, and H. J. Kimble, *Single-photon generation from stored excitation in an atomic ensemble*, Phys. Rev. Lett. **92**, 213601 (2004).
- [14] A. Kuzmich, W. P. Bowen, A. D. Boozer, A. Boca, C. W. Chou, L.-M. Duan, and H. J. Kimble, *Generation of nonclassical photon pairs for scalable quantum communication with atomic ensembles*, Nature **423**, 731 (2003).
- [15] H. de Riedmatten, J. Laurat, C. W. Chou, E. W. Schomburg, D. Felinto, and H. J. Kimble, *Direct measurement of decoherence for entanglement between a photon and stored atomic excitation*, Phys. Rev. Lett. **97**, 113603 (2006).
- [16] J. G. Rarity and P. R. Tapster, *Experimental violation of Bells inequality based on phase and momentum*, Phys. Rev. Lett. **64**, 2495 (1990).
- [17] N. Brunner, D. Cavalcanti, S. Pironio, V. Scarani, and S. Wehner, *Bell nonlocality*, Rev. Mod. Phys. **86**, 419 (2014).
- [18] H. M. Wiseman and E. G. Cavalcanti, *Causarum Investigatio and the Two Bell's Theorems of John Bell*, arXiv e-prints, arXiv:1503.06413 (2015), arXiv:1503.06413 [quant-ph].
- [19] A. K. Ekert, *Quantum cryptography based on bell's theorem*, Physical Review Letters **67**, 661 (1991).
- [20] A. Acín, N. Gisin, and L. Masanes, *From Bells Theorem to Secure Quantum Key Distribution*, Phys. Rev. Lett. **97**, 120405 (2006).

3

OPTOMECHANICAL CRYSTAL NANOBEAM

Igor Marinković

While the previous chapter was dealing with a generic optomechanical system, in this chapter I will describe the particular optomechanical hardware used in this thesis - an optomechanical crystal nanobeam.

3.1. PHOTONIC CRYSTAL CAVITY

We showed in the previous chapters that our task is obtaining control of mechanical resonator at single phonon level using light. In this chapter I will first present the particular structure that we will use for our task and that is optomechanical crystal (OMC) nanobeam[1]. Why this particular design is used, will be discussed in the last section of this chapter. A detailed description of designing a nanobeam device can be found in [2]. For completeness, here I will give a short introduction. A starting point is a silicon nanowire that serves as a rectangular waveguide that can localize light in two directions by total internal reflection, as well as mechanical vibrations. This way optical and mechanical excitations can propagate along the nanowire. By patterning holes into it, one can create a mirror for both optical and mechanical excitations (so they become reflected). Holes are designed using crystal theory, such that they have both a mechanical and an optical bandgap (Fig. 3.1) at frequencies of excitations. Patterning two mirrors on the waveguide results in the formation of an optomechanical cavity, meaning confinement of mechanical and optical waves in all three dimensions. Two such mirrors can be placed close to each other so they form a small mode volume mechanical and optical resonators with a large overlap that will result in the high optomechanical coupling. The space between two mirrors is also filled with holes, but such that crystal in middle supports mode inside of bandgap of mirrors. This is done instead of a simple nanowire without holes between mirrors in order to minimize light scattering. As described in ([3]) sudden changes in the electric field of the optical mode will lead to a broad distribution of field in the momentum space. This is detrimental to the quality factor as more field will be inside the light cone, not satisfying the total internal reflection condition, and ultimately leading to large scattering of light into free space. Unlike the the generic system described in the previous chapter, moving boundary contribution to optomechanical coupling is secondary to photo-elastic coupling[2].

Though the same mirrors are used for optical and mechanical waves, independent control of mechanical from optical quality factor can be achieved. Phonon leakage from the cavity can be to some extent tuned[1, 4]. Surrounding the nanobeam with an additional phononic shield can lead to mechanical lifetimes as high as 1.5 seconds [5].

3.2. FIBER TO NANOBEAM COUPLING

It is important to have an efficient way to couple light from the laser to the nanobeams. We choose to deliver light from an optical fiber to the optical cavity of nanobeam in two steps[6]. First light is coupled into an optical waveguide and after that into the cavity. Both are achieved by evanescent coupling. Adding these structures to the nanobeam results in device outline presented in Fig. 3.2.

3.2.1. FIBER TO WAVEGUIDE COUPLING

Next to the optical device we fabricated a optical waveguide that is used as the intermediate step in transferring laser light from a standard single mode optical fiber (SMF28) to optomechanical cavity.

Detailed exploration of several options to deliver light from fiber to silicon nanobeam can be found in [8], in addition to those I will write about single sided tapered fiber cou-

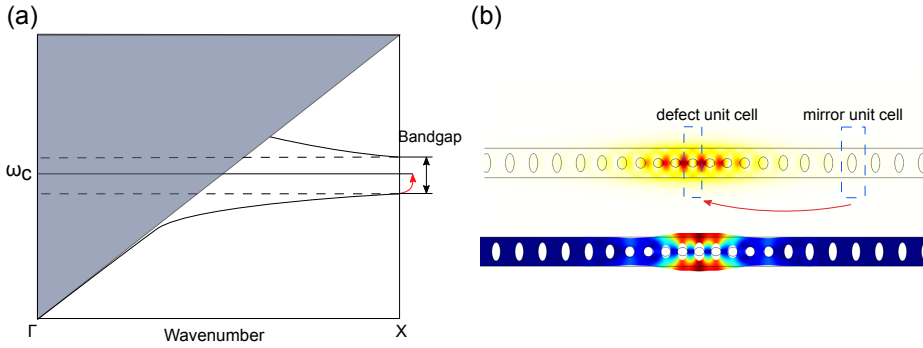


Figure 3.1: (a) Bandgap diagram of a nanobeam mirror photonic crystal. By slowly modifying the unit cell, the mirror region is transformed such that its frequency (ω_c) at X point is inside bandgap (red arrow). Shaded region presents the light cone. (b) Optical(up) and mechanical(down) mode shapes of the nanobeam. Red arrow shows the geometric transformation between the mirror and defect region.

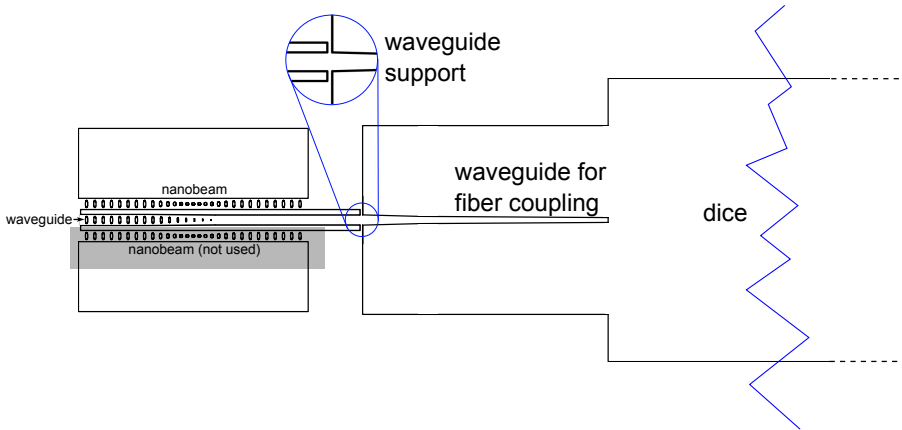


Figure 3.2: Outline of complete device-nanobeam with coupling waveguide and taper for fiber coupling. There are two nanobeams per waveguide so we fabricate more devices per chip. Overlap of optical resonances of two nanobeams is unlikely, so we can use one at the time. Waveguide support is used so waveguide does not collapse (only relevant when fabrication is taken into account).

pling. Throughout this thesis, for coupling light into the waveguide, lensed fibers were used[9]. This was mainly because it is easy to use it inside dilution fridge, it is robust, and it is commercially available (OZoptics, $2.5 \pm 0.3 \mu\text{m}$ mode diameter). Still, best transfer efficiency achieved was below 0.7, which matches with similar reports[10]. In principle, this method can provide higher efficiency, but one needs much longer tapered waveguides[11]. If we make waveguides longer than about $15 \mu\text{m}$ they tend to bend and stick to substrate layer. We wanted to improve transfer efficiency while being able to couple light into waveguide inside dilution fridge. The first approach was to use so-

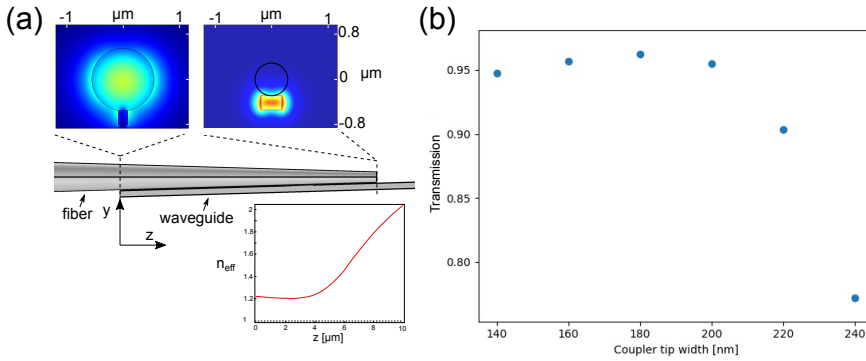


Figure 3.3: (a) Transferring laser light from tapered fiber to waveguide. At the beginning of the taper there will be a discontinuity, still high transfer efficiency is possible if one designs the system such that input fiber mode and supermode(upper-right $|E|$ mode profile) have overlap close to unity. Same goes for the discontinuity at her end of taper (upper-left $|E|$ mode profile). The plot on the bottom is effective refractive index at various points along the waveguide. (b) Simulated transfer efficiency for various widths of waveguide tip, fixed end width of 350 nm, length of 10 μm and fiber with angle 3° . This fiber angle should give negligible losses for fiber tapering itself[7], so we simulate only region where it is coupling to the waveguide.

called dimpled fibers because of their ability for transfer of light into the waveguide with efficiencies up to 0.95[6]. The problem with this technique is that it requires a microscope for alignment and fibers are very fragile. Though we had some success, after a few months we gave up on this approach and turned back to lensed fibers.

Another way to couple light from the fiber to the waveguide is using single sided tapered fiber. This is an attractive approach, because of reported efficiency of 0.96 for coupling to silicon nitride and diamond waveguides[7, 12]. Using frequency domain COMSOL simulation we show that efficiencies above 0.95 can be achieved for silicon as well (Fig. 3.3). Although these are also tapered fibers, they are much more robust than dimpled fibers and do not require a microscope for alignment inside dilution fridge. One can simply use the reflection of the side of the chip as a reference when aligning (see Appendix).

We use taper design guidelines as described in [6, 7, 12]. When fiber and waveguide are nearby ($< \lambda$) such that they couple evanescently, the system is described by supermodes. Idea is to start with supermode that looks very much like a bare fiber mode and to slowly transform the system until the supermode has high overlap with the bare waveguide mode. If the transformation is done slow enough the field will always stay in the same eigenmode of the system. The explicit adiabatic condition is[6, 7]:

$$\frac{dn_{eff}}{dz} \ll \frac{2\pi}{\lambda} \Delta n^2$$

where n_{eff} is the effective refractive index of supermode, z is the coordinate along the waveguide, λ is the free space wavelength of light and Δn is the refractive index difference of the supermode and an other nearest mode of the system. In our case, same as in reference [12] nearest modes with appropriate polarization are radiation modes with refractive index 1.

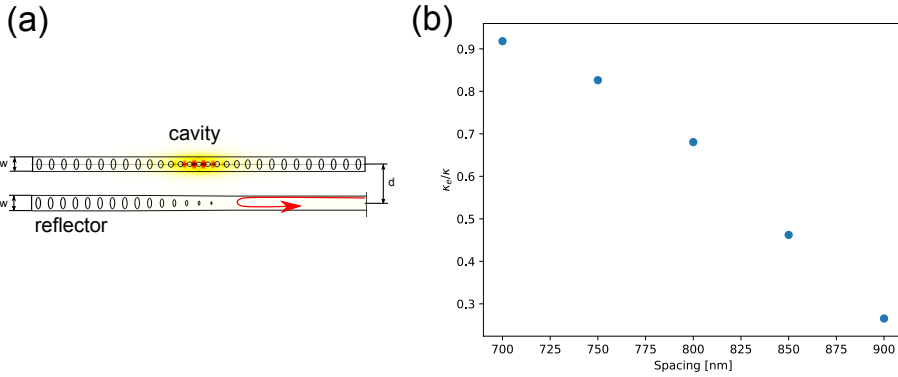


Figure 3.4: (a) Waveguide with a reflector used to couple light into the cavity. Coupling can be modified by changing the spacing between waveguide and the cavity - d . The width of the waveguide and the position of the reflector also influence coupling. (b) Simulated collection efficiency from cavity as a function of spacing between waveguide and cavity. We can see that we can change the coupling. We expect that the intrinsic quality factor of fabricated devices is fairly different from simulated, therefore this plot only serves us for qualitative purpose and rough estimation of distance

3.2.2. WAVEGUIDE TO NANOBEAM COUPLING

Once the light is inside the waveguide, we need to couple it to the optical resonator. This is also done in evanescent fashion[8]. The waveguide is placed parallel in vicinity of the cavity (Fig. 3.4(a)). Additionally there is a mirror patterned at the end of the waveguide in order to obtain single sided coupling. Other than to the waveguide, the optical mode is coupled to other loss channels. It is important to know both of these couplings in order to be able to determine parameters like fraction of photons collected by waveguide and intracavity power. Nice introduction to this problem for similar devices is given in [13] and in general [14].

The simplest way to probe the optical cavity is to record the intensity of the reflected light as a function of the detuning (Δ). The output field from optical cavity in steady state, that is driven by input field a_{in} ($|a_{in}|^2$ in units *photons/s*) is given as[13]:

$$a_{out} = a_{in} \left(1 - \frac{\kappa_e}{\frac{\kappa}{2} - i\Delta} \right), \quad (3.1)$$

where κ, κ_e are the total decay rate and decay rate into waveguide. This field can be detected on the photodiode giving a signal proportional to:

$$R = |a_{in}|^2 \left(1 - \frac{\kappa_e(\kappa - \kappa_e)}{\left(\frac{\kappa}{2}\right)^2 + \Delta^2} \right) \quad (3.2)$$

If we plot the signal as a function of detuning we can observe a Lorentzian with full width half maximum of κ . So, first we can extract total loss rate as it is equal to linewidth of recorded signal. After that we can try to extract κ_e from on resonance depth of Lorentzian:

$$D = \frac{R(\Delta = 0)}{R(\Delta \gg 0)} = \frac{\left(\frac{\kappa}{2} - \kappa_e\right)^2}{\frac{\kappa^2}{4}}$$

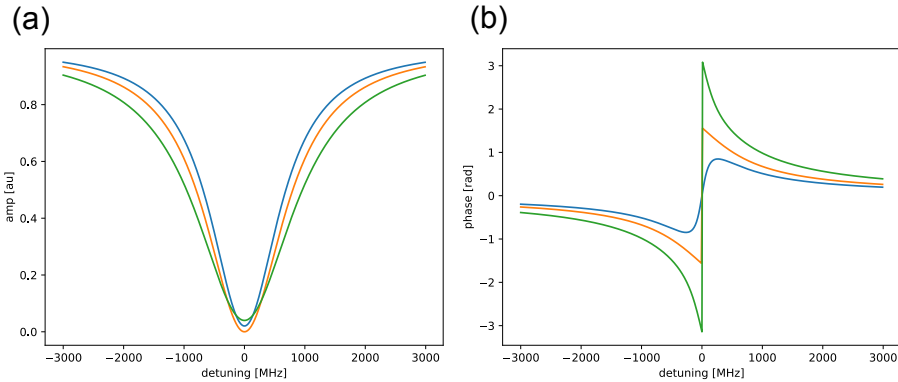


Figure 3.5: (a) Intensity response of single side coupled optical cavity. Cavity parameters are intrinsic linewidth $\kappa_0=800$ MHz and extrinsic coupling 600 MHz, 800 MHz, 1200 MHz for blue, orange, green line respectively. We can see that the over-coupled and under-coupled cavity both reflect more signal than critically-coupled one at the resonance. This prevents us from distinguishing between two. (b) Phase response of cavity, same cavity parameters and color coding.

A problem is that we can not distinguish between the over-coupled and under-coupled cavity. If we have this information we can determine κ_e from values of D and κ . This is usually done by measuring the phase response of the cavity as well (Appendix). The phase response of the cavity is plotted in Fig. 3.5(b) for various coupling regimes.

Once we have both total cavity loss and coupling constant we can determine the fraction of photons that are collected by the cavity is given by $\eta = \frac{\kappa_e}{\kappa}$, and intracavity number of photons $n_c = \left(\frac{\kappa_e}{(\frac{\kappa}{2})^2 + \Delta^2} \right) |a_{in}|^2$.

In order to vary κ_e on devices we can either change the distance between the waveguide and the cavity (Fig. 3.4) or shift the position of the waveguide mirror holes along the waveguide.

3.3. MORE THAN OPTOMECHANICS

In previous chapter we mentioned only vacuum bath as additional modes to which optomechanical system is coupled. The internal state of the silicon atoms couple to nanobeam as well, primarily through optical absorption (for a detailed description refer to [15]). Fig. 3.6 illustrates the complexity of actual nanobeam physical system. When inside silicon cavity the light will excite electrons in silicon. These will decay and emit high frequency phonons in silicon. Mechanical modes of the nanobeam will locally thermalize before thermalizing with rest of the chip. This leads to the thermal occupation of breathing mode of nanobeam that is much higher than given by the temperature of the chip. As we will see the thermal phonons will not immediately populate the mechanical state, but it usually takes 1-2 μs to achieve maximum thermal population. While many parameters of optomechanical nanobeam tend to drift with fabrication, this one tends to stay in this small range.

This heating will limit the amount of pump light we can send and therefore the con-

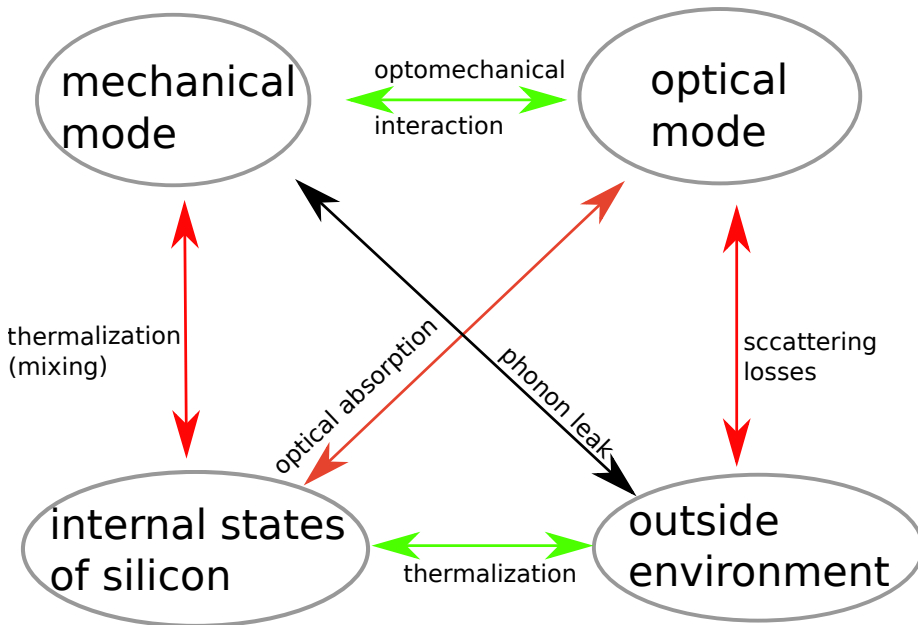


Figure 3.6: Relevant degrees of freedom of silicon OMC nanobeam. With green are labeled the interaction that one wishes to enhance and red ones that one wishes to suppress. Phonon leakage can be chosen depending of the application. By internal states we mean electronic states as well other phononic modes. Outside environment consists of infinite number of optical and mechanical resonators in ground state.

version efficiency. Also it means that we can not actively cool the device into the ground state. In addition to that whenever we send laser pulse (red or blue), we have to wait for nanobeam to thermalize to substrate if we wish to be in the ground state. I will discuss potential roads towards solving this problem in the conclusion chapter.

3.4. WHY SILICON NANOBEAMS

There are a plethora of optomechanical designs that have been investigated in detail. Our goal was to take one of these and try to observe quantum behaviour with it. We chose to perform our experiments with optomechanical crystal nanobeam devices for the following reasons

1. Ability to fabricate the devices in the sideband resolved regime, as this is one of the requirements in order to be able to select between the two mode squeezing and beamsplitter Hamiltonian.
2. High mechanical frequency enables us to have mechanical mode naturally initialized close to the ground state with negligible thermal occupation $n_{th} = [e^{\frac{\hbar\omega_m}{k_b T}} - 1]^{-1}$, when placed in dilution fridge at 20 mK. Another way of getting into the ground state is red sideband cooling, but optical absorption makes this approach practically really hard. Therefore we consider only optomechanical systems whose

mechanical frequency is in the GHz range.

3. Fairly high $g_0/\kappa \approx 10^{-3}$
4. Fabrication that is not too demanding and it is possible to fabricate a large number of devices on a single chip. This was crucial for performing two device experiments.
5. They are one of most researched on optomechanical devices, with a lot of knowledge already available
6. Integrated on the chip makes them easy to use inside dilution fridge and attractive for applications

One of the disadvantages of OMC nanobeam geometry is its bad thermal connection to the rest of the chip, which means that absorption induced thermal excitations are more likely to couple into our mechanical mode than to leak into the substrate.

OMC nanobeams can be fabricated out of almost any dielectric, with silicon, gallium arsenide, aluminium nitride, silicon nitride devices among already reported ones [16–18].

Devices described in this thesis are made out of silicon, for the following reasons

1. high refractive that enables high optomechanical coupling
2. bandgap (1.1 eV) bigger than energy of telecom photons (1550 nm→0.8 eV)
3. it is a widely used material, so fabrication is quite developed

There is usually the trade-off between bulk absorption and refractive index. Because a lot of the absorption will be from the surface of the photonic devices[19], this trade-off does not necessarily hold the same way for nanophotonic structures.

REFERENCES

- [1] J. Chan, A. H. Safavi-Naeini, J. T. Hill, S. Meenehan, and O. Painter, *Optimized optomechanical crystal cavity with acoustic radiation shield*, App. Phys. Lett. **101**, 081115 (2012).
- [2] J. Chan, *Laser cooling of an optomechanical crystal resonator to its quantum ground state of motion*, Ph.D. thesis, California Institute of Technology (2012).
- [3] Y. Akahane, T. Asano, B.-S. Song, and S. Noda, *Erratum: High- q photonic nanocavity in a two-dimensional photonic crystal*, Nature **425**, 944 (2003).
- [4] R. N. Patel, C. J. Sarabalis, W. Jiang, J. T. Hill, and A. H. Safavi-Naeini, *Engineering phonon leakage in nanomechanical resonators*, Phys. Rev. Applied **8**, 041001 (2017).
- [5] G. MacCabe, H. Ren, J. Luo, J. Cohen, H. Zhou, A. Ardizzi, and O. Painter, *Optomechanical measurements of ultra-long-lived microwave phonon modes in a phononic bandgap cavity*, (APS March Meeting, 2018).

- [6] S. Gröblacher, J. T. Hill, A. H. Safavi-Naeini, J. Chan, and O. Painter, *Highly efficient coupling from an optical fiber to a nanoscale silicon optomechanical cavity*, *Appl. Phys. Lett.*, **103**, 181104 (2013).
- [7] M. J. Burek, C. Meuwly, R. E. Evans, M. K. Bhaskar, A. Sipahigil, S. Meesala, B. Machielse, D. D. Sukachev, C. T. Nguyen, J. L. Pacheco, E. Bielejec, M. D. Lukin, and M. Lončar, *Fiber-coupled diamond quantum nanophotonic interface*, *Phys. Rev. Applied* **8**, 024026 (2017).
- [8] S. M. Meenehan, *Cavity Optomechanics at Millikelvin Temperatures*, Ph.D. thesis (2015).
- [9] S. M. Meenehan, J. D. Cohen, S. Gröblacher, J. T. Hill, A. H. Safavi-Naeini, M. Aspelmeyer, and O. Painter, *Silicon optomechanical crystal resonator at millikelvin temperatures*, *Phys. Rev. A* **90**, 011803 (2014).
- [10] J. D. Cohen, S. M. Meenehan, G. S. MacCabe, S. Gröblacher, A. H. Safavi-Naeini, F. Marsili, M. D. Shaw, and O. Painter, *Phonon counting and intensity interferometry of a nanomechanical resonator*, *Nature* **520**, 522 (2015).
- [11] V. R. Almeida, R. R. Panepucci, and M. Lipson, *Nanotaper for compact mode conversion*, *Opt. Lett.* **28**, 1302 (2003).
- [12] T. G. Tiecke, K. P. Nayak, J. D. Thompson, T. Peyronel, N. P. de Leon, V. Vuletić, and M. D. Lukin, *Efficient fiber-optical interface for nanophotonic devices*, *Optica* **2**, 70 (2015).
- [13] A. G. Krause, *Acceleration Sensing, Feedback Cooling, and Nonlinear Dynamics with Nanoscale Cavity-Optomechanical Devices*, Ph.D. thesis, California Institute of Technology (2015).
- [14] H. A. Haus, *Waves and fields in optoelectronics* (Prentice Hall, 1983).
- [15] S. M. Meenehan, J. D. Cohen, G. S. MacCabe, F. Marsili, M. D. Shaw, and O. Painter, *Pulsed Excitation Dynamics of an Optomechanical Crystal Resonator near Its Quantum Ground State of Motion*, *Phys. Rev. X* **5**, 041002 (2015).
- [16] K. C. Balram, M. Davanço, J. Y. Lim, J. D. Song, and K. Srinivasan, *Moving boundary and photoelastic coupling in GaAs optomechanical resonators*, *Optica* **1**, 414 (2014).
- [17] C. Xiong, W. H. P. Pernice, X. Sun, C. Schuck, K. Y. Fong, and H. X. Tang, *Aluminum nitride as a new material for chip-scale optomechanics and nonlinear optics*, *New Journal of Physics* **14**, 095014 (2012).
- [18] K. E. Grutter, M. Davanco, and K. Srinivasan, *Si₃N₄ nanobeam optomechanical crystals*, *IEEE Journal of Selected Topics in Quantum Electronics* **21**, 61 (2015).
- [19] H. Sekoguchi, Y. Takahashi, T. Asano, and S. Noda, *Photonic crystal nanocavity with a *q*-factor of 9 million*, *Opt. Express* **22**, 916 (2014).

4

FABRICATION OF OPTOMECHANICAL NANOBEAM DEVICES

Igor Marinković

In this chapter I will describe microfabrication steps used in this thesis to make optomechanical nanobeam devices. I will also describe a process of making single sided tapered fibers.

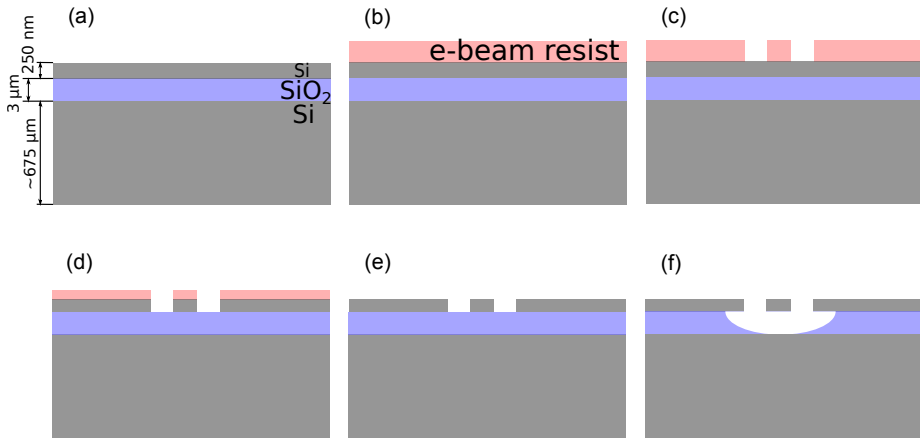


Figure 4.1: Fabrication steps of silicon nanobeams. Side view of a SOI chip (a) Starting with SOI chip (b) Spinning resist (c) Exposing resist with electron beam lithography and developing resist (d) Etching silicon layer (e) Removing resist (f) Removing oxide layer underneath device

4.1. FABRICATION OF SILICON NANOBEAM DEVICES

Once the design process of the optomechanical crystal is completed, our next task is to fabricate devices as similar to the design as possible. All devices fabricated in this thesis are made out of silicon. More precisely out of the top layer of silicon-on-insulator (SOI) wafer (boron doped, resistivity 13.5-22.5 $\Omega\text{m}\cdot\text{cm}$) from Soitec.

A summary of the fabrication steps is given in Fig. 4.1 and details for each step will be provided in the following sections. We start with SOI wafer that is diced into smaller 10x5x0.675 mm chips. These chips are made of a silicon substrate with 3 μm layer of silicon oxide above and 250 nm of crystalline silicon on top of everything. Optomechanical nanobeam devices are made out of this 250 nm top layer.

In addition to this chapter, the appendix contains several examples of fabrication trials that went wrong and how this can be prevented.

4.1.1. ELECTRON BEAM LITHOGRAPHY

We start fabrication with Electron Beam Lithography (EBL). In this step the nanobeam design will be patterned onto EBL resist. First we spin CSAR 62-09 resist on a SOI chip (Fig. 4.1(b)) using vacuum chuck spinner, that is programmed to spin for 5 seconds at 500 rpm and at 2000 rpm for 55 seconds. The chip is then baked at 150°C for 3 minutes on hot plate. This creates a layer of EBL resist (about 250 nm) on top of our chip, onto which nanobeam design will be written using an EBL machine. We expose the patterns primarily using Raith EBPG5200, though Raith EBPG5000 was also available and occasionally used. First step is making .dxf file of pattern that should be exposed. After that pattern is fractured into trapezoids and rectangles of the same dose[1]. Fracturing is done with beam step size that is about 1.5 times smaller than beam diameter (smaller than 5 nm usually). This is the distance between points that ebeam will expose. When exposing pattern for the first time, it is good to try different combinations of beam step

size and beam spot size. For each combination one should do a dose sweep in order to determine the optimal dose. In the appendix one can find example SEM images where EBL parameters were far from optimal. When choosing parameters, one should also have in mind that high resolution of exposure requires more time. Therefore sometimes it is good to separate exposure into fine and less fine patterns, and use the appropriate beams.

After the EBL write, parts of the resist that have been exposed will be removed in process called development (Fig. 4.1(c)). This is done by submerging the chip for 1 minute each, first in pentyl acetate, then 1:1 mixture of isopropanol and methyl isobutyl ketone and finally in just isopropanol.

Further improvements in the EBL step can be obtained by using a multipass technique, that minimizes the effect of noise during exposure by exposing pattern multiple times with smaller dose [2]. We noticed that this method is more reliable than simple exposure, as it averages out fast beam drifts. Few more details on multipass can be found in the appendix.

4.1.2. DRY ETCHING

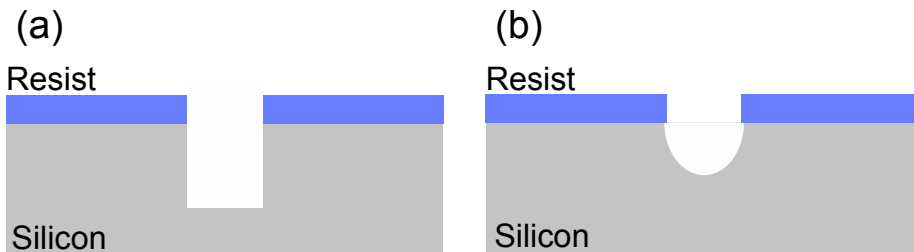


Figure 4.2: (a) Etch profile of anisotropic etching inside RIE etcher (b) Isotropic etch profile inside RIE etcher.

Areas of silicon that are not anymore covered with resist can now be etched using Inductively Coupled Plasma (ICP) Reactive Ion Etcher (RIE). Recipe for etching silicon has been developed before I joined the project, still some optimization had to be done. Introduction to ICP RIE etching can be found in [1, 3]. The basic idea is that gases used for etching are released into the vacuum chamber where the chip is. Using strong electromagnetic field plasma is created out of the gases and the ions are accelerated towards the chip. These ions can remove atoms of silicon by chemical reaction or if they have enough energy, by milling. Chemical etching tends to produce isotropic etch profile Fig. 4.2, which would make devices quite different from the design. On the other hand, milling tends to produce vertical sidewalls, but gives poor etch selectivity between silicon and resist. Some of the ions can react with silicon such that protective (passivation) layer is created. This layer has a property of not reacting with ions that are etching away silicon. Still passivation layer can be milled away. Since milling happens on surfaces facing plasma, passivation layer helps to produce vertical sidewalls.

As one can see, this is a rather complicated process with a lot of parameters that can influence the quality of the etched devices. What we desire is to fabricate devices as close as possible to the designed ones. This means a straight vertical etch with min-

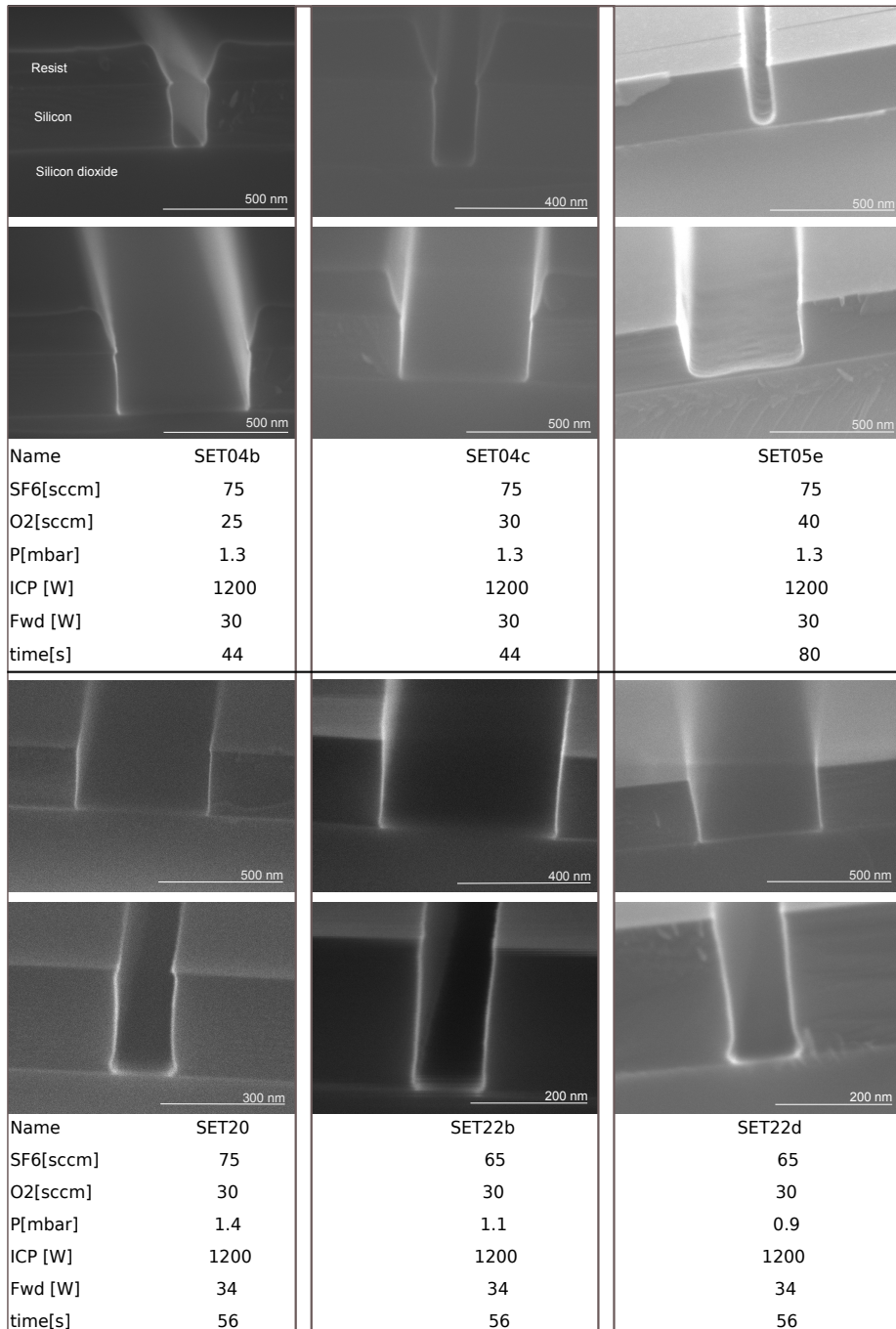


Figure 4.3: Scanning Electron Microscope (SEM) images of the etch profiles for several different etch recipes. Wide and narrow trenches of 500 nm and 100 nm are etched into silicon. After that, the chip was cleaved such that cleave intercepts the trench. Finally the side of the chip can be inspected using a SEM. On some of the SEMs, the resist had been removed. ICP[W]-power of RF source used for generating plasma. Fwd[W]-power of RF source used to accelerate ions towards the sample.

imum roughness of side walls. It is really hard to figure out what etch parameters have to be used in order to achieve this. There is some logic behind it, but also a lot of guesswork. We had to perform a lot of etch tests in search for optimal etch recipe. I show several combinations of parameters (recipes) and the result they produce in Fig. 4.3. In our fabrication process, the device pattern is transferred to the top silicon layer in ICP RIE machine Adixen AMS 100. We use a plasma of sulfur hexafluoride (SF_6) and oxygen (O_2) gases. Etching of silicon relies on ions produced by SF_6 , while both SF_6 and O_2 provide ions used for passivation (SiO_xF_y). Therefore the etch rate decreases with increase in the amount of oxygen ions in the chamber, while dependence on the amount of SF_6 is more complicated as this gas is used both for etching and passivation. The etch is performed at -120°C , as the passivation layer does not condense at higher temperatures [3]. Therefore it is important to wait several minutes in between placing the chip into the chamber and etching, so chip thermalizes to the right temperature. The electric field that accelerates ions towards the sample is switched on every 90 ms for about 10 ms only (pulsed operation). This is done so the sample can discharge any locally built up charges that may occur and that might deflect ions and that way influence the etch profile. Fig. 4.3 shows the typical sidewall profile that we obtain with this etch. Initial etch recipe Fig. 4.3-SET04b had a problem of large scalloping at top of silicon layer. Increasing amount of O_2 helps mitigate this issue to some extent-SET04b, SET05e. This also decreases etching rate. We can see that reducing the pressure in chamber by adjusting valve of turbo pump can also help with removing the scallop, yet in this case etching rate is increased-SET22b. Bottom three etches in Fig. 4.3 have been performed three years after top three etches, so cross comparison might not be ideal, since etch tends to vary over time even if all parameters are the same. If parameters suddenly change a lot, there is a chance the tool requires maintenance. One of the potential issues is leaking of helium into chamber. Helium is used for better thermal contact [1], but it leak into the chamber and influence the etch. There is a sensor measuring the pressure and flow of helium, so it is wise to monitor it. Another potential issue can be RF power reflected into the RF source. The tool automatically adjusts the impedance matching, but high reflected power can occur. This can be detrimental to the source as well the etch performance.

Silicon oxide is not etched in SF_6+O_2 plasma. It is important to stop the etch as soon as oxide layer is reached, otherwise ions will start under-etching silicon sideways resulting in profile shown in Fig. 4.3-SET22d.

Other combinations of gases can be used to anisotropically etch silicon. We had $\text{SF}_6+\text{C}_4\text{F}_8$ combination available in our etcher. This etch indeed was producing more straight sidewalls. Still we decided not to use this etch as it can leave polymer residues.

As the etch rate may drift over timescale of weeks, it is good to check the etch profile occasionally. If etch rates vary too much, it is good idea to have an additional chip in the etcher for checking etch depth at the end. So far we used the silicon carrier wafer. Problem with this is that wafer is etched and we can see surface color change over time and this might be one the reasons that etch rate is fluctuating. One can try to use carrier wafer that has silicon oxide layer on top. Another improvement might be reducing the etch rate by reducing SF_6 or increasing O_2 . Reducing SF_6 is not advisable with our etcher as flow controller is not stable at low flows. After etching we dice the chip around $10\ \mu\text{m}$ away from devices in order to be able to approach device with optical fiber (Fig. 4.4)

when we want to perform measurements.

4.1.3. WET PROCESSING

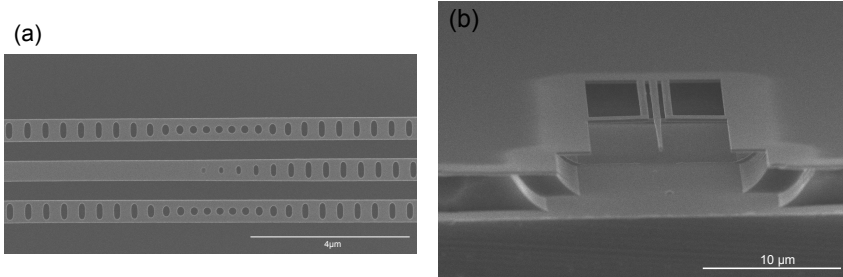


Figure 4.4: (a) Scanning electron microscope (SEM) top view image of nanobeam device at the end of fabrication process. (b) Side view on chip with fully fabricated waveguide and two nanobeams.

After the chip is diced, the resist layer is removed by leaving it in *N,N*-Dimethylformamide for 5 minutes at 70 °C. In order to remove contamination from the chip, that might have occurred during the fabrication, we perform standard RCA cleaning[4]. This step is good at removing the most organic contaminants as well as some metallic contaminants. Another option would be using Piranha solution for cleaning. RCA cleaning is well known silicon process that consist of two steps[5]

1. RCA1: mixture of 5 parts of deionized water, 1 part of 28% ammonia water is heated to 75 °C. 1 part of hydrogen peroxide is added and finally holder with chip is placed inside for 10 minutes.
2. RCA2: mixture of 6 parts of deionized water, 1 part of aqueous 37% HCl is heated to 75 °C. 1 part of hydrogen peroxide is added and finally holder with chip is placed inside for 10 minutes.

Finally the oxide under the device is removed by keeping it in 40% Hydrofluoric acid (HF) at room temperature for 3 minutes and 30 seconds. 40% HF isotropically etches oxide with about one micrometer per minute while the silicon etch rate is negligible. Optionally additional RCA cleaning and 10 second dip in 1% HF can be performed in order to clean and smooth down the surface. Once we take the chip out of HF, its surface should be passivated with hydrogen atoms. RCA oxidises the silicon surface, while HF strips the grown oxide, therefore each RCA+HF step tends to shift the optical resonance (by about 15 nm to lower wavelength).

At this point the devices are finished and a first quick thing to check is the optical resonance. If the resonance is not at the wavelength desired or their linewidth is too large, it is necessary to inspect the structure with SEM. Sizes of the features can be measured and if they are far from designed, this can be compensated for in next generation of chips. Optical quality factor strongly depends on the fabrication imperfections. Typical optical intrinsic quality factor of a fabricated device is about $4 \cdot 10^5$, while simulated value is above 10^7 [6]. Mechanical quality factor is also sensitive on fabrication imperfections, but as we will see in later chapters we intentionally wanted low mechanical quality

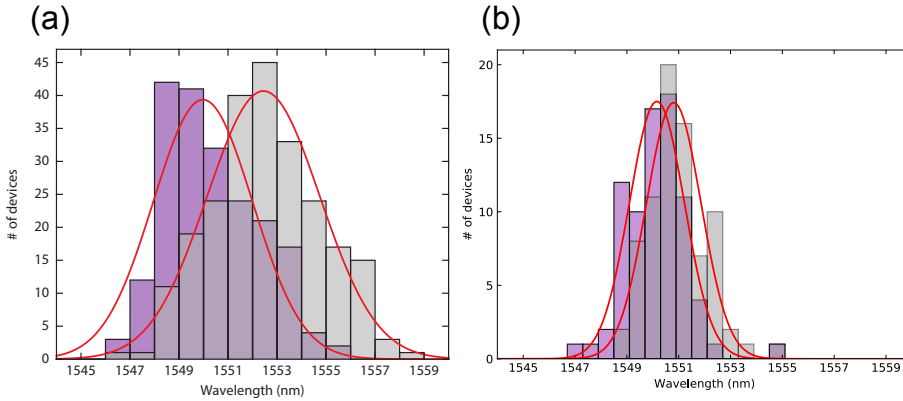


Figure 4.5: Distribution of optical resonances for: (a) Devices fabricated on two chips with proximity error correction and devices were exposed in blocks of 8 (devices separated $30\ \mu\text{m}$ inside same blocks, blocks separated by $100\ \mu\text{m}$). Standard deviation is about 2 nm. Figure taken from [7]. (b) Devices fabricated on single chip without proximity error correction with single block of few hundred devices each separated $30\ \mu\text{m}$. Standard deviation is about 1 nm.

factors so devices thermalize faster to the base temperature. Images of a fully processed device can be seen in Fig. 4.4.

4.2. FABRICATING IDENTICAL DEVICES

As it will be seen in the later chapters, for some applications it is crucial to be able to fabricate devices with nearly identical optical and mechanical resonances. In this section I would like to give few hints that can help in achieving that. Initially we always fabricated two chips and looked for a matching pair. Statistical distribution of resonances is given in Fig. 4.5. Main approach here was to simply fabricate large number of devices on the chip and select ones with similar properties. After this experiment it was realized that a better overlap can be achieved by fabricating only one chip and cleaving it into two pieces. Devices for an experiment can be then chosen from each of these two pieces. This enables chips that have center of resonance distribution closer to each other. When writing devices with EBL it is important to have same dose on all devices in order to have most identical devices. We initially arranged devices in block of eight devices and performed proximity error correction (PEC). About $30\ \mu\text{m}$ away we would place next identical block and so on. It turned out this is not the best solution and half the resonance spread can be achieved by simply not using PEC and writing one large block. Of course devices at the edge will have their resonance off, but in previous case devices at the edge of each block is affected.

4.3. FABRICATING TAPERED FIBERS

As described in the previous chapter, tapered fibers can be used to efficiently transfer the light from fiber to a waveguide fabricated on a chip. We fabricate these tapered fibers from regular $125\ \mu\text{m}$ fibers (SMF28) by etching them in hydrofluoric (HF) acid[8]. Before

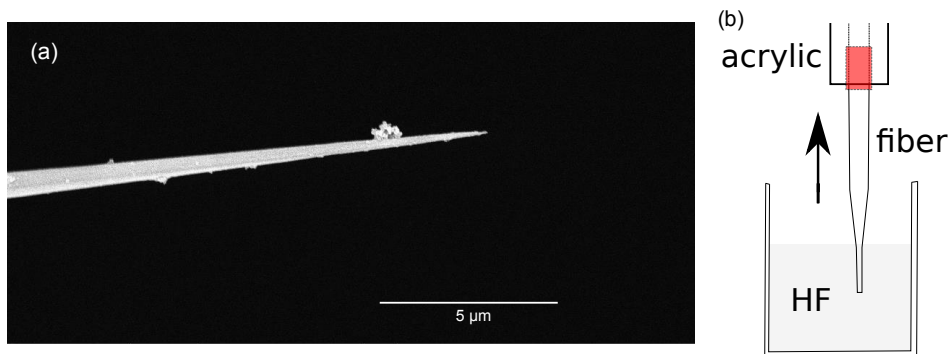


Figure 4.6: (a) SEM image of HF fiber. Fiber is coated with gold in order to obtain SEM image. Unfortunately, dust particles polluted the fiber during gold evaporation (Image credit Andreas Wallucks). (b) Pulling fiber out of HF. Transition between coated and striped fiber (red) showed structural weakness-tends to break.

etching, the acrylic buffer is stripped at the end of the fiber. In order to obtain conical shape we slowly pull fiber out of 40% HF for about 70 minutes with $0.4 \mu\text{m/s}$ using Thorlabs MTS25-Z8. During the pulling HF evaporates and condenses on the fiber. This can lead to roughness as well structural weakness (Fig. 4.6). A film of o-Xylene can be added on top such that meniscus is formed, that shrinks as the fiber gets thinner and that way provide a gradual etch even without pulling. This layer also probably helps with reducing HF evaporation. Etching of fibers under acrylic can also be partially mitigated by using fiber ferrules as protection for fibers during the pulling. Alternatively one can produce similar fibers by heating it with hydrogen flame and then pulling[9].

REFERENCES

- [1] J. T. Hill, *Nonlinear Optics and Wavelength Translation Via Cavity-Optomechanics*, Ph.D. thesis, California Institute of Technology (2013).
- [2] X. Ji, F. A. S. Barbosa, S. P. Roberts, A. Dutt, J. Cardenas, Y. Okawachi, A. Bryant, A. L. Gaeta, and M. Lipson, *Ultra-low-loss on-chip resonators with sub-milliwatt parametric oscillation threshold*, *Optica* **4**, 619 (2017).
- [3] M. D. Henry, *ICP ETCHING OF SILICON*, Ph.D. thesis, California Institute of Technology (2010).
- [4] D. K. Sparacin, S. J. Spector, and L. C. Kimerling, *Silicon waveguide sidewall smoothing by wet chemical oxidation*, *J. Lightwave Technol.* **23**, 2455 (2005).
- [5] W. Kern, *The evolution of silicon wafer cleaning technology*, *Journal of The Electrochemical Society* **137**, 1887 (1990).
- [6] J. Chan, A. H. Safavi-Naeini, J. T. Hill, S. Meenehan, and O. Painter, *Optimized optomechanical crystal cavity with acoustic radiation shield*, *App. Phys. Lett.* **101**, 081115 (2012).

- [7] R. Riedinger, A. Wallucks, I. Marinković, C. Löschnauer, M. Aspelmeyer, S. Hong, and S. Gröblacher, *Remote quantum entanglement between two micromechanical oscillators*, *Nature* **556**, 473 (2018).
- [8] M. J. Burek, C. Meuwly, R. E. Evans, M. K. Bhaskar, A. Sipahigil, S. Meesala, B. Machielse, D. D. Sukachev, C. T. Nguyen, J. L. Pacheco, E. Bielejec, M. D. Lukin, and M. Lončar, *Fiber-coupled diamond quantum nanophotonic interface*, *Phys. Rev. Applied* **8**, 024026 (2017).
- [9] T. G. Tiecke, K. P. Nayak, J. D. Thompson, T. Peyronel, N. P. de Leon, V. Vuletić, and M. D. Lukin, *Efficient fiber-optical interface for nanophotonic devices*, *Optica* **2**, 70 (2015).

5

HANBURY BROWN AND TWISS INTERFEROMETRY OF SINGLE PHONONS FROM AN OPTOMECHANICAL RESONATOR

Sungkun Hong^{*}, Ralf Riedinger^{*}, Igor Marinković^{*}, Andreas Wallucks^{*}, Markus Aspelmeyer, Simon Gröblacher

Nano- and micromechanical devices have become a focus of attention as new solid-state quantum devices. Reliably generating non-classical states of their motion is of interest both for addressing fundamental questions about macroscopic quantum phenomena as well as for developing quantum technologies in the domains of sensing and transduction. We use quantum optical control techniques to conditionally generate single-phonon Fock states of a nanomechanical resonator. We perform a Hanbury Brown and Twiss type experiment that verifies the non-classical nature of the phonon state without requiring full state reconstruction. Our result establishes purely optical quantum control of a mechanical oscillator at the single phonon level.

^{*} equal contribution

This chapter has been published in Science **358**, 203 – 206 (2017)

5.1. MAIN TEXT

Intensity correlations in electromagnetic fields have been pivotal in the development of modern quantum optics. The experiments by Hanbury Brown and Twiss were a particular milestone that connected the temporal and spatial coherence properties of a light source with the second-order intensity autocorrelation function $g^{(2)}(\tau, x)$ [1–3]. In essence, $g^{(2)}$ correlates intensities measured at times differing by τ or at locations differing by x and is hence a measure for their joint detection probability. At the same time, these correlations allow the quantum nature of the underlying field to be inferred directly. For example, a classical light source of finite coherence time can only exhibit positive correlations at $\tau \approx 0$ delay in the joint intensity detection probability, leading to bunching in the photon arrival time. This result is true for all bosonic fields. Fermions, on the other hand, exhibit negative correlations and hence anti-bunching in the detection events [4–6], which is a manifestation of the Pauli exclusion principle. A bosonic system needs to be in a genuine non-classical state to exhibit anti-bunching. The canonical example is a single photon (Fock) state, for which $g^{(2)}(\tau = 0) = 0$ because no joint detection can take place [7]. For this reason, measuring $g^{(2)}$ has become a standard method to characterize the purity of single-photon sources [8]. In general, $g^{(2)}(\tau)$ carries a wealth of information on the statistical properties of a bosonic field with no classical analogue [9, 10], specifically sub-Poissonian counting statistics ($g^{(2)}(0) < 1$) and anti-bunching ($g^{(2)}(\tau) \geq g^{(2)}(0)$), all of which have been demonstrated successfully with quantum states of light [11, 12].

Over the past decade, motional degrees of freedom, i.e. phonons, of solid-state devices have emerged as a novel quantum resource. Quantum control of phonons was pioneered in the field of trapped ions [13], where single excitations of the motion of the ions are manipulated through laser light. These single phonon states have been used for fundamental studies of decoherence [14] as well as for elementary transduction channels in quantum gates for universal quantum computing [15]. Cavity optomechanics [16] has successfully extended these ideas to optically controlling the collective motion of solid-state mechanical systems. It has allowed for remarkable progress in controlling solid-state phonons at the quantum level, including sideband cooling into the quantum ground state of motion [17, 18], the generation of quantum correlated states between radiation fields and mechanical motion [19–21] and the generation of squeezed motional states [22–24].

So far single phonon manipulation of micromechanical systems has exclusively been achieved via coupling to superconducting qubits [25–27], while optical control was limited to the generation of quantum states of bipartite systems [20, 21, 28]. Here we demonstrate all-optical quantum control of a purely mechanical system, creating phonons at the single quantum level and unambiguously showing their non-classical nature. We combine optomechanical control of motion and single phonon counting techniques [21, 29] to probabilistically generate a single phonon Fock state from a nanomechanical device. Implementing Hanbury Brown and Twiss interferometry for phonons [21, 29] (Figure 5.1), allows us to probe the quantum mechanical character of single phonons without reconstructing their states. We observe $g^{(2)}(0) < 1$, which is a direct verification of the non-classicality of the optomechanically generated phonons, highlighting their particle-like behavior.

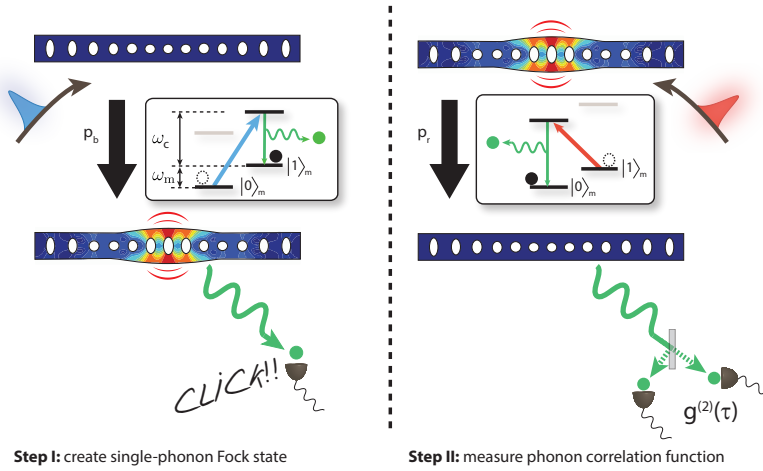


Figure 5.1: Working principle of the scheme used to generate single-phonon states and to verify their non-classicality. The first step (left) starts with a mechanical oscillator in its quantum ground state, followed by pumping the optomechanical cavity with a blue-detuned pulse. The resonator is excited to a single-phonon state with a probability $p_b = 1.2\%$ through the optomechanical interaction, which is accompanied with the emission of a photon on resonance with the cavity. The detection of such a photon in a single-photon detector allows us to post-select on a purely mechanical Fock state. In order to verify the quantum state we created, a red-detuned read pulse is sent onto the optomechanical cavity in the second step (right), which performs a partial state transfer between the optics and the mechanics. With a probability of $p_r = 32.5\%$ the mechanical system's excitation is converted into a photon on cavity resonance, returning the mechanics to its ground state. The photon is sent onto a beamsplitter, where we measure the second order intensity correlation function $g^{(2)}$ using a pair of single-photon detectors. $g^{(2)}(0) < 1$ confirms the non-classicality of the generated phonon states. The insets show the equivalent energy level diagrams of the processes.

Our optomechanical crystal [18] consists of a micro-fabricated silicon nanobeam patterned in a way that it simultaneously acts as a photonic and phononic resonator (Figure 5.2). The resulting optical and mechanical modes couple through radiation pressure and the photoelastic effect such that a displacement equivalent to the zero-point fluctuation of the mechanical mode leads to a frequency shift of the optical mode by $g_0/2\pi = 869$ kHz (g_0 : optomechanical coupling rate). The optical resonance has a wavelength of $\lambda = 1554.35$ nm and a critically coupled total quality factor of $Q_o = 2.28 \times 10^5$ (i.e. cavity energy decay rate $\kappa/2\pi = 846$ MHz), while the mechanical resonance has a frequency of $\omega_m/2\pi = 5.25$ GHz and a quality factor of $Q_m = 3.8 \times 10^5$. The device is placed in a dilution refrigerator with a base temperature of $T = 35$ mK. When the device is thermalized, its high frequency guarantees that the mechanical mode is initialized deep in its quantum ground state [21].

We utilize two types of linearized optomechanical interactions: the parametric down-conversion and the state-swap, which can be realized by driving the system with detuned laser beams in the limit of weak coupling ($g_0\sqrt{n_c} \ll \kappa$; n_c : intracavity photon number) and resolved sidebands ($\kappa \ll \omega_m$) [16]. The parametric down-conversion interaction has the form $H_{dc} = \hbar g_0\sqrt{n_c}(\hat{a}^\dagger \hat{b}^\dagger + \hat{a} \hat{b})$ where \hbar is the reduced Planck con-

stant and \hat{b}^\dagger (\hat{b}) the phononic creation- (annihilation-) operator, while \hat{a}^\dagger (\hat{a}) are the respective photonic operators. This interaction is selectively turned on by detuning the laser frequency ω_L to the blue side of the cavity resonance ω_c ($\omega_L = \omega_c + \omega_m$). H_{dc} drives the joint optical and mechanical state, initially in the ground state, into the state $|\psi\rangle_{om} \propto |00\rangle + p_b^{1/2}|11\rangle + p_b|22\rangle + O(p_b^{3/2})$. For low excitation probabilities $p_b \ll 1$, higher order terms can be neglected such that the system can be approximated as emitting a pair of resonant signal photon and idler phonon with a probability p_b [30]. Detection of the signal photon emanating from the device heralds a single excitation of the mechanical oscillator $|\psi\rangle_m \approx |1\rangle$, in close analogy to heralded single photons from spontaneous parametric down-conversion. To read out the phonon state, we send in another laser pulse that is now red-detuned from the cavity resonance by ω_m ($\omega_L = \omega_c - \omega_m$). This realizes a state-swap interaction $H_{swap} = \hbar g_0 \sqrt{n_c} (\hat{a}^\dagger \hat{b} + \hat{a} \hat{b}^\dagger)$ which transfers the mechanical state to the optical mode with efficiency p_r . We can therefore use the scattered light field from this “read” operation to directly measure the second-order intensity correlation function $g^{(2)}$ of the mechanical oscillator mode, which is defined as

$$g^{(2)}(\tau) = \langle \hat{b}^\dagger(0) \hat{b}^\dagger(\tau) \hat{b}(\tau) \hat{b}(0) \rangle / \langle \hat{b}^\dagger(0) \hat{b}(0) \rangle \langle \hat{b}^\dagger(\tau) \hat{b}(\tau) \rangle, \quad (5.1)$$

where τ is the time between the first and the second detection event. Just like for any other bosonic systems, $g^{(2)}(0) > 1$ means that the phonons exhibit super-Poissonian (classical) behavior, while $g^{(2)}(0) < 1$ is direct evidence of the quantum mechanical nature of the state and implies sub-Poissonian phonon statistics [10].

We implement the experimental scheme (Fig. 5.1) by repeatedly sending a pair of optical pulses, the first one blue-detuned (pump pulse, full width at half maximum, FWHM ≈ 32 ns) and a subsequent one red-detuned (read pulse, FWHM ≈ 32 ns) with a fixed repetition period, $T_r = 50 \mu\text{s}$. Photons generated through the optomechanical interactions are reflected back from the device, and are analyzed by a Hanbury Brown and Twiss interferometer using two superconducting nanowire single-photon detectors (SNSPD). We set the mean pump pulse energy to 27 fJ such that $p_b = 1.2\%$ [31]. Detection of resonant (signal) photons created by this pulse heralds the preparation of the mechanical oscillator in a single phonon Fock state, in principle with a probability of 98.8%. Due to a small amount of initial thermal phonons and residual absorption heating, a fraction of unwanted phonons are incoherently added to the quantum states we prepare [21]. Following each pump pulse, a red-detuned read pulse is sent to the device with a programmable delay t_d , reading out phonons stored in the device by converting them into photons on resonance with the cavity. The mean read pulse energy is set to 924 fJ, corresponding to a state-swap efficiency $p_r \approx 32.5\%$. Taking into account subsequent optical scattering losses, this yields an absolute quantum efficiency for the detection of phonons of 0.9% [31]. Finally, the pulse repetition period of $T_r = 50 \mu\text{s}$, which is long compared to the mechanical damping time of 11 μs , provides ample time for dissipating any excitation or unwanted heating generated by optical absorption. This ensures that each experimental cycle starts with the mechanical mode well in the quantum ground state. The pulse sequence is repeated more than 7×10^9 times in order to acquire enough statistics. Conditioned on heralding events from detectors $D1$ by the blue-detuned pulses, we analyze the coincidence detection probability of photons at $D1$ and $D2$, that are transferred from phonons by the swap operation.

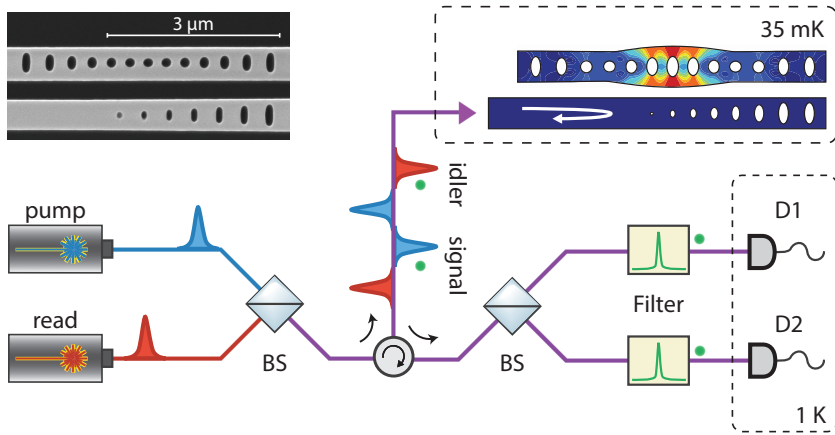


Figure 5.2: Sketch of the experimental setup used to measure the intensity autocorrelation function $g^{(2)}$ of phonons. Blue-detuned pump pulses are sent into the optomechanical cavity which is kept at 35 mK. With a small probability p_b the optomechanical interaction creates a single excitation of the mechanical mode at 5.25 GHz (idler) and at the same time emit a signal photon on resonance with the cavity. The original optical pump field is then filtered and only the signal photon created in the optomechanical down-conversion process is detected in one of the single-photon detectors $D1$ or $D2$. With a time delay of t_d a red-detuned read pulse is sent into the device, converting any mechanical idler excitation into an idler photon, which again is filtered from the original pump. Conditioned on the detection of a signal photon, we measure the $g^{(2)}$ of the idler photons. As the red-detuned pulse is equivalent to a state-swap interaction (see text), the $g^{(2)}$ function we obtain for the photons is a direct measure of the $g^{(2)}$ function of the phonons in the mechanical oscillator. The inset in the top left corner shows a scanning electron microscope image of the device (top) next to a waveguide (bottom).

In our first experiment, we set $t_d = 115$ ns and measure $g^{(2)}(0)$ of the heralded phonons. We note that one of our SNSPDs, $D2$, exhibits a longer dead time than t_d [31] and we therefore only use photon counts from $D1$ for heralding the phonon states. From these measurements we obtain a $g^{(2)}(0)$ of $0.65^{+0.11}_{-0.08}$ (Figure 5.3c), demonstrating a non-classical character of the mechanical state.

The observed $g^{(2)}(0)$ of 0.65 is considerably higher than what we expect in the ideal case $g_{ideal}^{(2)}(0) \approx 4 \times p_b = 0.045$ [31]. We attribute this to heating induced by the absorption of the pump and read pulses. While a detailed physical mechanism of the absorption and subsequent heat transfer into the mechanical mode is still a subject of current studies [21], the influx of thermal phonons \dot{n}_{abs} caused by the absorption of drive laser pulses can be experimentally deduced from the (unconditional) photon count rates generated by the read pulses [31]. Including an estimation of the initial thermal phonon number n_{init} , which is likewise inferred from the unconditional photon counts associated with the pump and read pulses, we construct a theoretical model that predicts $g^{(2)}(0)$ as a function of p_b , n_{init} , and \dot{n}_{abs} . Given the measured $n_{init} \approx 0.20$ and n_{abs} [31] within the read pulse, our model predicts $g^{(2)}(0) \approx 0.76$, which is consistent with the experimental value.

To further probe the effect of thermal phonons, we perform a set of experiments with reduced repetition periods T_r , while keeping the other settings for the pump pulses the

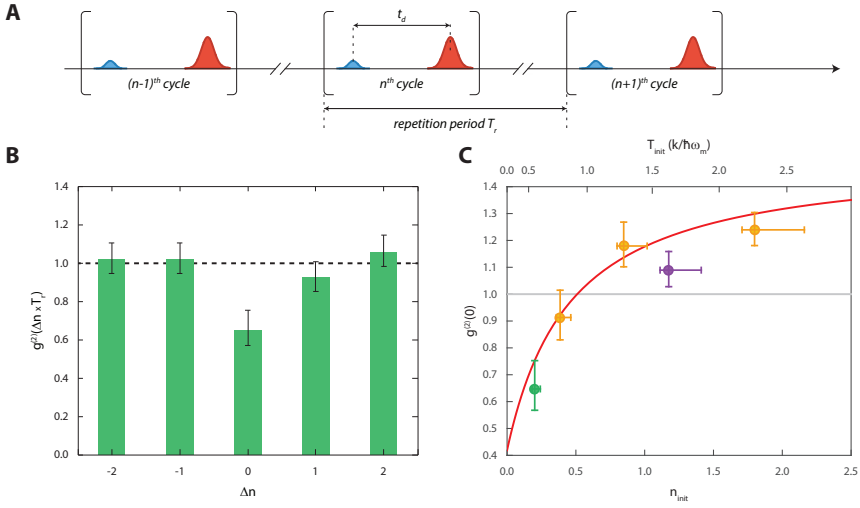


Figure 5.3: (a) Pulse sequence used in the experiments. Each cycle consists of a blue-detuned pump pulse and a subsequent red-detuned read pulse delayed by t_d . The pulse sequence is repeated with the cycle of T_r . Both t_d and T_r can be adjusted. (b) The measurement result of the second-order correlation function $g^{(2)}(\tau = \Delta n \times T_r)$ of the heralded phonons, with $g^{(2)}(0) < 1$ being a direct measure of their non-classicality. In this measurement, we set $t_d = 115$ ns and $T_r = 50$ μ s. $g^{(2)}(\Delta n \times T_r)$ with $\Delta n \neq 0$ depicts the correlations between phonons read from separate pulse sequences with the cycle difference of Δn . While phonons from independent pulses show no correlation $g^{(2)}(\Delta n \times T_r; \Delta n \neq 0) \approx 1$, those from the same read pulse are strongly anti-correlated with a $g^{(2)}(\tau = 0) = 0.65^{+0.11}_{-0.08}$. (c) The influence of an incoherent phonon background on the $g^{(2)}(0)$ of the generated mechanical states. We plot several measurements for a range of different effective initial temperatures of the nanomechanical oscillator. The first data point (green) is taken with a delay $t_d = 115$ ns and a repetition period $T_r = 50$ μ s. We control the initial mode occupation n_{init} utilizing the long lifetime of the thermally excited phonons stemming from the delayed absorption heating by pump and read pulses. This allows to increase n_{init} while keeping the bulk temperature and properties of the device constant, causing an increase of $g^{(2)}(0)$, as the state becomes more thermal. The red line shows the simulated $g^{(2)}(0)$ as discussed in [31]. For technical reasons all data points (yellow, purple) except the leftmost (green) were taken with $t_d = 95$ ns. In addition, the second from the right (purple) was taken at an elevated bath temperature of $T_{bath} = 160$ mK.

same. This effectively increases n_{init} , because the absorbed heat does not have enough time to dissipate before the next pair of pulses arrives. As expected, as T_r is reduced, we observe an increase in $g^{(2)}(0)$. With the measured n_{init} and \dot{n}_{abs} from the same data set, we can plot the predicted $g^{(2)}(0)$ values. As is shown in Figure 5.3, the experimental values and theoretical bounds on $g^{(2)}(0)$ are in good agreement.

We also measure $g^{(2)}(0)$ for $t_d = 350$ ns, and find that it is increased to $0.84^{+0.07}_{-0.06}$. This increase is consistent with previously observed delayed heating effects of the absorption [21] and is in good agreement with the theoretical prediction of 0.84. Even for these longer delays, the value is still distinctively below 1, demonstrating the potential of our device as a single phonon quantum memory on the time scale of several hundred nanoseconds.

We have experimentally demonstrated the quantum nature of heralded single phonons in a nanomechanical oscillator by measuring their intensity correlation function $g^{(2)}(0) < 1$. The deviation from a perfect single-phonon state can be modeled by a finite initial

thermal occupation and additional heating from our optical cavity fields. We achieve conversion efficiencies between phonons and telecom photons of more than 30%, only limited by our available laser power and residual absorption. Full state reconstruction of the single phonon state, as demonstrated with phononic states of trapped ions [14], should be realizable with slightly improved read-out efficiency and through homodyne tomography. The demonstrated fully optical quantum control of a nanomechanical mode, preparing sub-Poissonian phonons, shows that optomechanical cavities are a useful resource for future integrated quantum phononic devices, both as single phonon sources and detectors. They are also an ideal candidate for storage of quantum information in mechanical excitations and constitute a fundamental building block for quantum information processing involving phonons. Some of the potential applications include quantum-noise limited, coherent microwave to optics conversion, as well as studying the quantum behavior of individual phonons of a massive system.

ACKNOWLEDGMENTS

We thank V. Anant, J. Hofer, C. Loeschner, R. Patel, and A. Safavi-Naeini for experimental support and K. Hammerer for helpful discussions. We acknowledge assistance from the Kavli Nanolab Delft, in particular from M. Zuiddam and C. de Boer. This project was supported by the European Commission (OMT), Foundation for Fundamental Research on Matter (FOM) Projectruimte grants (15PR3210, 16PR1054), the Vienna Science and Technology Fund WWTF (ICT12-049), the European Research Council (ERC CoG QLev4G, ERC StG Strong-Q), the Austrian Science Fund (FWF) under projects F40 (SFB FOQUS) and P28172, and by the Netherlands Organisation for Scientific Research (NWO/OCW), as part of the Frontiers of Nanoscience program, as well as a Vidi grant (016.159.369). R.R. is supported by the FWF under project W1210 (CoQuS) and is a recipient of a DOC fellowship of the Austrian Academy of Sciences at the University of Vienna. All relevant data to understand and assess the conclusions of this research are available in the main text and supplementary materials.

5.2. MATERIALS AND METHODS

OPTOMECHANICAL DEVICES

The optomechanical device is fabricated from a silicon on insulator wafer (Soitec) with a device layer of 250 nm thickness on top of a 3 μm buried oxide layer. We pattern our chips with an electron beam writer and transfer the structures into the silicon layer in a reactive ion etcher using a SF_6/O_2 plasma. One of the sides of the chip is removed to allow for in-plane access to the lensed fiber couplers. After the resist is removed, the device layer is undercut in 40% hydrofluoric acid. An additional cleaning step using the so-called RCA method [32] is performed to remove organic and metallic residuals. The final step is a dip in 2% hydrofluoric acid to remove the oxide layer formed by the RCA cleaning and to terminate the silicon surface with hydrogen atoms.

Unlike in previous device designs [33], we do not use an additional phononic shield around the optomechanical structure as this unnecessarily increases the re-thermalization time and therefore reduces the achievable repetition rate of our experiment [21]. We reduce the mechanical quality factors of the designed structures further by offsetting the

photonic crystal holes laterally from the center of the beam by 30 nm [34]. This yields a measured quality factor of $Q_m = 3.8 \times 10^5$ at mK temperatures, while otherwise such structures exhibit Q's beyond 10^7 .

In order to find particularly good devices on a chip, we characterize them in a pump-probe experiment at cryogenic temperatures (35mK) and select devices with optimal mechanical Q and low optical absorption. We then perform cross-correlation measurements of the photon-phonon pairs scattered by the pump pulse, while varying the repetition period T_r , pump excitation probability p_b and state-swap efficiency p_r . This short two-fold coincidence measurement (~ 1 h) allows us to predict the expectation value of the three-fold coincidence autocorrelation measurement [21, 35, 36] as well as the time required to obtain enough statistics for a targeted confidence interval. We chose a parameter set, which allows for a statistically significant (p-value < 0.001 , see below) demonstration of intensity anti-correlations ($g^{(2)}(0) < 1$) of the phononic state within a realistic measurement time (~ 100 h).

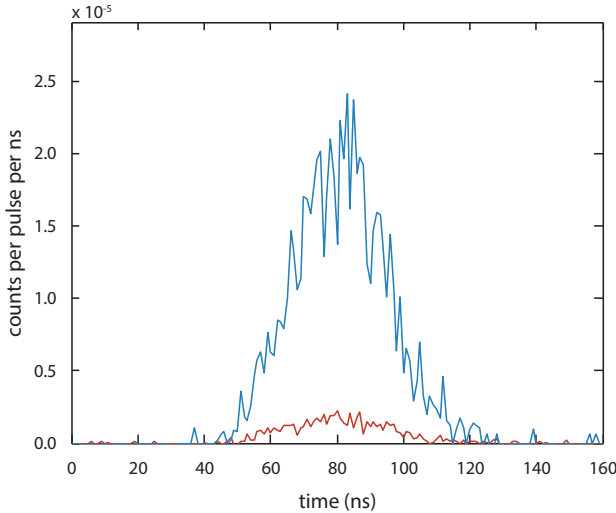


Figure 5.4: A sideband asymmetry measurement is performed to extract the optomechanical coupling rate g_0 . For a detailed explanation of the measurement see the text below. We plot the detected photon counts per pulse repetition per nanosecond for a blue-detuned (blue) and a red-detuned beam (red). Unwanted contributions from leaked pump photons and detector dark counts are independently measured and subtracted. Integrating over the whole detection window (i.e. from 30 to 150 ns in the plot) gives the photon counting probabilities C_b and C_r , respectively. From this data, we extract the optomechanical coupling rate $g_0/2\pi = 869$ kHz.

DETECTION EFFICIENCY

We calibrate the total detection efficiencies of optomechanically generated cavity photons ($\eta_i; i = 1, 2$) by performing a series of independent measurements. First, the fiber-to-device coupling efficiency ($\eta_{fc} = 0.48$) is measured by sending light with known power to the photonic crystal and then measuring the reflected power. The extraction efficiency of cavity photons η_{dev} is obtained from the device impedance ratio, $\eta_{dev} = \kappa_e/\kappa$, where

κ_e is the external cavity energy decay rate. These values are extracted from the visibility and the linewidth of the optical resonance scan, and we find $\eta_{dev} = 0.5$. Furthermore, we measure the efficiency of detecting photons coming from the device for each SNSPD. We launch weak, off-resonant optical pulses with an average of 5.14 photons to the device and measure the photon count rate of each SNSPD. This measurement gives the quantities $\eta_{fc}^2 \times \eta_{trans,i} \times \eta_{QE,i}$, where $\eta_{trans,i}$ is the transmission efficiency of the detection path to each SNSPD, while $\eta_{QE,i}$ is their quantum efficiency. As η_{fc} is measured independently, $\eta_{trans,i} \times \eta_{QE,i}$ can be calculated from these results. Finally, this allows us to obtain $\eta_i = \eta_{dev} \times \eta_{fc} \times \eta_{trans,i} \times \eta_{QE,i}$, which are $\eta_1 = 1.16\%$ and $\eta_2 = 1.50\%$, respectively.

OPTOMECHANICAL COUPLING RATE

In order to calibrate the optomechanical coupling rate g_0 between the cavity field and the mechanical mode, we perform a measurement similar to sideband thermometry [21, 37] (see Figure 5.4). In this measurement, pairs of pump and probe pulses are sent to the device with a repetition period of $T_r = 100 \mu\text{s}$. For this pulse sequence, a blue-detuned pump pulse (190.62 fJ) is sent to intentionally heat the device's mechanical mode, followed by the probe pulse (55.16 fJ) with a long delay of 99.825 μs . We perform two sets of such repetitive measurements, one with red-detuned and the other with blue-detuned probe pulses. From each measurement, we acquire a photon counting probability for the probe pulses, C_r (red-detuned) and C_b (blue-detuned). These can be expressed as $C_r = (\eta_1 + \eta_2) \times p_r \times n_{th}$ and $C_b = (\eta_1 + \eta_2) \times p_b \times (1 + n_{th})$ in the limit of $p_b \ll 1$ and $p_r \ll 1$, where p_b and p_r are equivalent to the photon-phonon pair excitation probability and state-swap efficiency as introduced in the main text. p_b and p_r can be explicitly written as

$$p_b = \exp(\kappa_e/\kappa [4g_0^2 E_p/\hbar\omega_c(\omega_m^2 + (\kappa/2)^2)]) - 1, \quad (5.2)$$

$$p_r = 1 - \exp(-\kappa_e/\kappa [4g_0^2 E_p/\hbar\omega_c(\omega_m^2 + (\kappa/2)^2)]), \quad (5.3)$$

where E_p is the total energy of the incident laser pulses and all the other terms as defined in the main text. We find that $C_r = 0.0064\%$ and $C_b = 0.0697\%$. From these values we extract $n_{th} = 0.104$, $p_r = 2.32\% \ll 1$ and $p_b = 2.37\% \ll 1$, which allows us to directly obtain $g_0/2\pi = 869 \text{ kHz}$, in good agreement with our simulated value [21]. With the calibrated value of g_0 , the scattering probabilities p_r and p_b can now be directly set by simply choosing the appropriate pulse energies. The average phonon occupation of the mechanical oscillator n_{th} can also be obtained by measuring the count rates with predetermined values of p_b and p_r , without requiring sideband thermometry.

DATA ANALYSIS

The second order autocorrelation function is defined as

$$g^{(2)}(t_1, t_2) = \frac{\langle : \hat{N}(t_1) \hat{N}(t_2) : \rangle}{\langle \hat{N}(t_2) \rangle \langle \hat{N}(t_1) \rangle}, \quad (5.4)$$

where $\hat{N}(t) = \hat{b}^\dagger(t)\hat{b}(t)$ is the phonon number operator of the mechanical mode at time t after the start of the pulse sequence, and $::$ is the notation for time and normal ordering of the operators. The mechanical mode is measured by the optical read pulses and the signal, i.e. the scattered photons, are filtered before they are detected by SNSPDs. Consequently, the observed detection events are averaged by the optical filters and weighted with the envelope of the read pulse $n_p(t)$, which holds for the weak coupling (i.e. adiabatic) regime. Further, to gain enough statistics, the events associated with the read pulse are integrated. We define the time interval $[t_a, t_b]$, containing the effective pulse shape $p(t)$, which is obtained from the actual pulse envelope $n_p(t)$ and the filter transfer function. This allows us to express the observed autocorrelation function

$$g_{obs}^{(2)}(\tau) = \frac{\int_{t_a}^{t_b} dt_1 \int_{t_a+\tau}^{t_b+\tau} dt_2 p(t_1)p(t_2) \langle : \hat{N}(t_1)\hat{N}(t_2) : \rangle}{\left(\int_{t_a}^{t_b} dt_1 p(t_1) \langle \hat{N}(t_1) \rangle \right) \left(\int_{t_a+\tau}^{t_b+\tau} dt_2 p(t_2) \langle \hat{N}(t_2) \rangle \right)}, \quad (5.5)$$

for a delay τ between two phonon measurements. This averaging does not influence the validity of the statements about sub-poissonian statistics and non-classicality of the mechanical state. Strictly speaking, within the averaging window there is a randomization of the phonon statistics due to damping and heating. Thus, a small regression towards $g^{(2)} = 1$ is expected. Due to the short averaging time, this effect is negligible compared the other uncertainties and systematic effects described below, such that we can safely assume $g^{(2)}(\tau) \equiv g^{(2)}(t_d, t_d + \tau) \approx g_{obs}^{(2)}(\tau)$, with the effective delay of the read pulse $t_d = (t_a + t_b)/2$.

A Hanbury Brown and Twiss setup with two single-photon detectors $D1$ and $D2$ with low count rates allows to measure this second order autocorrelation [30, 36]. Specifically, for $\tau = 0$, this expression reduces to the cross-correlation between those detectors

$$g^{(2)}(0) \approx g_{E_1, E_2}^{(2)} = P(E_1 \cap E_2) / P(E_1)P(E_2), \quad (5.6)$$

where $P(X)$ describes the probability of the occurrence of event X , and E_n is a detection event at detector D_n ($n = 1, 2$) during the time interval $[t_a, t_b]$. In this notation, it can easily be seen that a rescaling of the detection efficiency of either detector drops out of the expression. Consequently, $g^{(2)}$ is independent of losses in the optical path or the fidelity of the state transfer by the read pulse. However, the value of $g^{(2)}$ can be changed by measurement noise, in our case dominated by false positive detection events (caused by electronic noise, stray light or leaked pump photons). In our setup this gives a negligible systematic error $\delta g^{(2)} = g_{E_1, E_2}^{(2)} - g^{(2)}(0)$ of $0 < \delta g^{(2)} < 3 \times 10^{-4}$. If the state-swap is seen as part of the measurement, heating of the mechanical state by optical absorption of pump photons within the device can also be interpreted as measurement noise. The effect on $g^{(2)}$ depends strongly on the initial effective temperature of the mechanical mode, so that we cannot give a general number for the systematic error. From simulations, we deduce that it spans from about $0 < \delta g_{abs}^{(2)} < 0.17$ for the lowest temperature measurement to $0 < \delta g_{abs}^{(2)} < 0.02$ for the highest initial temperature. The absorption heating in combination with dead time of the SNSPDs, additionally causes a systematic error of $0 < \delta g_{dt}^{(2)} < 0.03$, which is described in detail in the following section. As the heating related effects can also be considered to be part of the actual mechanical state and

the other effects are much smaller than the statistical uncertainties, all $g^{(2)}$ values presented in this work are not corrected for these systematic errors. With all $\delta g^{(2)} > 0$, the presented values are upper bounds to the noise free auto-correlation of the mechanical state.

To estimate the statistical uncertainty of our measurement, we use the likelihood function based on a binomial distribution of photon detection events in the limit of low probabilities. The experimentally measurable values for $g_{E_1, E_2}^{(2)}(0)$ are the maximum likelihood values

$$\bar{g}_{E_1, E_2}^{(2)} \equiv \frac{C(E_1 \cap E_2)/N}{(C(E_1)/N)(C(E_2)/N)} \approx g_{E_1, E_2}^{(2)}, \quad (5.7)$$

where $C(E_1)$ ($C(E_2)$) is the number of counts registered at detector $D1$ ($D2$) and $C(E_1 \cap E_2)$ is the number of co-detection events at both detectors, all conditioned on heralding events (i.e. detection events from earlier pump pulses). N refers to the number of such heralding events. In our experiment, the uncertainty of $g_{E_1, E_2}^{(2)}$ is dominated by that of $\bar{P}(E_1 \cap E_2) \equiv C(E_1 \cap E_2)/N$, i.e. the estimated probability of $P(E_1 \cap E_2)$, as $E_1 \cap E_2$ is the rarest event among all the other events. Therefore, we use the likelihood function of $P(E_1 \cap E_2)$ to determine the confidence interval of the given values $g^{(2)}(0) = \bar{g}_{E_1, E_2}^{(2) \pm \sigma_{\pm}}$, such that the likelihood of the actual value of $g_{E_1, E_2}^{(2)}$ is 34% to be within $[\bar{g}_{E_1, E_2}^{(2)} - \sigma_{-}, \bar{g}_{E_1, E_2}^{(2)}]$ and 34% to be within $[\bar{g}_{E_1, E_2}^{(2)}, \bar{g}_{E_1, E_2}^{(2)} + \sigma_{+}]$. While the low count numbers produce skewed likelihood functions and therefore unequal upper and lower uncertainties σ_{\pm} , the counts are high enough such that the rule of thumb of requiring 3σ for statistical significance (p-value < 0.001) still holds. Specifically, our null hypothesis is no correlation between the phonons in the oscillator, i.e. an actual $g_{\text{actual}}^{(2)} = 1$. For the delay of the read pulse of $t_d = 115$ ns and $T = 35$ mK, we measured an autocorrelation of $g^{(2)}(0) = 0.647_{-0.079}^{+0.105}$. The p-value, i.e. the probability of observing this or a more extreme result, given that the null hypothesis of no correlation was true, is $p = P(\bar{g}_{E_1, E_2}^{(2)} \leq 0.647 | g_{\text{actual}}^{(2)} = 1, N = 1.2 \times 10^6) < 7 \times 10^{-4}$. In our case this coincides with the probability of falsely rejecting the classical bound $P(g_{\text{actual}}^{(2)}(0) \geq 1 | \bar{g}^{(2)}(0) = 0.647_{-0.079}^{+0.105}) < 7 \times 10^{-4}$. For the delay of $t_d = 370$ ns and $T = 35$ mK, we find the p-value $p < 0.01$ for the observed $g^{(2)}(0) = 0.832_{-0.058}^{+0.068}$, also coinciding with $P(g_{\text{actual}}^{(2)}(0) \geq 1 | g^{(2)}(0) = 0.832_{-0.058}^{+0.068}) < 0.01$.

DEAD TIME EFFECTS

In order to reduce the effects of absorption heating on the mechanical state [21, 37, 38], it is important to measure the state as quickly as possible upon its generation by the pump pulse. For the data shown in Figure 5.3b in the main text, the time delay between the read and the pump pulses is $t_d = 115$ ns. For the measurements in Figure 5.3c, t_d is set to 95 ns, except for the first data point, which represents the result of Figure 5.3b.

In our measurement scheme, we use the same pair of SNSPDs to herald the generation of non-classical mechanical states as we use to measure $g^{(2)}(0)$ through the read pulses. After a detection event, the superconducting nanowire is in the normal conducting state and is therefore blind to additional photons arriving during this time, before it cools down and returns into the superconducting state. This so-called dead time for our

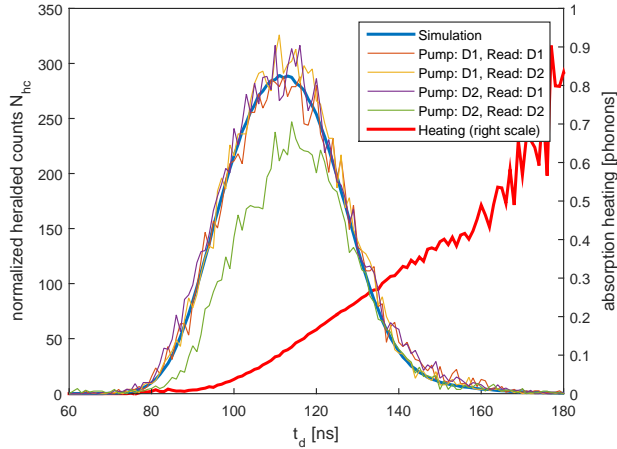


Figure 5.5: Plotted are the heralded counts for various combinations of detection events: In brown, yellow, purple and green are the counts of photons scattered by the read pulse (left axis), heralded on the detection of a photon scattered by the pump pulse. They are normalized to the detection efficiency of events heralded by detector $D1$ and detected by $D2$ (yellow). All combinations involving $D1$ either for heralding or detection match well with the simulated counting distribution (blue). Notably, the combination of heralding and detecting with $D2$ deviates from that. This reduced detection efficiency is caused by the longer dead time of $D2$ compared to $D1$. In addition, the time window over which the pulse averages, is shifted to later times and is more heavily influenced by the cumulative heating $n_{abs}(t)$ (red) by absorbed driving photons from the read pulse. The latter is extracted from the detection of a thermal state and compensated for the optomechanical cooling to obtain the true cumulative number of added phonons $n_{abs}(t)$ (right axis).

detectors is nominally on the order of 50 – 70 ns. If the state is heralded by one of the SNSPDs and its dead time overlaps with the arrival time of the photons from the read pulse, its detection efficiency will be lower than the nominal value. In our experiment this is in fact the case for detector $D2$ in the measurement of $g^{(2)}(0)$ with $t_d = 115$ ns (cf. Figure 5.5).

To first approximation, this should have no influence on the value of $g^{(2)}(0)$ itself, as the detection probability of the heralded pulses enters equation (5.6) in the numerator $P(E_1 \cap E_2)$ and the denominator $P(E_2)$ in the same way. However, a detected readout pulse with a seemingly distorted shape as in Figure 5.5 effectively measures the mechanical state slightly later than the nominal delay time t_d . Due to absorption heating during the read pulse (cf. Figure 5.5), the mechanical state at later times is corrupted by the influx of thermal phonons $\dot{n}_{abs}(t)$. Therefore, it will increase the observed value of $g^{(2)}(0)$ towards 2, the value of a thermal state. For this reason we discard heralding events from detector $D2$ for short delays.

A more detailed analysis allows us to quantify the systematic error by the shorter dead time of detector $D1$. The minor reduction of the detection efficiency for a t_d of 115 ns leads to $0 < \delta g_{dt}^{(2)} < 0.01$, which corresponds to an overestimation of our observed value of $g^{(2)}(0)$ by much less than our statistical uncertainty. For $t_d = 95$ ns, this effect from detector $D1$ becomes stronger, resulting in 10% reduced detection efficiency. However, thanks to an increased thermal background, it only produces a systematic error

of around $0 < \delta g_{dt}^{(2)} < 0.03$, which is again smaller than the statistical uncertainty. As they are negligible in magnitude, we did not account for these systematic errors in the reported values of $g^{(2)}$ in the main text.

SIMULATION OF THE CORRELATION FUNCTION

To calculate the expected value of $g^{(2)}$ we use the formalism developed by Barchielli [39, 40]. In order to do this, we require a model of the open-system dynamics of our optomechanical system, describing the coupling to the environment. In addition to the typical assumption that the mechanical system couples to a heat bath of a fixed temperature, we observe in our experiment an additional, time-dependent heating effect that is activated by the strong read pulse. In the absence of a microscopic description of this effect, we adopt a simple phenomenological description and model it as a standard Lindblad dynamics with two parameters γ and n_{bath} , which can be estimated from the singlefold detection events of the experimental $g^{(2)}$ data for each n_{init} . Note that n_{bath} is not the occupation number determined by the dilution refrigerator and is assumed to be a function of time. In essence, the incoherent (thermal) phonon influx $\dot{n}_{abs} = \gamma n_{bath}(t)$ is the derivative of the cumulative absorption heating and can be extracted from singlefold detection events, with calibrated scattering rates from sideband asymmetry measurements (see above) and knowledge of the envelope of the read pulse (cf. Figure 5.5). The mechanical decay rate γ is assumed to be the measured decay rate ω_m/Q_m . The Lindblad dynamics stay identical when coupling to a number of different baths with different coupling strengths, as long as the phonon influx and the mechanical decay rate stay constant. For reasons of simplicity, we therefore work with a single phenomenological phonon influx $\gamma \times n_{bath}(t)$.

The evolution of the optomechanical quantum state ρ under open-system dynamics can be described by a Lindblad master equation [41] of the form [42]

$$\dot{\rho} = \mathcal{L}\rho = -\frac{i}{\hbar}[H_{swap}(t), \rho] + \kappa\mathcal{D}[a]\rho + \gamma(n_{bath}(t) + 1)\mathcal{D}[b]\rho + \gamma n_{bath}(t)\mathcal{D}[b^\dagger]\rho, \quad (5.8)$$

where the time dependence in H_{swap} accounts for the time-dependent drive by the light pulses. The Lindblad terms,

$$\mathcal{D}[s]\rho = s\rho s^\dagger - \frac{1}{2}(s^\dagger s\rho + \rho s^\dagger s), \quad (5.9)$$

describe the coupling of the system to its electromagnetic environment (second term in eq. (5.8)) and the mechanical heat bath with a mean occupation number n_{bath} (third and fourth term in eq. (5.8)). Below we will write the formal solution of eq. (5.8) as $\rho(t) = \mathcal{T}(t, t_0)\rho(t_0)$.

To describe a photon-counting measurement with a quantum efficiency η , we iteratively solve the master equation as [43]

$$\rho(t) = \mathcal{S}(t, t_0)\rho(t_0) + \sum_{m=1}^{\infty} \int_0^t dt_m \dots \int_0^{t_2} dt_1 \mathcal{S}(t, t_m) \mathcal{J}\mathcal{S}(t, t_{m-1}) \dots \mathcal{J}\mathcal{S}(t_1, 0)\rho(t_0), \quad (5.10)$$

where we defined the operator $\mathcal{J}\rho = \eta\kappa a\rho a^\dagger$ (which corresponds to the emission of one photon from the cavity), and the propagator \mathcal{S} that solves the effective evolution $\dot{\mathcal{S}} = (\mathcal{L} - \mathcal{J})\mathcal{S}$. Equation (5.10) allows for the following interpretation: Assuming that we register m photons on the photo-detector, the *conditional* state of the system is, up to a normalizing factor, given by the m -th term in the sum above. In case no photons are registered, the unnormalized conditional state is given by $\mathcal{S}(t, t_0)\rho(t_0)$ instead. The heralded state of the mechanical system after the blue-detuned write pulse (for a click of the detector at time t_{click}) is thus given by

$$\rho_{click} = \frac{\text{Tr}_{cav}[\mathcal{J}(t_{click}, t_0)\rho(t_0) - \mathcal{S}(t_{click}, t_0)\rho(t_0)]}{\text{Tr}[\mathcal{J}(t_{click}, t_0)\rho(t_0) - \mathcal{S}(t_{click}, t_0)\rho(t_0)]}. \quad (5.11)$$

Note that this state is conditioned on a measurement of *at least* one phonon. For our case where two-fold events are rare, this effectively reduces to the first term in the sum in eq. (5.10), i.e., $\rho_{click} \propto \text{Tr}_{cav}[a^\dagger a \mathcal{S}(t_{click}, t_0)\rho(t_0)]$.

As the evaluation of $g^{(2)}$ is computationally expensive, we first adiabatically eliminate the cavity mode from eq. (5.8), which is possible in the weak-coupling limit $g_0 \times \sqrt{n_c} \ll \kappa$. For the case of the red-detuned read pulse we find the equation (neglecting the very weak optical-spring effect) [42]

$$\dot{\rho}_m = [\gamma(n_{bath} + 1) + \Gamma_-(t)]\mathcal{D}[b]\rho_m + (\gamma n_{bath} + \Gamma_+(t))\mathcal{D}[b^\dagger]\rho_m, \quad (5.12)$$

for the reduced state of the mechanical system ρ_m , with $\Gamma_\pm(t) = 2\kappa_e/\kappa \times g_0^2 n_c(t) \text{Re}(\eta_\pm)$, $\eta_- = 2/\kappa$, $\eta_+ = 2/(\kappa + 4i\omega_m)$. In this approximation the photo-counting measurement at the cavity resonance frequency is described by $\mathcal{J}(t)\rho = \eta\Gamma_-(t)b\rho b^\dagger$.

To calculate $g^{(2)}$ of the photons emitted from the cavity (after heralding) we need to evaluate time- and normal-ordered expectation values of the cavity output field, which is readily achieved in this formalism. We find [40]

$$\langle \hat{I}(t_1) \rangle = \text{Tr}[\mathcal{J}(t_1)\mathcal{J}(t_1, t_{click})\rho_{click}], \quad (5.13)$$

$$\langle : \hat{I}(t_1)\hat{I}(t_2) : \rangle = \text{Tr}[\mathcal{J}(t_2)\mathcal{J}(t_2, t_1)\mathcal{J}(t_1)\mathcal{J}(t_1, t_{click})\rho_{click}]. \quad (5.14)$$

To evaluate equations (5.13) and (5.14), we expand the mechanical operators in a number basis up to a maximal phonon number of 50. We assume the mechanical system to initially be in a thermal state with a mean phonon number n_{init} . In optomechanical crystals, the mechanical damping rate γ tends to be a function of the environmental temperature. As $\gamma \times n_{bath}$ is effectively treated as a single parameter \dot{n}_{abs} and the time scale of the simulation is short compared to the mechanical decay time $1/\gamma$, potential changes of γ with the bath temperature by up to one order of magnitude do not influence the simulations significantly.

NON-CLASSICALITY AND $g^{(2)}$

The degree of second order coherence $g^{(2)}$ allows to draw various conclusions on the system under investigation. The most prominent use of $g^{(2)}$ is to violate the non-classicality

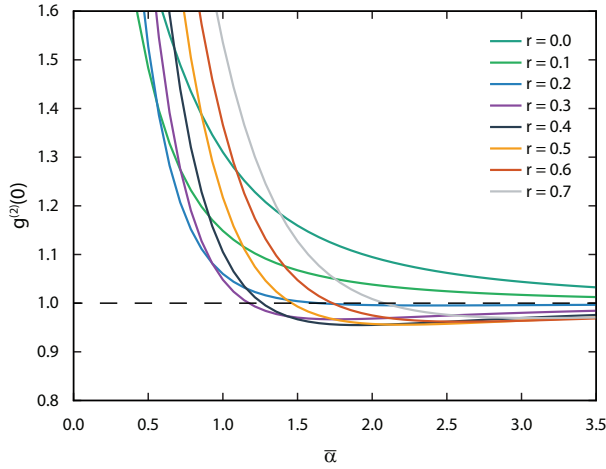


Figure 5.6: Shown is the numerically calculated $g^{(2)}$ function of a squeezed Gaussian state with an initial thermal occupation of $n_{init} = 0.20$ as a function of displacement $\bar{\alpha}$ and squeezing parameter r (color-coded) for $\theta = 2\phi$. Even for the optimal choice of settings $r = 0.44$ and $\bar{\alpha} = 2.00$, such a model cannot explain our data.

bound as described in the main text. The physical meaning of this bound can be inferred from the variance of the energy $\hat{H} = \hbar\omega_m \hat{b}^\dagger \hat{b}$ of the free mechanical oscillator.

$$\text{Var}(\hat{H}) = \langle \hat{H}^2 \rangle - \langle \hat{H} \rangle^2 = (g^{(2)}(0) - 1) \langle \hat{H} \rangle^2 + \hbar\omega_m \langle \hat{H} \rangle. \quad (5.15)$$

For classical physics, i.e. not applying canonical quantization, $\langle : \hat{H}^2 : \rangle = \langle \hat{H}^2 \rangle$ and therefore the last term, stemming from the commutation relations, drops out. It immediately follows from $\text{Var}(\hat{H}) \geq 0$ that $g^{(2)}(0) \geq 1$. When using the canonical quantization, we can infer from $g^{(2)}(0) < 1$ that the source had sub-Poissonian phonon statistics. This also classifies the mechanical state as "non-classical" in the sense that it cannot be represented as an incoherent mixture of coherent states [12]. The degree of second order coherence $g^{(2)}$ can be used to test against stricter bounds as well [44], some of them depending on the physical system under investigation. For two level systems it is for example important to demonstrate that only a single emitter is present. This can be done by demonstrating $g^{(2)}(0) < 0.5$ [45]. In our case it is sufficient to show $g^{(2)}(0) < 1$ as we only have a single macroscopic oscillator by design.

As we can see from equation (5.15), states possessing a small variance and/or low energies can also exhibit $g^{(2)}(0) < 1$. One set of states, which is interesting to exclude is incoherent mixtures of Gaussian states. In general, linear bosonic systems that involve squeezing can exhibit $g^{(2)}(0) < 1$. This has recently been theoretically shown in the context of optomechanics [46]. Using these models we numerically calculate $g^{(2)}(0)$ for a general mechanical single-mode Gaussian state undergoing squeezing. For this, we use the most favorable parameters observed in our correlation experiments. We start from an initial thermal state $\hat{\rho}_{init}$ with $n_{init} = 0.20$ phonons, which corresponds to the lowest temperature observed in the correlation measurements. The state is assumed to be purely thermal, which is in agreement with the experimentally observed

autocorrelation of the pump pulse of $g^{(2)}(0) = 2.0_{-0.1}^{+0.1}$. Neglecting any heating from the optical pulses, we apply displacement $\hat{D}(\alpha) = \exp[\alpha\hat{b}^\dagger - \alpha^*\hat{b}]$ and squeezing operations $\hat{S}(\xi) = \exp[\frac{1}{2}(\xi^*\hat{b}^2 - \xi\hat{b}^{\dagger 2})]$ with variable $\alpha = \bar{\alpha}e^{i\phi}$ and $\xi = re^{i\theta}$ ($\bar{\alpha}, r > 0$). We then numerically minimize $g^{(2)}(0)$ of the resulting states $\hat{\rho} = \hat{D}(\alpha)\hat{S}(\xi)\hat{\rho}_{init}\hat{S}^\dagger(\xi)\hat{D}^\dagger(\alpha)$ as a function of α and ξ using the quantum toolbox QuTiP [47, 48]. The minimal correlation we can obtain is $g^{(2)}(0) \approx 0.95$, with $r = 0.44$ and $\bar{\alpha} = 2.00$ for $\theta = 2\phi$, clearly exceeding our experimentally measured value, as shown in Fig. 5.6. This simple model therefore allows us to exclude, with a p-value of 0.002, the possibility that the states we generate are in fact squeezed Gaussian states. When additionally limiting the mean occupation $n = \text{Tr}[\hat{\rho}\hat{b}^\dagger\hat{b}]$ to the experimentally observed occupation number of the heralded states, $1.25 < n < 1.90$, we get a minimum $g^{(2)}(0) \approx 0.99$, rejecting the hypothesis of observing a squeezed state with even stronger statistical confidence.

REFERENCES

- [1] R. H. Brown and R. Q. Twiss, *Correlation between photons in two coherent beams of light*, Nature **177**, 27 (1956).
- [2] R. H. Brown and R. Q. Twiss, *A test of a new type of stellar interferometer on sirius*, Nature **178**, 1046 (1956).
- [3] B. L. Morgan and L. Mandel, *Measurement of photon bunching in a thermal light beam*, Phys. Rev. Lett. (1966).
- [4] M. Henny, S. Oberholzer, C. Strunk, T. Heinzel, K. Ensslin, M. Holland, and C. Schönnenberger, *The fermionic hanbury brown and twiss experiment*, Science **284**, 296 (1999).
- [5] W. D. Oliver, J. Kim, R. C. Liu, and Y. Yamamoto, *Hanbury brown and twiss-type experiment with electrons*, Science **284**, 299 (1999).
- [6] T. Jelte, J. M. McNamara, W. Hogervorst, W. Vassen, V. Krachmalnicoff, M. Schellekens, A. Perrin, H. Chang, D. Boiron, A. Aspect, and C. I. Westbrook, *Comparison of the hanbury brown twiss effect for bosons and fermions*, Nature **445**, 402 (2007).
- [7] P. Grangier, G. Roger, and A. Aspect, *Experimental evidence for a photon anticorrelation effect on a beam splitter: a new light on single-photon interference*, Europhys. Lett. **1**, 173 (1986).
- [8] M. D. Eisamana, J. Fan, A. Migdall, and S. V. Polyakov, *Single-photon sources and detectors*, Rev. Sci. Instrum. **82**, 071101 (2011).
- [9] X. T. Zou and L. Mandel, *Photon-antibunching and sub-poissonian photon statistics*, Phys. Rev. A **41**, 475 (1990).
- [10] L. Davidovich, *Sub-poissonian processes in quantum optics*, Rev. Mod. Phys. **68**, 127 (1996).

- [11] H. J. Kimble, M. Dagenais, and L. Mandel, *Photon antibunching in resonance fluorescence*, Phys. Rev. Lett. **39**, 691 (1977).
- [12] R. Short and L. Mandel, *Observation of sub-poissonian photon statistics*, Phys. Rev. Lett. **51**, 384 (1983).
- [13] R. Blatt and D. Wineland, *Entangled states of trapped atomic ions*, Nature **453**, 1008 (2008).
- [14] D. Leibfried, D. M. Meekhof, B. E. King, C. Monroe, W. M. Itano, and D. J. Wineland, *Experimental determination of the motional quantum state of a trapped atom*, Phys. Rev. Lett. **77**, 4281 (1996).
- [15] J. I. Cirac and P. Zoller, *Quantum computations with cold trapped ions*, Phys. Rev. Lett. **74**, 4091 (1995).
- [16] M. Aspelmeyer, T. J. Kippenberg, and F. Marquardt, *Cavity optomechanics*, Rev. Mod. Phys. **86**, 1391 (2014).
- [17] J. D. Teufel, T. Donner, D. Li, J. W. Harlow, M. S. Allman, K. Cicak, A. J. Sirois, J. D. Whittaker, K. W. Lehnert, and R. W. Simmonds, *Sideband cooling of micromechanical motion to the quantum ground state*, Nature **475**, 359 (2011).
- [18] J. Chan, T. P. M. Alegre, A. H. Safavi-Naeini, J. T. Hill, A. Krause, S. Gröblacher, M. Aspelmeyer, and O. Painter, *Laser cooling of a nanomechanical oscillator into its quantum ground state*, Nature **478**, 89 (2011).
- [19] T. Palomaki, J. Teufel, R. Simmonds, and K. Lehnert, *Entangling mechanical motion with microwave fields*, Science **342**, 710 (2013).
- [20] K. C. Lee, M. R. Sprague, B. J. Sussman, J. Nunn, N. K. Langford, X.-M. Jin, T. Champion, P. Michelberger, K. F. Reim, D. England, D. Jaksch, and I. Walmsley, *Entangling macroscopic diamonds at room temperature*. Science **334**, 1253 (2011).
- [21] R. Riedinger, S. Hong, R. A. Norte, J. A. Slater, J. Shang, A. G. Krause, V. Anant, M. Aspelmeyer, and S. Gröblacher, *Non-classical correlations between single photons and phonons from a mechanical oscillator*, Nature **530**, 313 (2016).
- [22] E. E. Wollman, C. U. Lei, A. J. Weinstein, J. Suh, A. Kronwald, F. Marquardt, A. A. Clerk, and K. C. Schwab, *Quantum squeezing of motion in a mechanical resonator*, Science **349**, 952 (2015).
- [23] J.-M. Pirkkalainen, E. Damskäg, M. Brandt, F. Massel, and M. A. Sillanpää, *Squeezing of quantum noise of motion in a micromechanical resonator*, Phys. Rev. Lett. **115**, 243601 (2015).
- [24] F. Lecocq, J. B. Clark, R. W. Simmonds, J. Aumentado, and J. D. Teufel, *Quantum nondemolition measurement of a nonclassical state of a massive object*, Phys. Rev. X **5**, 041037 (2015).

- [25] A. D. O'Connell, M. Hofheinz, M. Ansmann, R. C. Bialczak, M. Lenander, E. Lucero, M. Neeley, D. Sank, H. Wang, M. Weides, J. Wenner, J. M. Martinis, and A. N. Cleland, *Quantum ground state and single-phonon control of a mechanical resonator*, *Nature* **464**, 697 (2010).
- [26] Y. Chu, P. Kharel, W. H. Renninger, L. D. Burkhardt, L. Frunzio, P. T. Rakich, and R. J. Schoelkopf, *Quantum acoustics with superconducting qubits*, *Science* **358**, 199 (2017).
- [27] A. P. Reed, K. H. Mayer, J. D. Teufel, L. D. Burkhardt, W. Pfaff, M. Reagor, L. Sletten, X. Ma, R. J. Schoelkopf, E. Knill, and K. W. Lehnert, *Faithful conversion of propagating quantum information to mechanical motion*, *Nature Phys.* **13**, 1163 (2017).
- [28] K. C. Lee, B. J. Sussman, M. R. Sprague, P. Michelberger, K. F. Reim, J. Nunn, N. K. Langford, P. J. Bustard, D. Jaksch, and I. A. Walmsley, *Macroscopic non-classical states and terahertz quantum processing in room-temperature diamond*, *Nat. Photon.* **6**, 41 (2012).
- [29] J. D. Cohen, S. M. Meenehan, G. S. MacCabe, S. Gröblacher, A. H. Safavi-Naeini, F. Marsili, M. D. Shaw, and O. Painter, *Phonon counting and intensity interferometry of a nanomechanical resonator*, *Nature* **520**, 522 (2015).
- [30] S. G. Hofer, W. Wieczorek, M. Aspelmeyer, and K. Hammerer, *Quantum entanglement and teleportation in pulsed cavity optomechanics*, *Phys. Rev. A* **84**, 52327 (2011).
- [31] See supplementary materials .
- [32] W. Kern and D. A. Puotinen, *Cleaning solutions based on hydrogen peroxide for use in silicon semiconductor technology*, *RCA Rev.* **31**, 187 (1970).
- [33] J. Chan, *Laser cooling of an optomechanical crystal resonator to its quantum ground state of motion*, Ph.D. thesis, California Institute of Technology (2012).
- [34] R. N. Patel, C. J. Sarabalis, W. Jiang, J. T. Hill, and A. H. Safavi-Naeini, *Engineering phonon leakage in nanomechanical resonators*, *Phys. Rev. Applied* **8**, 041001 (2017).
- [35] C. W. Chou, S. V. Polyakov, A. Kuzmich, and H. J. Kimble, *Single-photon generation from stored excitation in an atomic ensemble*, *Phys. Rev. Lett.* **92**, 213601 (2004).
- [36] C. Galland, N. Sangouard, N. Piro, N. Gisin, and T. J. Kippenberg, *Heralded Single-Phonon Preparation, Storage, and Readout in Cavity Optomechanics*, *Phys. Rev. Lett.* **112**, 143602 (2014).
- [37] S. M. Meenehan, J. D. Cohen, G. S. MacCabe, F. Marsili, M. D. Shaw, and O. Painter, *Pulsed Excitation Dynamics of an Optomechanical Crystal Resonator near Its Quantum Ground State of Motion*, *Phys. Rev. X* **5**, 041002 (2015).
- [38] S. M. Meenehan, J. D. Cohen, S. Gröblacher, J. T. Hill, A. H. Safavi-Naeini, M. Aspelmeyer, and O. Painter, *Silicon optomechanical crystal resonator at millikelvin temperatures*, *Phys. Rev. A* **90**, 011803 (2014).

- [39] A. Barchielli, *Quantum stochastic differential equations: an application to the electron shelving effect*, J. Phys. A **20**, 6341 (1987).
- [40] A. Barchielli, *Direct and heterodyne detection and other applications of quantum stochastic calculus to quantum optics*, Quantum Opt. **2**, 423 (1990).
- [41] G. Lindblad, *On the generators of quantum dynamical semigroups*, Commun. Math. Phys. **48**, 119 (1976).
- [42] I. Wilson-Rae, N. Nooshi, W. Zwerger, and T. J. Kippenberg, *Theory of ground state cooling of a mechanical oscillator using dynamical back-action*, Phys. Rev. Lett. **99**, 093901 (2007).
- [43] C. W. Gardiner and P. Zoller, *Quantum Noise* (Springer Series in Synergetics, 2004).
- [44] R. Filip and L. Lachman, *Hierarchy of feasible nonclassicality criteria for sources of photons*, Phys. Rev. A **88**, 043827 (2013).
- [45] W. M. Itano, J. C. Bergquist, and D. J. Wineland, *Photon antibunching and sub-poissonian statistics from quantum jumps in one and two atoms*, Phys. Rev. A **38**, 559(R) (1988).
- [46] M.-A. Lemonde, N. Didier, and A. A. Clerk, *Antibunching and unconventional photon blockade with gaussian squeezed states*, Phys. Rev. A **90**, 063824 (2014).
- [47] J. R. Johansson, P. D. Nation, and F. Nori, *Qutip: An open-source python framework for the dynamics of open quantum systems*, Comp. Phys. Comm. **183**, 1760 (2012).
- [48] J. R. Johansson, P. D. Nation, and F. Nori, *Qutip 2: A python framework for the dynamics of open quantum systems*, Comp. Phys. Comm. **184**, 1234 (2013).

6

OPTOMECHANICAL BELL TEST

**Igor Marinković^{*}, Andreas Wallucks^{*}, Ralf Riedinger,
Sungkun Hong, Markus Aspelmeyer, Simon Gröblacher**

Over the past few decades, experimental tests of Bell-type inequalities have been at the forefront of understanding quantum mechanics and its implications. These strong bounds on specific measurements on a physical system originate from some of the most fundamental concepts of classical physics – in particular that properties of an object are well defined independent of measurements (realism) and only affected by local interactions (locality). The violation of these bounds unambiguously shows that the measured system does not behave classically, void of any assumption on the validity of quantum theory. It has also found applications in quantum technologies for certifying the suitability of devices for generating quantum randomness, distributing secret keys and for quantum computing. Here we report on the violation of a Bell inequality involving a massive, macroscopic mechanical system. We create light-matter entanglement between the vibrational motion of two silicon optomechanical oscillators, each comprising approx. 10^{10} atoms, and two optical modes. This state allows us to violate a Bell inequality by more than 4 standard deviations, directly confirming the non-classical behavior of our optomechanical system under the fair sampling assumption.

^{*} equal contribution

This chapter has been published in Phys.Rev.Lett.**121**, 220404(2018)

6.1. MAIN TEXT

Bell's theorem [1] predicts that any local realistic theory is at variance with quantum mechanics. It was originally conceived to settle an argument between Einstein [2] and Bohr [3] on locality in physics, and to investigate the axioms of quantum physics. First tests of the Clauser-Horne-Shimony-Holt (CHSH) inequality [4], an experimentally testable version of Bell's original inequality, were performed with photons from cascaded decays of atoms [5, 6] and parametric down-conversion [7–9]. Subsequent experiments reduced the set of assumptions required for the falsification of classical theories, closing, e.g., the locality [10] and detection loopholes [11], first individually and recently simultaneously [12–15]. In addition to the fundamental importance of these experiments, the violation of a Bell-type inequality has very practical implications – in particular, it has become the most important benchmark for thrust-worthily verifying entanglement in various systems [16, 17], including mesoscopic superconducting circuits [18], for certifying randomness [19, 20], secret keys [21], and quantum computing [22].

While the standard form of quantum theory does not impose any limits on the mass or size of a quantum system [23], the potential persistence of quantum effects on a macroscopic scale seems to contradict the human experience of classical physics. Over the past years, quantum optomechanics has emerged as a new research field, coupling mechanical oscillators to optical fields. While these systems are very promising for quantum information applications due to their complete engineerability, they also hold great potential to test quantum physics on a new mass scale. Recent experiments have demonstrated quantum control of such mechanical systems, including mechanical squeezing [24], single-phonon manipulation [25–28], as well as entanglement between light and mechanics [29] and entanglement between two mechanical modes [30–32]. However, explaining the observed results in these experiments required assuming the validity of quantum theory at some level. A Bell test, in contrast, is a genuine test of non-classicality without quantum assumptions.

Here we report on the first Bell test using correlations between light and microfabricated mechanical resonators, which constitute massive macroscopic objects, hence verifying non-classical behavior of our system without relying on the quantum formalism. Bell-tests do not require assumptions about the physical implementation of a quantum system such as the dimension of the underlying Hilbert space or the fundamental interactions involved in state preparation and measurement [33]. The violation of a Bell-inequality is hence the most unambiguous demonstration of entanglement with numerous important implications. From a fundamental perspective, the robust entanglement between flying optical photons and a stored mechanical state rules out local hidden-variables, which can be used for further tests of quantum mechanics at even larger mass scales [34, 35]. From an application perspective, the presented measurements also imply that optomechanics is a promising technique to be used for quantum information processing tasks including teleportation, quantum memories and the possibility of quantum communication with device-independent security [21].

The optomechanical structures used in this work are two photonic crystal nanobeams on two separate chips. They are designed to have an optical resonance in the telecom band that is coupled to a co-localized, high-frequency mechanical mode [36]. Each device is placed in one of the arms of an actively stabilized fiber interferometer (see [31] and

SI for additional details). The resonators are cryogenically cooled close to their motional ground state inside a dilution refrigerator. Our entanglement creation and verification protocol consists of two optical control pulses that give rise to linearized optomechanical interactions, addressing the Stokes and anti-Stokes transitions of the system (see Figure 6.1). Both types of interactions result in scattered photons that are resonant with the cavity and can be efficiently filtered from the drive beams before being detected by superconducting nanowire single photon detectors (SNSPDs).

A blue detuned, ~ 40 ns long laser pulse with frequency $\nu_b = \nu_o + \nu_m$ (ν_o optical resonance, ν_m mechanical resonance) generates photon-phonon pairs. The interaction in this case is described by $\hat{H}_b = -\hbar g_0 \sqrt{n_b} \hat{a}^\dagger \hat{b}^\dagger + \text{h.c.}$, with the intracavity photon number n_b , the optomechanical single photon coupling g_0 and the optical (mechanical) creation operators \hat{a}^\dagger (\hat{b}^\dagger). This correlates the number of mechanical and optical excitations in each of the arms of the interferometer as

$$|\psi\rangle \propto (|00\rangle_{\text{om}} + \epsilon|11\rangle_{\text{om}} + \mathcal{O}(\epsilon^2)), \quad (6.1)$$

where o denotes the optical and m the mechanical mode, while $p = \epsilon^2$ is the excitation probability. For small $p \ll 1$, states with multiple excitations are unlikely to occur, and can therefore be neglected in the statistical analysis. Driving the devices simultaneously and post-selecting on trials with a successful detection of both the Stokes-photon and the phonon, we approximate the combined state as

$$\begin{aligned} |\Psi\rangle &= \frac{1}{\sqrt{2}} (|11\rangle_A |00\rangle_B + e^{i\phi_b} |00\rangle_A |11\rangle_B) \\ &= \frac{1}{\sqrt{2}} (|AA\rangle_{\text{om}} + e^{i\phi_b} |BB\rangle_{\text{om}}), \end{aligned} \quad (6.2)$$

again neglecting higher order excitations. Here ϕ_b is the phase difference that the blue drives acquire in the two interferometer paths A and B, including the phase shift of the first beam splitter. Expressing the state in a path basis $|A\rangle_x = |10\rangle_{AB}$, where x is o for the photonic and m for the phononic subsystem in arm A and B, allows to identify the Bell-state, similarly to polarization entanglement in optical down-conversion experiments. Unlike the two mode entangled mechanical state in [31], this four-mode entangled optomechanical state allows us to realize a Bell measurement of the type suggested by Horne, Shimony and Zeilinger [37] and first demonstrated by Rarity and Tapster [8] involving two-particle interference between four different modes. In order to access interferences between the mechanical modes, we convert the phonons into photons using a red detuned laser pulse (duration ~ 40 ns, drive frequency $\nu_r = \nu_o - \nu_m$). This realizes an optomechanical beamsplitter interaction which allows for a state transfer ($\hat{H}_r = -\hbar g_0 \sqrt{n_r} \hat{a}^\dagger \hat{b} + \text{h.c.}$, with the intracavity photon number n_r). Note that this can also be described as a classical mapping process. The optical readout fields in the interferometer arms are again recombined on a beam splitter, after which the state of Stokes / anti-Stokes field is

$$\begin{aligned} |\Phi\rangle &= \frac{1}{2\sqrt{2}} [(1 - e^{i(\phi_b + \phi_r)})(\hat{a}_{r1}^\dagger \hat{a}_{b1}^\dagger - \hat{a}_{r2}^\dagger \hat{a}_{b2}^\dagger) \\ &+ i(1 + e^{i(\phi_b + \phi_r)})(\hat{a}_{r1}^\dagger \hat{a}_{b2}^\dagger + \hat{a}_{r2}^\dagger \hat{a}_{b1}^\dagger)] |0000\rangle. \end{aligned} \quad (6.3)$$

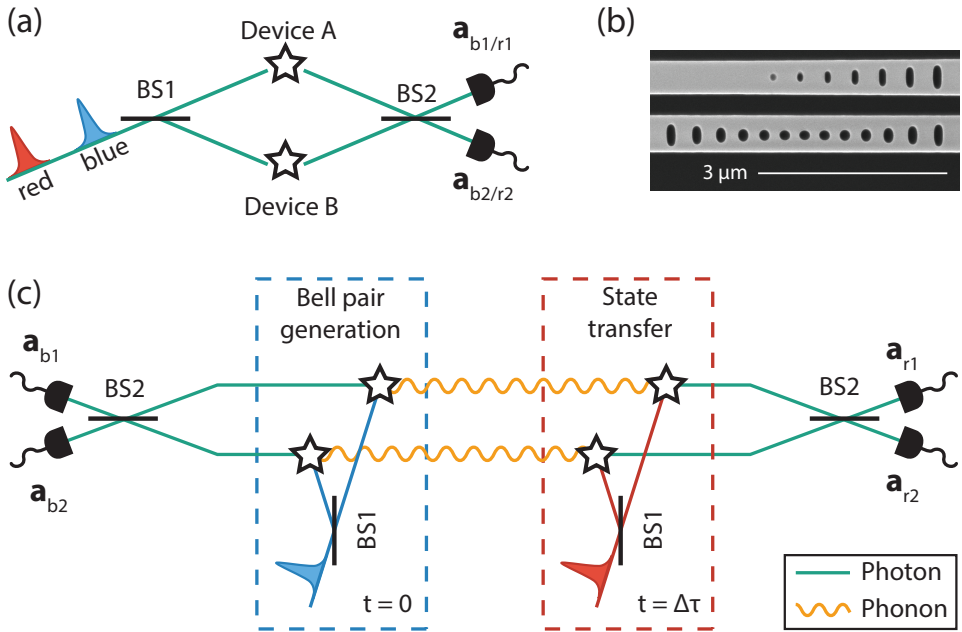


Figure 6.1: (a) Schematic of the setup: blue detuned drive pulses interact with the mechanical resonators (devices A & B) producing entangled photon-phonon pairs. The light-matter entanglement is in the path basis (A or B), corresponding to the device in which the Stokes scattering event took place. The generated photons are detected in single-photon detectors giving the measurement results a_{b1} and a_{b2} . The detection of the phonons is done by transferring their states to another optical mode by using a red drive after some time $\Delta\tau$ and subsequently obtaining the results a_{r1} and a_{r2} . Note that for technical reasons the photons created by the blue and red drives are detected on the same pair of detectors, but with a time delay $\Delta\tau = 200$ ns. Therefore we have time-separation of the two parties of the Bell test instead of space-separation (as commonly done). BS1/2 represent beamsplitter 1/2. (b) Scanning electron microscope image of one of the optomechanical devices, represented with a star-symbol in (a) and (c), next to the coupling waveguide (top). (c) Illustration of our experimental sequence: one party of the Bell test measures in which detector path the Stokes photon is found at time $t = 0$, while the other performs the same measurement for the anti-Stokes photon after a time $t = \Delta\tau$. We probe their correlations in order to violate the CHSH inequality. Since the two photons never interacted directly (only through the mechanics), the observed correlations are a direct consequence of the correlations between the Stokes photons and phonons.

Here we express the detected fields in terms of their creation operators with labels b (r) for photons scattered from the blue (red) drive and 1 (2) for the two detectors (cf. Fig. 6.1). Furthermore ϕ_r is the phase difference that the red detuned pulse photons acquire in the two arms of the interferometer. Since experimentally the mechanical frequencies of the devices differ by a small offset $\Delta\nu_m$ (see below), the state acquires an additional phase $\Omega = \Delta\nu_m\Delta\tau$, where $\Delta\tau$ is the delay between the blue and red pulses. In all data below, however, we keep $\Delta\tau$ fixed such that we can treat it as constant and set $\Omega = 0$. Typically, Bell experiments are done by rotating the measurement basis in which each particle is detected. Equivalently, the state itself can be rotated, while keeping the measurement basis fixed. In our experiment we choose the latter option, as this is simpler to implement in our setup. We achieve this by applying a phase shift with an

electro-optical modulator (EOM) in arm A of the interferometer, with which we can vary ϕ_b and ϕ_r independently (see SI). This allows us to select the relative angles between the photonic and phononic states.

In our experiment, the optical resonances are at a wavelength of $\lambda = 1550.4$ nm with a relative mismatch of $\Delta\nu_o \approx 150$ MHz. The mechanical modes have frequencies of $\nu_m = 5.101$ GHz and 5.099 GHz for device A and B, respectively. The bare optomechanical coupling rate $g_0/2\pi$ is 910 kHz for device A and 950 kHz for device B. While the optical mismatch is much smaller than the linewidth $\Delta\nu_o \ll \kappa \sim 1$ GHz such that the devices are sufficiently identical, the mechanical mismatch requires optical compensation. This is realized using the EOM in arm A of the interferometer to ensure that the scattered photons from each arm interfere with a well defined phase on the second beamsplitter (see also SI).

At the base temperature of the dilution refrigerator of around 12 mK we obtain the phonon temperature of the mechanical modes by performing sideband asymmetry measurements [38]. The measured thermal occupations for both devices is $n_{\text{init}} \leq 0.09$. We determine the lifetimes of the phonons in our structures to be $\tau_A = 3.3 \pm 0.5$ μs and $\tau_B = 3.6 \pm 0.7$ μs using a pump-probe type experiment in which we excite the devices and vary the delay to the readout pulse. To re-initialize the devices in their groundstates prior to each measurement trial, we repeat the drive sequence every 50 μs , leaving more than 10 times their lifetime for thermalization with the environment. Furthermore, we set the delay between the blue and red detuned pulses to $\Delta\tau = 200$ ns. The pulse energies for the Bell inequality experiment are chosen such that the excitation probability is 0.8% (1%), while the readout efficiency is 3% (4.1%) for device A (device B). These probabilities match the number of optomechanically generated photons for each device at the beamsplitter.

To characterize the performance of the devices, we first perform cross-correlation measurements of the photons scattered from blue and red drives on each individual optomechanical system. With the above mentioned settings, we obtain normalized cross-correlation values of $g_{\text{br,A}}^{(2)} = 9.3 \pm 0.5$ and $g_{\text{br,B}}^{(2)} = 11.2 \pm 0.6$ [38]. We can use this to estimate the expected interferometric visibility for the experiments below as $V_{\text{xpcd}} = \frac{g_{\text{br}}^{(2)} - 1}{g_{\text{br}}^{(2)} + 1}$ [39]. As there is a small mismatch in the observed cross-correlations of the two devices, we use the smaller value of device A, which results in an expected visibility of around $V_{\text{xpcd}} = 81\%$.

In order to experimentally test a Bell inequality, we then drive the two devices simultaneously in a Mach-Zehnder interferometer (see Fig. 6.1 and SI). We define the correlation coefficients

$$E(\phi_b, \phi_r) = \frac{n_{11} + n_{22} - n_{12} - n_{21}}{n_{11} + n_{22} + n_{12} + n_{21}}. \quad (6.4)$$

Here n_{ij} represents the number of detected coincidences scattered from blue (i) and red (j) pulses on the two detectors ($i, j = 1, 2$), such that e.g. n_{21} is the number of trials where the blue drive resulted in an event on detector 2, whereas the consecutive red drive on detector 1. The visibility V is given as the maximum correlation coefficient $V = |E(\phi_b, \phi_r)|_{\text{max}}$. We measure the correlation coefficients for various phase settings for the blue (ϕ_b) and red (ϕ_r) pulses, as shown in Figure 6.2. Strong correlations in the detection events by photons scattered from blue and red pump pulses can be seen, of which

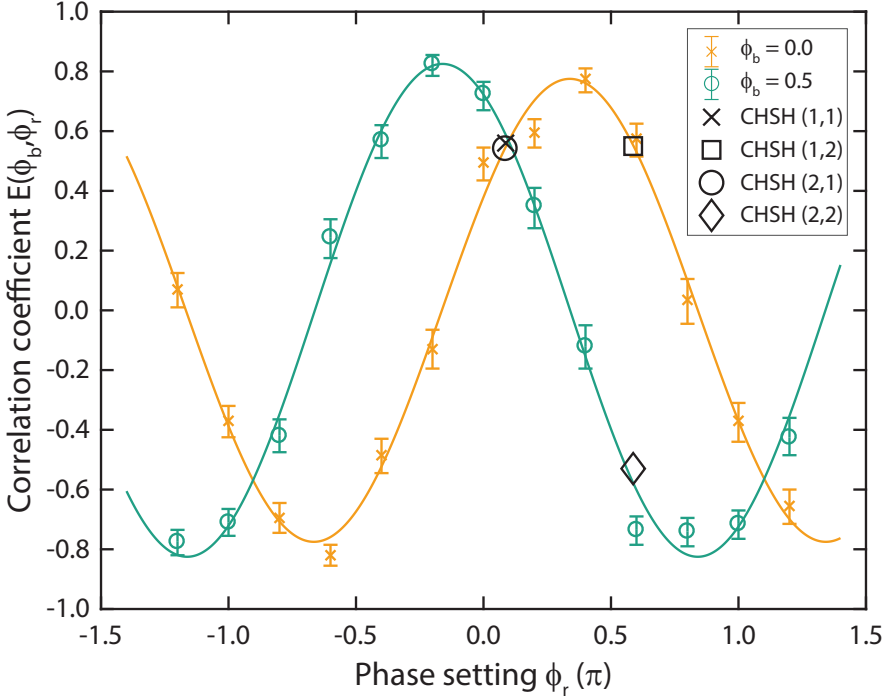


Figure 6.2: Correlation coefficients for various phase settings. We set the blue phase parameter ϕ_b to 0 (orange) and 0.5π (green), while we scan the red pulse's phase setting ϕ_r over more than 2π . The optimal angles to test the CHSH inequality are shown with different symbols. The associated measured values can be found in Table 6.1.

the latter are a coherent mapping of the mechanical state of the resonator. This sweep demonstrates that we are able to independently shift the phases for the Stokes and anti-Stokes states. The visibility $V = 80.0 \pm 2.5\%$ we obtain from fitting the data matches the prediction from the individual cross-correlation measurements very well. The interference furthermore shows the expected periodicity of 2π .

To test possible local hidden-variable descriptions of our correlation measurements we use the CHSH-inequality [4], a Bell-type inequality. Using the correlation coefficients $E(\phi_b, \phi_r)$, it is defined as

$$S = |E(\phi_b^1, \phi_r^1) + E(\phi_b^1, \phi_r^2) + E(\phi_b^2, \phi_r^1) - E(\phi_b^2, \phi_r^2)| \leq 2. \quad (6.5)$$

A violation of this bound allows us to exclude a potential local realistic theory from describing the optomechanical state that we generate in our setup. The maximal violation $S_{QM} = 2\sqrt{2} \cdot V$ is expected for settings $\phi_b^i = [0, \pi/2]$ and $\phi_r^j = [-\pi/4 + \phi_c, \pi/4 + \phi_c]$, with $i, j = 1, 2$ [40]. Here $\phi_c = 0.337\pi$ is an arbitrary, fixed phase offset that is inherent to the setup. Our experimentally achieved visibility exceeds the minimal requirement for a violation of the classical bound $V \geq 1/\sqrt{2} \approx 70.7\%$. We proceed to directly measure

Settings i, j	$\phi_b^i [\pi]$	$\phi_r^j [\pi]$	$E(\phi_b, \phi_r)$
(1,1)	0.0	0.087	$0.561_{-0.020}^{+0.019}$
(1,2)	0.0	0.587	$0.550_{-0.022}^{+0.020}$
(2,1)	0.5	0.087	$0.542_{-0.021}^{+0.018}$
(2,2)	0.5	0.587	$-0.523_{-0.021}^{+0.021}$

Table 6.1: Correlation coefficients for the optimal CHSH angles. The violation of the inequality can be computed according to Eq. (6.5) and results in a S value of $S = 2.174_{-0.042}^{+0.041}$, corresponding to a violation of the classical bound by more than 4 standard deviations.

the correlation coefficients in the four settings, as indicated in Figure 6.2, and obtain $S = 2.174_{-0.042}^{+0.041}$ (cf. Table 6.1). This corresponds to a violation of the CHSH inequality by more than 4 standard deviations, clearly confirming the non-classical character of our state. From the observed visibility of $V = 80.0\%$, we would expect a slightly stronger violation with $S \approx 2.26$. The reduction in our experimentally obtained value for S can be attributed to imperfect filtering of drive photons in front of one of the SNPSDs, which gives rise to varying amounts of leak photons at different phase settings (see discussion in SI).

For quantum network applications it is also important to analyze the quality of the detected optomechanical entanglement with regard to the detection rate. In our measurements we can achieve this by changing the energies of the drive beams to alter the optomechanical interaction strengths. An increase in the blue pulse energy is accompanied by two mechanisms that decrease the state fidelity. Firstly, the probability for higher order scattering events $\mathcal{O}(p_{A,B}^2)$ is increased. Secondly, higher pulse energies also result in more absorption, degrading the state through thermal excitations. As observed in previous experiments [31, 38], optical pumping of the devices creates a thermal population of the mechanical modes with timescales on the order of several hundreds of nanoseconds (see also SI). While we keep the delay to the readout pulse short ($\Delta\tau = 200$ ns), we cannot fully avoid these spurious heating effects. Hence the decrease in visibility with increased pulse energy, as seen in Figure 6.3(a), can be attributed mostly to this direct absorption heating. To further test the heating dynamics of our state, we also sweep the red pulse energies while keeping the excitation energy fixed at the value used in the main experiment ($p_b = 0.8\%$ and 1%). As expected, the increased readout pulse energies lead to substantial heating of the devices [27]. However, even for relatively large optical powers corresponding to $\sim 14\%$ read out efficiency, the correlation coefficient is above the threshold for violating a Bell inequality under the fair sampling assumption, see Figure 6.3(b).

Our system is fully engineered and hence we have complete control over the resonance frequencies and possibilities to integrate with other systems. While in our current structures we intentionally cap the mechanical quality factors to keep the measurement time short [41], recent experiments with very similar devices have observed lifetimes larger than 1 s [42]. Long lived non-classical states of large masses are interesting for fun-

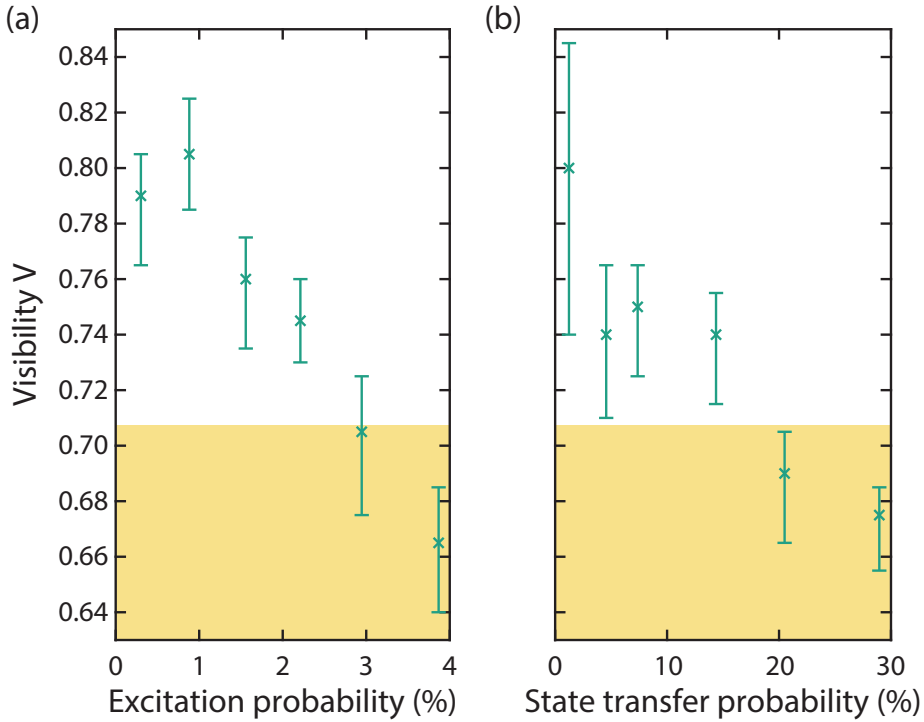


Figure 6.3: Visibility as a function of generation rate and state transfer probability. We sweep the power of the blue pulse while keeping the red state transfer probability fixed, inducing absorption of the optical field in the silicon structure, and see that for excitation probabilities up to around 3% the measured visibility exceeds the threshold to violate the CHSH inequality (left). When increasing only the red pump power (right) a similar behavior can be observed, allowing us to increase the state transfer probability beyond 14%, while still being able to overcome the classical bound (orange shaded region). The visibilities $V = |E(\phi_b, \phi_r)|_{\max}$ are measured in a single phase setting at the optimal angles $\phi_b = 0$ and $\phi_r = 0.337\pi$.

damental studies of quantum mechanics. Combined with the fact that we can efficiently couple these states to photons in the telecom band could enable interesting experiments with Bell tests at remote locations. Employing fast optical switches that route one of the photons to a second set of detectors would furthermore allow us to close the locality loophole in the future. Our probabilistic scheme could, in principle, also be adapted to perform a 'loophole-free' Bell test [13], if in addition the detection loophole would be closed through a more efficient read-out.

In summary, we have demonstrated the violation of a Bell-type inequality using massive (around 10^{10} atoms), macroscopic optomechanical devices, thereby verifying the non-classicality of their state without the need for a quantum description of our experiment. The experimental scheme demonstrated here may also be employed in other, even more massive optomechanical systems. One outstanding challenge is to generate states of genuine macroscopic distinction, for example a macroscopic separation in the center of mass, to investigate fundamental decoherence mechanisms [43] or even the

interplay between quantum physics and gravity [44, 45]. We also show that the created entangled states are relatively robust to absorption heating, which could lead to a realistic implementation of entanglement generation for a future quantum network using optomechanical devices. Violation of a CHSH inequality can also be used to verify long-distance quantum communication with device-independent security using mechanical systems.

ACKNOWLEDGMENTS

We would like to thank Vikas Anant, Nicolas Sangouard, and Joshua Slater for valuable discussions and support. We also acknowledge assistance from the Kavli Nanolab Delft, in particular from Marc Zuiddam and Charles de Boer. This project was supported by the Foundation for Fundamental Research on Matter (FOM) Projectruimte grants (15PR3210, 16PR1054), the European Research Council (ERC StG Strong-Q, ERC CoG QLev4G), the European Commission under the Marie Curie Horizon 2020 initial training programme OMT (grant 722923), the Vienna Science and Technology Fund WWTF (ICT12-049), the Austrian Science Fund (FWF) under projects F40 (SFB FOQUS) and P28172, and by the Netherlands Organisation for Scientific Research (NWO/OCW), as part of the Frontiers of Nanoscience program, as well as through a Vidi grant (680-47-541/994). R.R. is supported by the FWF under project W1210 (CoQuS) and is a recipient of a DOC fellowship of the Austrian Academy of Sciences at the University of Vienna.

6.2. SUPPLEMENTARY INFORMATION

EXPERIMENTAL SETUP

A sketch of the fiber-based setup used in the main text is shown in Figure 6.4. The pulse generation consists of two tunable diode lasers (Santec TSL550 and Toptica CTL1550), which are stabilized at the sidebands of device B using a wavelength meter. We suppress high frequency noise on both laser through optical filtering (linewidth ~ 50 MHz), before we generate the drive pulses using acousto-optic modulators (pulse length ~ 40 ns). The interferometer is formed by a variable ratio coupler and a calibrated 50:50 coupler (deviation below 3%). The interferometer has a free spectral range of 1.2 GHz and is phase-stabilized with a home built fiber stretcher. The EOM is used to select a desired phase on a fast timescale and simultaneously to compensate the frequency mismatch of the mechanical devices of $\Delta\nu_m = 2.3$ MHz. This mismatch is small enough to be compensated by a linear phase sweep during the pulses without the need of a serrrodyne drive.

In order to achieve high efficiencies in our detection paths we use a home-built freespace filtering setup. Each filter line consists of two linear cavities which are actively stabilized to the resonance of the devices. The total detection efficiency for optomechanically scattered photons from device A is 3.4% for detector 1 and 2.9% for detector 2. The efficiency for device B is 2.9% for detector 1 and 2.3% for detector 2. The total loss budget consists of various contributions: photons that are created in one of the optomechanical cavities are transferred to an on-chip silicon waveguide with efficiencies of 65% and 55% for devices A and B, respectively. The transmission from the waveguide to the output of the circulator (59% and 55%) is dominated by waveguide to fiber coupling losses. The rest of the losses are due to a finite transmission through filters, optical components

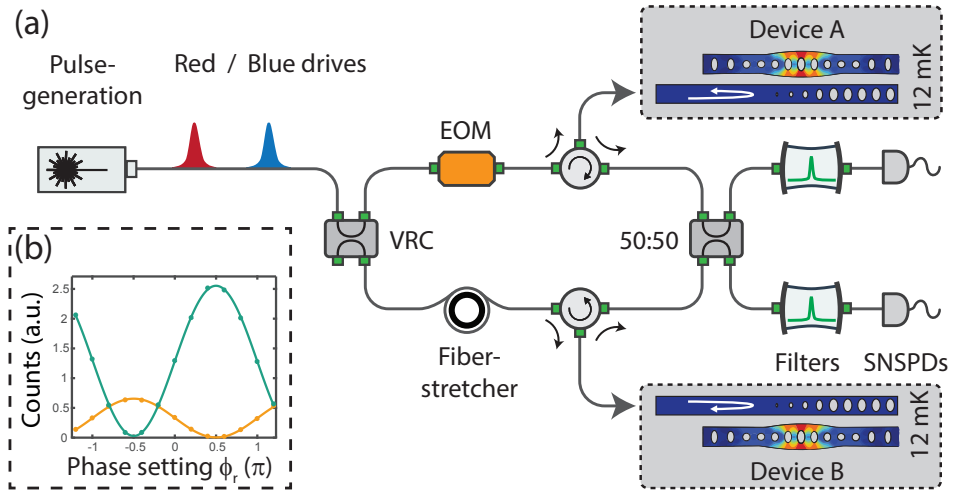


Figure 6.4: (a) Sketch of the setup. We first generate blue and red pulses that drive the optomechanical interactions. The devices are each placed in one arm of a fiber interferometer realized between a variable ratio coupler (VRC) and a 50:50 beamsplitter. We stabilize the overall phase with a fiber stretcher such that we can select particular phase settings with our EOM in arm A. The optomechanically generated photons are filtered from the drive pulses before finally being detected on single-photon superconducting nanowire detectors (SNSPDs). (b) Interferometer visibility. We detune the filter locking point from the device resonance such that we are only sensitive to pump photons that leak through the filters. Here we plot the rate of pump photons detected with detector 1 (orange) and detector 2 (green) as a function of phase difference of the interferometer arms. We observe the expected 2π periodicity with an interference visibility of 98.4%. The difference in amplitude stems from different degrees of suppression of pump photons through the two filter lines.

needed for feeding continuous locking light and finite detection efficiency of SNSPDs.

In order to evaluate the quality of our interferometer we record the first order interference of our lasers. For this, we detune the filters by ~ 2 GHz from the optomechanically scattered photons, such that we are only sensitive to leaked pump photons. We then lock the interferometer with the fiber stretcher and sweep the phase using the EOM as we do for the visibility sweep in Figure 6.1. The visibility we obtain of 98.4% matches well with the independently measured short term fluctuations of the interferometer lock of around $\sim \pi/25$ [46]. The main cause of these fluctuations is noise that is picked up by the fibers inside the dilution refrigerator stemming from the pulse tube cryo cooler.

PUMP FILTERING AND FALSE COINCIDENCES

To estimate the effect of erroneous coincidence clicks that do not stem from the optomechanical state, we perform calibration measurements to estimate the role of leaked drive photons. To do this, we slightly detune the filters away from the frequency of the optomechanically scattered photons, such that they are reflected from the filters and do not reach the SNSPDs. We find that during the main experiments around 17% of red counts detected on detector 2 are in fact imperfectly filtered drive photons. For detector 1 this number is around 7%. To understand this asymmetry, we note that the cavities

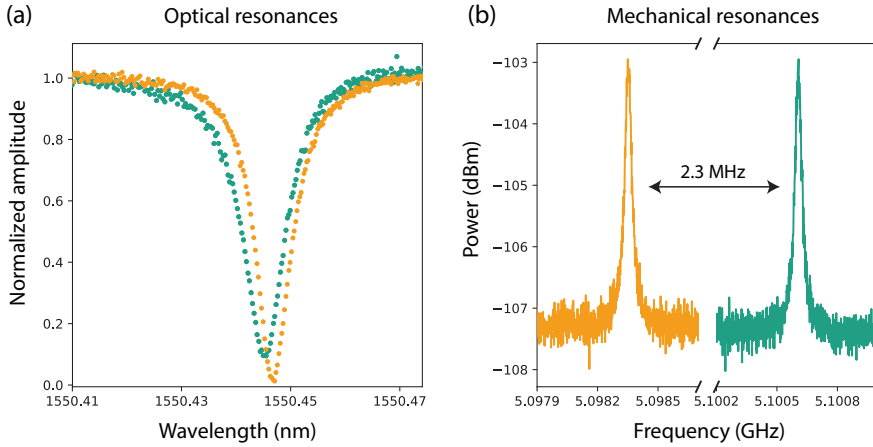


Figure 6.5: Spectroscopy of optomechanical devices A (green) and B (orange). Left: Optical cavity reflection spectrum of the cavities. Right: Mechanical resonances of the two devices.

in front of detector 1 both have linewidths of ~ 35 MHz, while the ones in front of detector 2 have a slightly larger linewidth of ~ 45 MHz. We estimate that perfect filtering would enable us to obtain roughly 12% higher cross correlation values for the individual devices. Similarly, we measure that less than 2% of the detected photons during the blue pulses are leak photons.

The asymmetry in pump suppression has additional consequences for the experiments in which we drive the devices simultaneously. The total rate of leak photons varies with the selected phase setting ϕ_r . The angular dependency is proportional to the sum of the two curves in inset (b) of Figure 6.4. These unwanted photons result in additional coincidences in the second order interference of the main experiment, hence they distort the visibility sweeps of Figure 6.2. The purely sinusoidal fits are not capturing this accurately and therefore mostly serve as a guide to the eye. The values of the correlation coefficients $E(\phi_b, \phi_r)$ in Table 6.1 are affected in the same way. We measure at angles $\phi_r = 0.087\pi$ and 0.587π , of which the latter suffers more from the imperfectly filtered drive pulses. This is the main reason of why we observe a reduction in the Bell parameter S compared to the expected results from the visibility V in figure 6.2 alone. Dark counts on the other hand are low enough (around 15 Hz) to only contribute by less than 1% to the detection events.

DEVICE FABRICATION AND CHARACTERIZATION

The optomechanical devices are fabricated from silicon-on-insulator wafers with a device film thickness of 250 nm as described in [27]. In order to reliably find identical devices on distinct chips, we optimized the electron-beam doses throughout the lithography step, which allowed us to obtain a distribution of only 1 nm of the optical resonances. To further reduce the variability between different chips, we first fabricate a single large chip, fully process it, and then cleave it into smaller pieces as a last step. This optimized procedure results in two chips with excellent overlap of the optical reso-

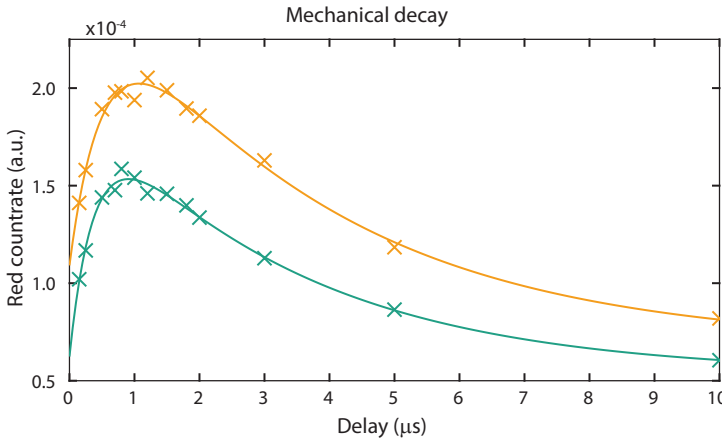


Figure 6.6: Absorption heating and mechanical decay. Heating dynamics of device A (green) and device B (orange) from a pump-probe experiment are plotted. We excite the devices with a blue pulse and read out the mechanical state after a variable delay $\Delta\tau$. Thermal phonons due to absorption of the blue drive occupy the mode on a timescale of several hundreds of nanoseconds, after which the excitations decay to the cold environment with the mechanical lifetimes.

6

nances. Unlike in previous experiments [31], our fabrication method allowed us to perform the experiments without the need for serrodyne shifting of the photon frequencies in one of the arms of the interferometer but rather only apply a small linear ramp signal to the red and blue pulses using the EOM in arm A.

We characterize the optical resonances by sweeping a continuous-wave part of our laser and recording the reflected intensity resonances (cf. Figure 6.5(a)). As we use reflectors at the end of our waveguides (see Figure 6.1), we effectively couple in a single sided way to our devices and therefore expect to see resonances as dips in the reflected light. The measurements of the mechanical resonances are performed by locking the laser to the blue sideband of the optical resonances, amplifying the reflected light in a fiber amplifier and then detecting the optomechanically generated sideband on a fast photodiode (Figure 6.5(b)).

To evaluate the absorption heating dynamics, we perform a pump-probe experiment with the individual devices. Here we excite the devices with a blue and probe with a red drive pulse after a variable delay $\Delta\tau$, see Figure 6.6. The pulse energies are chosen similarly to the ones in the main text. As already observed in previous work [27, 31, 38], the devices see absorption caused heating with a rise time of several hundreds of nanoseconds. The highest temperature is reached in both cases at a delay of around 1 μs , after which the devices decay with their intrinsic quality factors. We fit the excitation dynamics $d_i(\Delta\tau)$ of the two devices ($i = A, B$) with a phenomenologically motivated double exponential model of the form $d_i(\Delta\tau) = a_i e^{-\Delta\tau/\tau_i} - b_i e^{-\Delta\tau/\eta_i} + n_{\text{init},i}$ [31]. We can extract the energy lifetimes of our devices as $\tau_A = 3.3 \pm 0.5 \mu\text{s}$ and $\tau_B = 3.6 \pm 0.7 \mu\text{s}$. Note that the final decay level $n_{\text{init},i}$ does not represent the true base temperature, as we still observe counts from the intra-pulse heating. Nevertheless, we can bound the occupancy $n_{\text{init},i}$

CHSH setting	Trials	Heralding clicks	n_{00}	n_{01}	n_{10}	n_{11}
(1,1)	597302527	645858	708	194	175	611
(1,2)	500363903	546488	606	162	164	521
(2,1)	622224596	680260	752	212	185	589
(2,2)	540137661	592728	170	586	590	198

Table 6.2: Recorded coincidence clicks of the main experiment. Individual trials are performed every 50 μs . Heraldng clicks are the detected photons scattered by the blue pulse. Coincidences $n_{i,j}$ are clicks that were registered after getting a heralding event in the same trial, with i, j indicating the detector for the blue and red scattered photons.

from above using the asymmetry in the click rates of blue and red sideband scattered photons $C_{b,i}$ and $C_{r,i}$ as $n_{\text{init},i} = C_{r,i} / (C_{b,i} - C_{r,i})$ [38]. We perform the measurements for blue and red pulses individually with a duty cycle of 50 μs each. For device A, we determine the initial occupation to be ~ 0.07 phonons if measured on detector 1 and ~ 0.09 phonons if measured on detector 2. Device B has similar apparent occupations of ~ 0.06 phonons on detector 1 and ~ 0.09 phonons if measured on detector 2. The difference in the measurements on the two detectors reflects the different amount of leak suppression as discussed above. However, both measurements also contain the intrapulse heating detection events, meaning we expect the real occupancy in the dark to be below these extracted numbers.

STATISTICAL ANALYSIS

The statistical analysis for the CHSH inequality is done using the same techniques as Ref. [31]. We apply binominal statistics on the number of coincidence events n_{ij} in Equation (6.4) and generate discrete probability distributions. We then treat the correlation coefficients E as non-trivial functions of two random variables ($n_{\text{same}} = n_{11} + n_{22}$ and $n_{\text{diff}} = n_{12} + n_{21}$) and numerically find their probability distributions via the cumulative density function method. We calculate the probability distribution for the Bell parameter S as a convolution of the probability distributions of the four correlation coefficients. Finally we calculate the expectation value and error bounds ($\pm 34\%$ confidence interval) by numerical integration of the resulting probability density function.

The data for the main experiment was acquired in with approx. 500–620 million trials per CHSH setting. Together with the duty time of 50 μs , this amounts to pure measurement times of 7.0 – 8.6 hours per setting, or ~ 31 hours in total. This time is excluding additional overhead that is needed to re-lock the filters or manage the acquired data. The total actual measurement time is about a factor of two larger. The data was taken in intervals of 20 minutes and the CHSH settings were cycled after each interval. During the experiment, a total of 6423 photon pairs were detected, which amounts to roughly 210 successful trials per pure measurement hour.

REFERENCES

- [1] J. S. Bell, *On the Einstein Podolsky Rosen Paradox*, Physics 1, 195 (1964).

- [2] A. Einstein, B. Podolsky, and N. Rosen, *Can Quantum-Mechanical Description of Physical Reality Be Considered Complete?* Phys. Rev. **47**, 777 (1935).
- [3] N. Bohr, *Can quantum-mechanical description of physical reality be considered complete?* Phys. Rev. **48**, 696 (1935).
- [4] J. F. Clauser, M. A. Horne, A. Shimony, and R. A. Holt, *Proposed experiment to test local hidden-variable theories*, Phys. Rev. Lett. **23**, 880 (1969).
- [5] S. J. Freedman and J. F. Clauser, *Experimental test of local hidden-variable theories*, Phys. Rev. Lett. **28**, 938 (1972).
- [6] A. Aspect, P. Grangier, and G. Roger, *Experimental tests of realistic local theories via Bell's theorem*, Phys. Rev. Lett. **47**, 460 (1981).
- [7] Y. H. Shih and C. O. Alley, *New Type of Einstein-Podolsky-Rosen-Bohm Experiment Using Pairs of Light Quanta Produced by Optical Parametric Down Conversion*, Phys. Rev. Lett. **61**, 2921 (1988).
- [8] J. G. Rarity and P. R. Tapster, *Experimental violation of Bells inequality based on phase and momentum*, Phys. Rev. Lett. **64**, 2495 (1990).
- [9] P. G. Kwiat, K. Mattle, H. Weinfurter, A. Zeilinger, A. V. Sergienko, and Y. Shih, *New high-intensity source of polarization-entangled photon pairs*, Phys. Rev. Lett. **75**, 4337 (1995).
- [10] G. Weihs, T. Jennewein, C. Simon, H. Weinfurter, and A. Zeilinger, *Violation of Bell's inequality under strict Einstein locality conditions*, Phys. Rev. Lett. **81**, 5039 (1998).
- [11] M. A. Rowe, D. Kielpinski, V. Meyer, C. A. Sackett, W. M. Itan, C. Monroe, and D. J. Wineland, *Experimental violation of a Bell's inequality with efficient detection*, Nature **409**, 791 (2001).
- [12] B. Hensen, H. Bernien, A. E. Dréau, A. Reiserer, N. Kalb, M. S. Blok, J. Ruitenberg, R. F. L. Vermeulen, R. N. Schouten, C. Abellán, W. Amaya, V. Pruneri, M. W. Mitchell, M. Markham, D. J. Twitchen, D. Elkouss, S. Wehner, T. H. Taminiau, and R. Hanson, *Loophole-free Bell inequality violation using electron spins separated by 1.3 kilometres*, Nature **526**, 682 (2015).
- [13] M. Giustina, M. A. M. Versteegh, S. Wengerowsky, J. Handsteiner, A. Hochrainer, K. Phelan, F. Steinlechner, J. Kofler, J.-A. Larsson, C. Abellán, W. Amaya, V. Pruneri, M. W. Mitchell, J. Beyer, T. Gerrits, A. E. Lita, L. K. Shalm, S. W. Nam, T. Scheidl, R. Ursin, B. Wittmann, and A. Zeilinger, *Significant-Loophole-Free Test of Bell's Theorem with Entangled Photons*, Phys. Rev. Lett. **115**, 250401 (2015).
- [14] L. K. Shalm, E. Meyer-Scott, B. G. Christensen, P. Bierhorst, M. A. Wayne, M. J. Stevens, T. Gerrits, S. Glancy, D. R. Hamel, M. S. Allman, K. J. Coakley, S. D. Dyer, C. Hodge, A. E. Lita, V. B. Verma, C. Lambrocco, E. Tortorici, A. L. Migdall, Y. Zhang, D. R. Kumor, W. H. Farr, F. Marsili, M. D. Shaw, J. A. Stern, C. Abellán, W. Amaya, V. Pruneri, T. Jennewein, M. W. Mitchell, P. G. Kwiat, J. C. Bienfang, R. P. Mirin,

- E. Knill, and S. W. Nam, *Strong loophole-free test of local realism*, Phys. Rev. Lett. **115**, 250402 (2015).
- [15] W. Rosenfeld, D. Burchardt, R. Garthoff, K. Redeker, N. Ortegel, M. Rau, and H. Weinfurter, *Event-Ready Bell Test Using Entangled Atoms Simultaneously Closing Detection and Locality Loopholes*, Phys. Rev. Lett. **119**, 010402 (2017).
- [16] J. T. Barreiro, J.-D. Bancal, P. Schindler, D. Nigg, M. Hennrich, T. Monz, N. Gisin, and R. Blatt, *Demonstration of genuine multipartite entanglement with device-independent witnesses*, Nature Phys. **9**, 559 (2013).
- [17] R. Schmied, J.-D. Bancal, B. Allard, M. Fadel, V. Scarani, P. Treutlein, and N. Sangouard, *Bell correlations in a Bose-Einstein condensate*, Science **352**, 441 (2016).
- [18] M. Ansmann, H. Wang, R. C. Bialczak, M. Hofheinz, E. Lucero, M. Neeley, A. D. O'Connell, D. Sank, M. Weides, J. Wenner, A. N. Cleland, and J. M. Martinis, *Violation of Bell's inequality in Josephson phase qubits*, Nature **461**, 504 (2009).
- [19] S. Pironio, A. Acín, S. Massar, A. B. de la Giroday, D. N. Matsukevich, P. Maunz, S. Olmschenk, D. Hayes, L. Luo, T. A. Manning, and C. Monroe, *Random numbers certified by Bells theorem*, Nature **464**, 1021 (2010).
- [20] P. Bierhorst, E. Knill, S. Glancy, Y. Zhang, A. Mink, S. Jordan, A. Rommal, Y.-K. Liu, B. Christensen, S. W. Nam, M. J. Stevens, and L. K. Shalm, *Experimentally generated randomness certified by the impossibility of superluminal signals*, Nature **556**, 223 (2018).
- [21] A. Acín, N. Brunner, N. Gisin, S. Massar, S. Pironio, and V. Scarani, *Device-independent security of quantum cryptography against collective attacks*, Phys. Rev. Lett. **98**, 230501 (2007).
- [22] P. Sekatski, J.-D. Bancal, S. Wagner, and N. Sangouard, *Certifying the building blocks of quantum computers from Bell's theorem*, arXiv:1802.02170 (2018).
- [23] E. Schrödinger, *Die gegenwärtige Situation in der Quantenmechanik*, Die Naturwissenschaften **48**, 807 (1935).
- [24] E. E. Wollman, C. U. Lei, A. J. Weinstein, J. Suh, A. Kronwald, F. Marquardt, A. A. Clerk, and K. C. Schwab, *Quantum squeezing of motion in a mechanical resonator*, Science **349**, 952 (2015).
- [25] A. D. O'Connell, M. Hofheinz, M. Ansmann, R. C. Bialczak, M. Lenander, E. Lucero, M. Neeley, D. Sank, H. Wang, M. Weides, J. Wenner, J. M. Martinis, and A. N. Cleland, *Quantum ground state and single-phonon control of a mechanical resonator*, Nature **464**, 697 (2010).
- [26] Y. Chu, P. Kharel, W. H. Renninger, L. D. Burkhardt, L. Frunzio, P. T. Rakich, and R. J. Schoelkopf, *Quantum acoustics with superconducting qubits*, Science **358**, 199 (2017).

- [27] S. Hong, R. Riedinger, I. Marinković, A. Wallucks, S. G. Hofer, R. A. Norte, M. Aspelmeyer, and S. Gröblacher, *Hanbury Brown and Twiss interferometry of single phonons from an optomechanical resonator*, *Science* **358**, 203 (2017).
- [28] A. P. Reed, K. H. Mayer, J. D. Teufel, L. D. Burkhardt, W. Pfaff, M. Reagor, L. Sletten, X. Ma, R. J. Schoelkopf, E. Knill, and K. W. Lehnert, *Faithful conversion of propagating quantum information to mechanical motion*, *Nature Phys.* **13**, 1163 (2017).
- [29] T. Palomaki, J. Teufel, R. Simmonds, and K. Lehnert, *Entangling mechanical motion with microwave fields*, *Science* **342**, 710 (2013).
- [30] K. C. Lee, M. R. Sprague, B. J. Sussman, J. Nunn, N. K. Langford, X.-M. Jin, T. Champion, P. Michelberger, K. F. Reim, D. England, D. Jaksch, and I. Walmsley, *Entangling macroscopic diamonds at room temperature*. *Science* **334**, 1253 (2011).
- [31] R. Riedinger, A. Wallucks, I. Marinković, C. Löschnauer, M. Aspelmeyer, S. Hong, and S. Gröblacher, *Remote quantum entanglement between two micromechanical oscillators*, *Nature* **556**, 473 (2018).
- [32] C. F. Ockeloen-Korppi, E. Damskägg, J.-M. Pirkkalainen, M. Asjad, A. A. Clerk, F. Massel, M. J. Woolley, and M. A. Sillanpää, *Stabilized entanglement of massive mechanical oscillators*, *Nature* **556**, 478 (2018).
- [33] S. J. van Enk, N. Lütkenhaus, and H. J. Kimble, *Experimental procedures for entanglement verification*, *Phys. Rev. A* **75**, 052318 (2007).
- [34] V. C. Vivoli, T. Barnea, C. Galland, and N. Sangouard, *Proposal for an Optomechanical Bell Test*, *Phys. Rev. Lett.* **116**, 070405 (2016).
- [35] S. G. Hofer, K. W. Lehnert, and K. Hammerer, *Proposal to Test Bells Inequality in Electromechanics*, *Phys. Rev. Lett.* **116**, 070406 (2016).
- [36] J. Chan, A. H. Safavi-Naeini, J. T. Hill, S. Meenehan, and O. Painter, *Optimized optomechanical crystal cavity with acoustic radiation shield*, *App. Phys. Lett.* **101**, 081115 (2012).
- [37] M. A. Horne, A. Shimony, and A. Zeilinger, *Two-particle interferometry*, *Phys. Rev. Lett.* **62**, 2209 (1989).
- [38] R. Riedinger, S. Hong, R. A. Norte, J. A. Slater, J. Shang, A. G. Krause, V. Anant, M. Aspelmeyer, and S. Gröblacher, *Non-classical correlations between single photons and phonons from a mechanical oscillator*, *Nature* **530**, 313 (2016).
- [39] H. de Riedmatten, J. Laurat, C. W. Chou, E. W. Schomburg, D. Felinto, and H. J. Kimble, *Direct measurement of decoherence for entanglement between a photon and stored atomic excitation*, *Phys. Rev. Lett.* **97**, 113603 (2006).
- [40] B. S. Cirel'son, *Quantum generalizations of Bell's inequality*, *Lett. Math. Phys.* **4**, 93 (1980).

- [41] R. N. Patel, C. J. Sarabalis, W. Jiang, J. T. Hill, and A. H. Safavi-Naeini, *Engineering phonon leakage in nanomechanical resonators*, Phys. Rev. Applied **8**, 041001 (2017).
- [42] G. MacCabe, H. Ren, J. Luo, J. Cohen, H. Zhou, A. Ardizzi, and O. Painter, *Optomechanical measurements of ultra-long-lived microwave phonon modes in a phononic bandgap cavity*, (APS March Meeting, 2018).
- [43] A. Bassi, K. Lochan, S. Satin, T. P. Singh, and H. Ulbricht, *Models of wave-function collapse, underlying theories, and experimental tests*, Rev. Mod. Phys. **85**, 471 (2013).
- [44] S. Bose, A. Mazumdar, G. W. Morley, H. Ulbricht, M. Toroš, M. Paternostro, A. A. Geraci, P. F. Barker, M. S. Kim, and G. Milburn, *Spin entanglement witness for quantum gravity*, Phys. Rev. Lett. **119**, 240401 (2017).
- [45] C. Marletto and V. Vedral, *Gravitationally induced entanglement between two massive particles is sufficient evidence of quantum effects in gravity*, Phys. Rev. Lett. **119**, 240402 (2017).
- [46] J. Minář, H. de Riedmatten, C. Simon, H. Zbinden, and N. Gisin, *Phase-noise measurements in long-fiber interferometers for quantum-repeater applications*, Phys. Rev. A **77**, 052325 (2008).

7

CONCLUSION

In this chapter, I will discuss what challenges have to be solved in order to enable further progress of optomechanical crystal devices.

There are several ways integrated optomechanical structures with GHz frequency can have an impact of quantum technologies. We have shown in our work that it is possible to convert mechanical excitations with frequencies around 5 GHz to optical excitation at 190 THz, while preserving the non-classicality. This is an important step towards microwave-optical transducers. Still with devices presented in this thesis low conversion efficiency between optics and mechanics was attained. The main limitation is due to optical absorption that limits the amount of pump power that can be used for readout, without heating up device substantially.

Other application would be quantum repeaters based on nanobeams. Important step has been already demonstrate by generating entanglement between nanobeams on different chips using telecom wavelength[1]. Same as previous example quantum networks based on nanobeam are currently prohibited by absorption. We see from two applications presented that the next main step for gigahertz optomechanical crystals will be to demonstrate high conversion efficiency between phonons and optical photons without added thermal noise, by reducing optical absorption or its effects on mechanical state. I will briefly outline a few possible directions that could improve current performance.

If one wishes to keep the OMC nanobeam geometry some of the options would be following. One can experiment with different materials and their surface terminations. Once photons are absorbed in silicon, electron-hole pairs are generated. Potentially these can be collected in solar cell fashion before energy is lost as heat. Short lifetimes of excited electrons in silicon photonic structures may prohibit this[2].

Improved performance can be expected by optimizing pulse sequence. This has not been addressed in this thesis. Shorter pulses might enable lower number of thermal photons for same readout efficiency. Still this will not prevent delayed heating from a laser pulse.

Because of their one dimensional nature, nanobeams have a bad thermal connection

with the rest of the chip. Therefore once heat is generated inside nanobeam it takes a while for it to leak into the substrate. During this time it can start populating nanobeam breathing mode, which we wish to avoid. A natural way to approach this problem is to consider 2d optomechanical resonators and achieve a better thermal connection[3].

Even better thermal properties can be achieved with surface acoustic wave mechanical resonators[4]. Plus those can be efficiently interfaced with microwave signal. The problem is designing an optical cavity having good overlap with mechanical mode. Large mode volume might prevent coupling rates as high as in nanobeam.

Coupling the mechanical resonators to microwave cavities can have more upsides than just wavelength conversion. Potentially microwave cooling the silicon nanobeam would be a way to restart it into the ground state without waiting for a long time for absorption induced phonons to decay. One can also dream of transferring the state of mechanical resonator to microwave resonator temporarily before absorption kicks in.

Although the lifetime of nanobeams can be extremely long, absorption limited the life of quantum excitation in these structures up to a few hundred nanoseconds in our experiments. Preserving optically created excitation inside the nanobeam for much longer time is a necessity. Even the if absorption problem is not solved one can hope to achieve storage of heralded phonon for long time by sacrificing the generation rate. Still, this is probably not helping coming closer to actual applications.

If absorption issue is solved, one can hope for devices that have long lifetime, high readout efficiency, high entanglement generation rate, a possibility for multiplexing. Also, active cooling of the device using red-detuned light would become a possibility of making nanobeams even more attractive for applications.

7 REFERENCES

- [1] R. Riedinger, A. Wallucks, I. Marinković, C. Löschnauer, M. Aspelmeyer, S. Hong, and S. Gröblacher, *Remote quantum entanglement between two micromechanical oscillators*, Nature **556**, 473 (2018).
- [2] W. H. P. Pernice, C. Schuck, M. Li, and H. X. Tang, *Carrier and thermal dynamics of silicon photonic resonators at cryogenic temperatures*, Opt. Express **19**, 3290 (2011).
- [3] A. H. Safavi-Naeini, J. T. Hill, S. Meenehan, J. Chan, S. Gröblacher, and O. Painter, *Two-dimensional phononic-photonic band gap optomechanical crystal cavity*, Phys. Rev. Lett. **112**, 153603 (2014).
- [4] L. Kuhn, M. L. Dakss, P. F. Heidrich, and B. A. Scott, *DEFLECTION OF AN OPTICAL GUIDED WAVE BY a SURFACE ACOUSTIC WAVE*, Applied Physics Letters **17**, 265 (1970).

8

APPENDIX

8.1. FABRICATION FAILURES AND HINTS

In this section I would like to show several figures of fabrication that went wrong and share few fabrications tips.

As mentioned before the RIE ICP etch rate of silicon can drift over a timescale of weeks, so it is smart to check it occasionally. Our etch chemistry does not etch silicon dioxide. Once all silicon is etched away from the top, ions will start etching silicon sideways (Fig. 8.2(b)). Etching SOI with $\text{SF}_6 + \text{C}_4\text{F}_8$ plasma can be solution to this problem, but carbon based passivation used in this process is much harder to remove.

Choosing bad combination of parameters for EBL can lead to disaster (Fig. 8.1(a)). If for technical issues one has to change any of the parameters (beam current or aperture) it is best to do a sweep of a beam step size and dose.

Multipass exposure technique showed to be much more resilient to EBL machine issues. We can simply expose the pattern several times (3-5), with a dose that is roughly that many times smaller. It is important not to change the main field of the EBL. Even when writing within the same main-field, drifts can occur between exposures if the pattern takes a long time to write (Fig. 8.2(a)). Therefore it is best to expose each nanobeam fully with multipass before moving to the next device.

8.2. MEASURING INPUT COUPLING OF PHOTONIC RESONATOR

As described in Chapter 3 in order to determine whether the photonic cavity is under or over-coupled one should perform the measurement that is sensitive to the phase of reflected light[1]. This can be done by using setup showed in Fig. 8.3. We send amplitude modulated light, such that carrier and one sideband are fully off-resonant. That way they can be used as a phase reference. The second sideband is used to probe the resonance. When these three waves are detected on photodiode the detected signal at modulation frequency will depend on amplitude and phase response of the cavity.

Laser light (frequency ω , amplitude A) is weakly amplitude modulated (with fre-

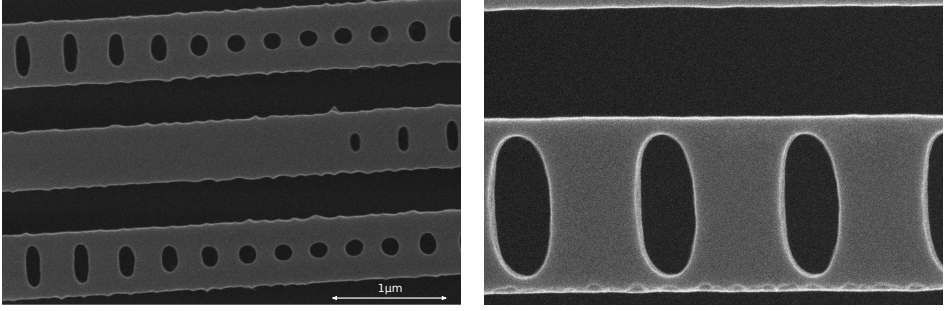


Figure 8.1: SEM image of fully fabricated nanobeams that were exposed with (a) too low and (b) too high EBL dose

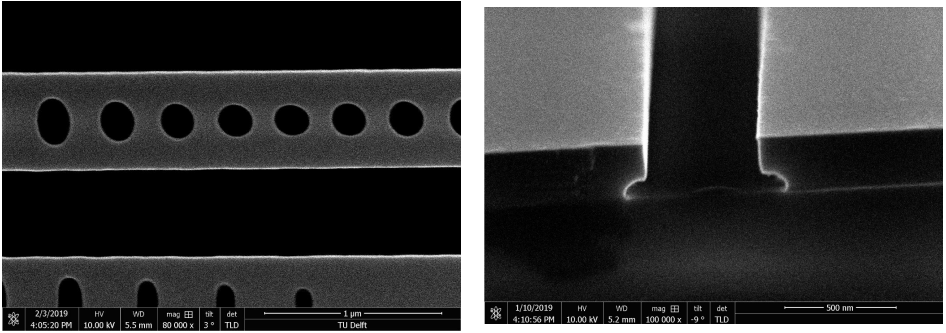


Figure 8.2: (a) Occasionally nanobeams written with multipass technique looked as presented here. On this particular chip we had nanobeams exposed in two different ways: 1. expose single nanobeam multiple times and then go for next one. 2. expose nanobeam once, then few more nanobeams also once and go back for the initial one and repeat process multiple times (all nanobeams were in the same mainfield). Only devices exposed with the second technique had the distortion. This make us believe that this distortion of holes comes from EBL machine drift during time delay between exposure passes in multipass techniques. (b) Cross section SEM of a trench etched in silicon when etching was not stopped on time. Resist has been removed with DMF before taking SEM image.

quency ω_a) using Electro-Optic Modulator (EOM) producing the signal:

$$S = A \cos(\omega t) + a \cos([\omega + \omega_a]t) + a \cos([\omega - \omega_a]t)$$

where a is amplitude of sidebands created by modulation. When reflected from the photonic resonator, the amplitude and phase of one of the sidebands will be changed due to cavity response (Chapter 3):

$$S = A \cos(\omega t) + a \cos((\omega + \omega_a)t) + a\sqrt{R(\omega_a)} \cos((\omega + \omega_a)t + \theta(\omega_a))$$

We detect these waves on photodiode giving the signal V that is proportional to S^2 . Since we are driving the EOMs with VNA and detecting only terms that rotate with ω_a :

$$V = Aa \cos((\omega + \omega_a)t) + Aa\sqrt{R(\omega_a)} \cos((\omega + \omega_a)t + \theta(\omega_a))$$

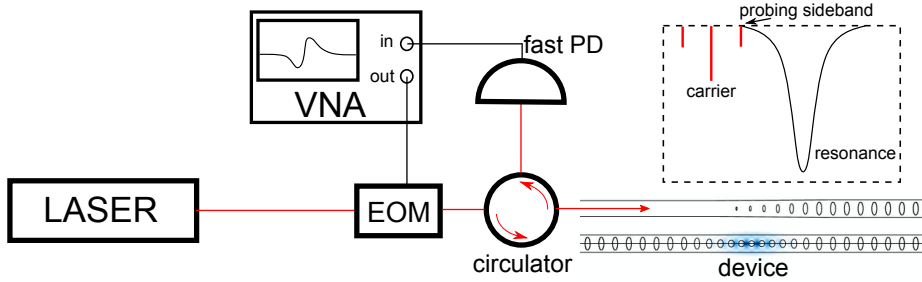


Figure 8.3: Setup for measuring the phase response of the cavity. Light from diode laser(Santec TSL550) is modulated using an amplitude electro optic modulator(ixblue MX-LN-10) and sent through circulator to the photonic cavity. Field reflected from the cavity is sent to fast photodiode(ET-3500AF). Vector Network Analyser (VNA) is used to drive the EOM and detect signal from photodiode. Additionally, polarization controllers should be used for adjusting the polarization coming into the EOM and device. Inset: Carrier and two sidebands (red) are reflected back to photodiode. As we sweep the modulation frequency with VNA the right sideband will probe the spectrum of the optical cavity.

We plot this result in Fig. 8.4. The phase of this signal with respect to signal that modulated EOM can be determined using VNA. We can see that it contains the phase response of the cavity ($\theta(\omega_d)$) but because of the second sideband, two are not equal. Still difference between the minimum and maximum of the phase is a monotonic function of coupling and we can determine whether the cavity is over- or under-coupled.

We can also determine the coupling regime from the amplitude of the detected signal. This can be understood as following. When the cavity is critically couple no light on resonance is reflected, therefore we expect half of the signal when one sideband is on resonance compared to when none of the three tones are on the resonance (all three reflected). As we enter the over-coupled regime cavity shifts the phase such that the probing sideband is the opposite phase than other one, leading to even lower signal. One can look at this as now part of our signal is transformed to phase modulated. Sideband that is probing resonance is smaller because of the amplitude response of the cavity and therefore we still see the signal that comes from amplitude modulation. As we approach the infinitely over-coupled regime, the amplitude of the RF signal goes to 0 at resonance, as two sidebands are out of phase and becoming the same in size. Calibration of VNA can be done by locking laser more than 10 GHz away so that all three waves are reflected. Also this technique assumes that reflection is flat around the resonance, such that all waves are equally reflected when off resonance. Erbium doped fiber amplifier (EDFA) can be used in front of photodiode to increase the signal. Power coming into the cavity should be small enough to avoid thermo-optic effects. At high RF powers higher order sidebands might corrupt the measurement.

Using this phase sensitive measurement technique we can determine the collection efficiency of optical cavity to the waveguide as shown in Fig. 8.5 for a set of devices. If one has ability to sweep the coupling between the waveguide and device, all parameters can be determined without the need for the technique presented here(just from intensity response for various κ_e). But this would rely on the (maybe true) fact that intrinsic quality factor is the same for all devices.

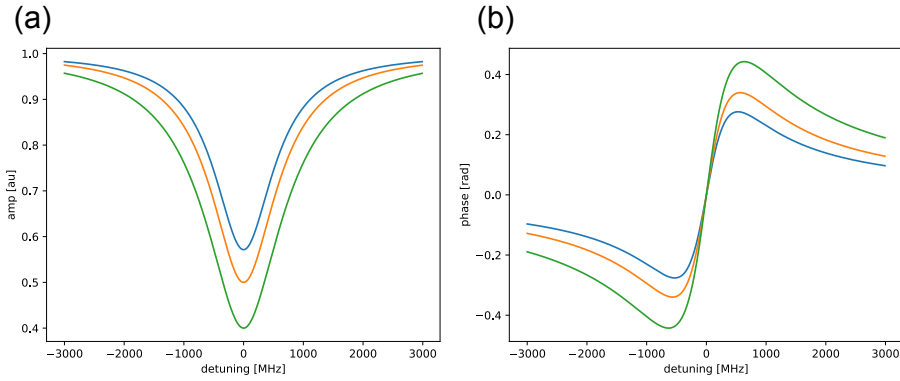


Figure 8.4: (a) Amplitude of the RF signal detected using setup in Fig. 8.3 as a function of the detuning of the probing sideband. Cavity parameters are: intrinsic linewidth $\kappa_0 = 800$ MHz and extrinsic coupling 600 MHz, 800 MHz, 1200 MHz for blue, orange, green line respectively. We can see that depth of resonance keeps increasing with external coupling even above critical coupling regime. (b) Phase of same RF signal, cavity parameters and color coding.

8.3. EFFICIENT FIBER COUPLING INSIDE A DILUTION FRIDGE

Coupling light with HF pulled fiber usually requires an imaging system. Installing microscope inside the fridge is possible but not a straight forward task[3]. Still it is possible to align the tapered fiber to waveguide on the chip inside the dilution fridge without a microscope following the steps given in Fig. 8.6. Alignment is done at $T = 4$ K before the condensing. If mounted under angle, the tapered fiber can be used to address also devices that are not on the edge of the chip. We have demonstrated this with setup that includes microscope but it should work without microscope as well as long as one uses positioning stages with position encoding and know how far from chip edge the devices are. We have measured a single pass efficiency above 0.9 inside dilution fridge. Problem with this way of coupling is that the fiber can occasionally slip of the waveguide even without intentional movement, depending how stable is the setup. We plan to investigate this problem further. The fiber can break if one runs into substrate, but being careful can result in very reliable alignment. Some softer materials can have an issue that the fiber rips off the waveguide. We saw this occasionally happening with gallium arsenide waveguides.

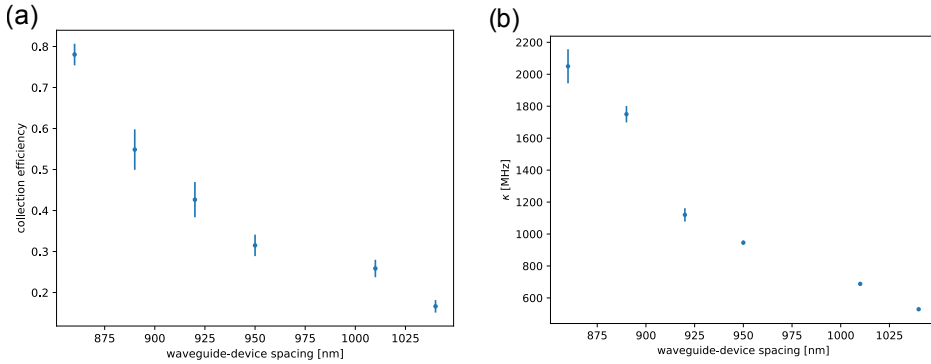


Figure 8.5: (a) Measured collection efficiency on set of devices with different spacing between the waveguide and nanobeam. Waveguide reflector is placed such that there is no offset along the waveguide between reflector holes and nanobeam holes. Tapering of the reflector is done as described in [2]. (b) Total decay rate of same devices.

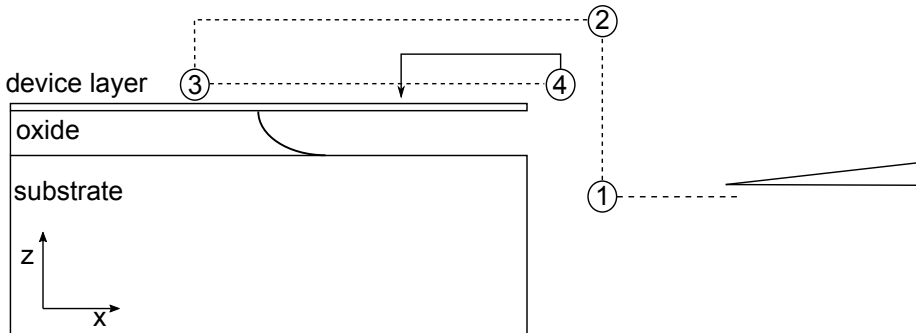


Figure 8.6: Simple procedure for aligning tapered fiber in fridge. Before cooling down one aligns the chip roughly to the substrate such that the reflected light can be detected. At 4K take following steps. 1. Approach the chip. As we do this amount of reflected light increases. The periodicity of interferometer formed by chip and fiber can be used to estimate the distance. 2. After approaching to within $20 \mu\text{m}$, one can move up until reflection is gone and that way find the top surface of chip. 3. Move fiber about $40 \mu\text{m}$ in negative x direction and lower it until small reflection from chip surface is observed. 4. Drag the fiber across the chip surface until reflection gets a sudden change. This enables to determine more precisely the side surface. Steps 3 and 4 can be avoided, specially if there is a lot of chipping due to dicing of chip. Last step is to try to couple to the device, although we have no information where the device is in y direction. Therefore one has to try several times at different locations. It is therefore advisable to have high density of devices on the chip. Some of them can be placed only as markers, cause as soon as one device is located, position of the rest is known.

REFERENCES

- [1] S. Gröblacher, J. T. Hill, A. H. Safavi-Naeini, J. Chan, and O. Painter, *Highly efficient coupling from an optical fiber to a nanoscale silicon optomechanical cavity*, Appl. Phys. Lett., **103**, 181104 (2013).
- [2] S. M. Meenehan, *Cavity Optomechanics at Millikelvin Temperatures*, Ph.D. thesis (2015).
- [3] A. J. R. MacDonald, G. G. Popowich, B. D. Hauer, P. H. Kim, A. Fredrick, X. Rojas, P. Doolin, and J. P. Davis, *Optical microscope and tapered fiber coupling apparatus for a dilution refrigerator*, Review of Scientific Instruments **86**, 013107 (2015).

SUMMARY

This thesis explores the possibility of controlling the quantum states of high frequency mechanical resonators using infra-red laser pulses.

Chapter 1 gives an overview of quantum technologies based on mechanical resonators relevant for this thesis.

Chapter 2 provides the basics of the theoretical background of optomechanics. The Hamiltonian that describes the interaction between the moving mirror and electromagnetic waves will be described. The second part of the chapter will deal with methods borrowed from quantum optics and used to demonstrate non-classical behaviour of a mechanical resonator.

Chapter 3 presents a physical implementation of optomechanics Hamiltonian in form of silicon nanobeam devices. Additional hardware that needs to be integrated with optomechanical devices in order to perform experiments will be described. This includes optical waveguides and fibers used for coupling light into the cavity. We will start the discussion on how effects beyond simple optomechanics model impact these devices.

Chapter 4 describes methods used to microfabricate nanobeam devices on a chip. This chapter aims to give tips and hits toward the successful fabrication of optomechanical devices.

Chapter 5 presents the results of an experiment demonstrating non-classical behaviour of a single optomechanical device. We will use a heralding scheme to prepare the non-classical state of mechanical resonator and use optical detection to confirm its non-classicality.

Chapter 6 describes the measurement of Bell inequality between two optical and two mechanical modes.

Chapter 7 is the conclusion chapter, where I discuss the results of experiments presented, as well the potential directions of future experiments and how control over quantum state of mechanical resonators can be improved.

SAMENVATTING

Dit proefschrift onderzoekt de mogelijkheid om kwantumtoestanden van hoogfrequente mechanische resonatoren te controleren door middel van infrarode laserpulsen.

Hoofdstuk 1 geeft een overzicht van de kwantumtechnologieën gebaseerd op mechanische resonatoren die relevant zijn voor dit proefschrift.

Hoofdstuk 2 geeft de basis van de theoretische achtergrond van de optomechanica. De Hamiltoniaan die de interactie tussen een bewegende spiegel en het elektromagnetisch veld beschrijft, zal worden beschreven. Het tweede deel van dit hoofdstuk gaat over methodes uit het veld van de kwantumoptica die gebruikt worden om niet-klassiek gedrag van een mechanische resonator aan te tonen.

Hoofdstuk 3 bevat de implementatie van de optomechanische Hamiltoniaan voor apparaten gebaseerd op Silicium nanobalken. Extra apparatuur die nodig is om experimenten te doen met optomechanische apparaten, zal worden beschreven. Dit omvat optische golfgeleiders en glasvezels die gebruikt worden om licht naar de optische holte te koppelen. We zullen een begin maken aan de discussie over hoe effecten die verder gaan dan het simpele optomechanische model deze apparaten beïnvloeden.

Hoofdstuk 4 beschrijft methodes die gebruikt worden om nanobalken te maken op een chip. Het doel van dit hoofdstuk is om tips en hits te geven voor de succesvolle fabricage van optomechanische apparaten.

Hoofdstuk 5 bevat de resultaten van een experiment waarin het niet-klassieke gedrag van een enkel optomechanisch apparaat gedemonstreerd wordt. We gebruiken een aankondigingsschema om de niet-klassieke staat van de mechanische resonator te maken, en gebruiken optische detectie om te bevestigen dat de staat niet-klassiek is.

Hoofdstuk 6 beschrijft de meting van de Bell-ongelijkheid tussen twee optische en twee mechanische eigentoestanden.

Hoofdstuk 7 is het concluderende hoofdstuk, waar ik de behaalde resultaten bediscussieer, evenals potentiële richtingen voor toekomstige experimenten en hoe de kwantum controle van mechanische resonatoren verbeterd kan worden.

ACKNOWLEDGEMENTS

This thesis could not be completed without the help of many that I interacted with in the last four years. First I would like to express my gratitude to my advisor Simon Gröblacher for accepting me in this group and creating great research environment from which great results came.

I would like to thank Herre van der Zant for his role of being my second promotor. Many thanks to Yaroslav Blanter, Peter Steeneken, Ewold Verhagen, Andrea Fiore, Nicolas Sangouard for being in my thesis committee.

I would like to greatly acknowledge Andreas Wallucks, with whom I worked closely on research projects during almost 4 years. I am very grateful for having Ralf Riedinger, Sungkun Hong and Markus Aspelmeyer as collaborators on experiments described in this thesis. It was great to be a part of this amazing team.

When I started my PhD I had no clue about microfabrication, so I would like acknowledge Richard Norte for sharing his knowledge and training me in the cleanroom. My cleanroom skills further developed thanks to interaction with Moritz Forsch and Claus Gärtner, new cleanroom gurus.

My knowledge in computational electromagnetism greatly benefited from interaction with Jingkun Guo and Teodoro Graziosi during their Master projects.

I would like to acknowledge Michail Vlassov for his great work on filter cavities during his Bachelor project.

I want to thank João Moura for keeping the entropy low in the group and for interesting discussions about multimembrane arrays.

It was amazing to see step by step process of building an STM thanks to weekly updates by Maarten Leeuwenhoek, who also provided me with useful microfabrication tips.

Clemens Schäfermeier stayed in our group for short time, still I am grateful for quantum optics discussions and electronics tips. Soon after Clemens left new postdoc Rob Stockill joined and I am glad that he was also happy to share his quantum optics and general physics knowledge.

I would like to thank to staff of our department in particular Maria Roodenburg, Tino Kool and Ronald Bode for helping me with administration and for technical support.

Success of this thesis was strongly dependant on smooth running of the cleanroom. For this I want to express big gratitude to Kavli Nanolab cleanroom staff.

During my Phd I had a chance to interact with a whole lot more people and I would like to thank everyone who made these four years a pleasant experience.

CURRICULUM VITÆ

Igor MARINKOVIĆ

December,
1990

Born in Kragujevac, Serbia.

EDUCATION

2005–2009 Secondary Education:
First Kragujevac Gymnasium, Kragujevac, Serbia

2009–2012 B.Sc. in Physics
University of Novi Sad, Novi Sad, Serbia

2012-2014 M.Sc. in Physics
University of Bonn, Bonn, Germany
Thesis: Experimental Setup for Rydberg Spectroscopy
Promotor: Prof. dr. D. Meschede

2015-2019 Ph.D. Physics
Delft University of Technology, The Netherlands
Thesis: Optomechanical devices in the quantum regime
Promotors: Dr. S. Gröblacher
Prof. dr. ir. H.S.J. van der Zant

LIST OF PUBLICATIONS

- [1] L. Magrini, R. A. Norte, R. Riedinger, I. Marinković, D. Grass, U. Delić, S. Gröblacher, S. Hong, and M. Aspelmeyer, *Near-field coupling of a levitated nanoparticle to a photonic crystal cavity*, *Optica* **5**, 1597 (2018).
- [2] I. Marinković, A. Wallucks, R. Riedinger, S. Hong, M. Aspelmeyer, and S. Gröblacher, *Optomechanical bell test*, *Phys. Rev. Lett.* **121**, 220404 (2018).
- [3] R. Riedinger, A. Wallucks, I. Marinković, C. Löschnauer, M. Aspelmeyer, S. Hong, and S. Gröblacher, *Remote quantum entanglement between two micromechanical oscillators*, *Nature* **556**, 473 (2018).
- [4] R. A. Norte, M. Forsch, A. Wallucks, I. Marinković, and S. Gröblacher, *Platform for measurements of the casimir force between two superconductors*, *Phys. Rev. Lett.* **121**, 030405 (2018).
- [5] S. Hong, R. Riedinger, I. Marinković, A. Wallucks, S. G. Hofer, R. A. Norte, M. Aspelmeyer, and S. Gröblacher, *Hanbury Brown and Twiss interferometry of single phonons from an optomechanical resonator*, *Science* **358**, 203 (2017).